


1-1-2010

Identification Of Neuroblastoma And Its Prognostic Markers Using Raman Spectroscopy

Rachel Kast
Wayne State University

Follow this and additional works at: http://digitalcommons.wayne.edu/oa_dissertations

 Part of the [Biomedical Engineering and Bioengineering Commons](#), [Biostatistics Commons](#), and the [Oncology Commons](#)

Recommended Citation

Kast, Rachel, "Identification Of Neuroblastoma And Its Prognostic Markers Using Raman Spectroscopy" (2010). *Wayne State University Dissertations*. Paper 94.

This Open Access Dissertation is brought to you for free and open access by DigitalCommons@WayneState. It has been accepted for inclusion in Wayne State University Dissertations by an authorized administrator of DigitalCommons@WayneState.

**IDENTIFICATION OF NEUROBLASTOMA AND ITS PROGNOSTIC MARKERS
USING RAMAN SPECTROSCOPY**

by

RACHEL KAST

DISSERTATION

Submitted to the Graduate School

of Wayne State University,

Detroit, Michigan

in partial fulfillment of the requirements

for the degree of

DOCTOR OF PHILOSOPHY

2010

MAJOR: BIOMEDICAL ENGINEERING

Approved by:

Advisor

Date

Co-Advisor

Date

© COPYRIGHT BY

RACHEL KAST

2010

All Rights Reserved

DEDICATION

To my family and friends.

The past three years have been full of amazing highs and unbearable lows.

Thank you for your support through the good and the bad.

Here's to hoping 2010 will be full of occasions to celebrate!

And to my future children

And their children

And their children

In hopes that this research will have a positive impact in the

Lives of families faced with pediatric cancer

ACKNOWLEDGMENTS

I would first like to thank my advisors Dr. Gregory Auner and Dr. Abhilash Pandya for everything they have provided me. Thank you for your guidance and encouragement, for sharing your expertise and advice, and for allowing me to take this research in its own direction. Thank you also to my committee members for sparing your time to join this committee, and for your comments and insights.

There are dozens of people who were integral in this research. Thank you to the entire CARES group for working with me, and for indulging me when I went on clinical and biological tangents. I would like to thank the ASTII/TEAMS group for the opportunity to work with you, and for the opportunities to present my work to a diverse audience of physicians and engineers.

Thank you Dr. Michael Klein for all of the time you spent discussing topics and providing suggestions. Thank you Dr. Raja Rabah and Dr. Janet Poulik, for keeping an open mind about Raman spectroscopy, and for all you taught me about pathology. I would also like to thank the staff of the pathology department, especially Lisa, Robert, Ruby, and Marcia. Thank you to Dr. Hale Wills for your clinical point of view, and for all of your help. I would like to thank Dave Leslie for all of your help, and for being so reliable.

I would like to thank Dr. Joe Smolinki for all of the advice, and for telling me what I need to hear instead of what I want to hear. Thank you Dr. Michelle Brusatori for all of your help, and for being my workout buddy (Dr. Auner too!). Thank you Kathy Huber for all of help, and for always greeting me with a smile. Thank you Barb House for everything - especially our unwinding sessions. Thank you to Dr. Chantelle Hughes and

Krystle Laja for your help in cell culturing, and thanks to Dr. Madhu Prasad, Dr. Masood Shammash, Dr. Ramesh Batchu, and Dr. Shelly Seward for allowing us into your laboratories and for teaching me cell culturing.

I would like to thank Dr. James Tucker and Dr. Robert Thomas for graciously allowing me to use their laboratory space for PCR testing, and especially thank Tara Twomey for showing me the ropes in biology and cracking a joke when I'm stressing out (degaussing?). I would also like to thank Dr. Jason Shoheit for kindly providing the MYCN-3 cell line for testing of MYCN genetic expression.

Finally, and most importantly, I thank my family and friends for their support through this journey. Thank you for laughing with me, and teasing me, and telling me "you can do it", and for being there through the hard times and the good times. I could not have done this without you.

TABLE OF CONTENTS

Dedication	ii
Acknowledgments	iii
List of Tables.....	vi
List of Figures.....	x
CHAPTER 1: BACKGROUND AND SIGNIFICANCE.....	1
CHAPTER 2: IDENTIFICATION OF NEUROBLASTOMA FROM NEURAL TUMORS ..	29
CHAPTER 3: INCLUSION OF FROZEN TUMORS IN TISSUE STUDIES.....	43
CHAPTER 4: IDENTIFICATION OF NEUROBLASTOMA FROM SMALL ROUND BLUE CELL TUMORS	54
CHAPTER 5: CLASSIFICATION OF UNFAVORABLE, FAVORABLE, AND TREATED NEUROBLASTOMAS	69
CHAPTER 6: BLINDED STUDY WITH CHILDREN'S ONCOLOGY GROUP TO IDENTIFY FAVORABLE, UNFAVORABLE, AND TREATED NEUROBLASTOMA	89
CHAPTER 7: IDENTIFICATION OF MYCN AMPLIFICATION IN NEUROBLASTOMA CELLS	110
CHAPTER 8: CONCLUSIONS	123
CHAPTER 9: FUTURE WORK	126
APPENDIX A: INTERNAL REVIEW BOARD DOCUMENTATION.....	130
APPENDIX B: RAMAN SPECTROSCOPY DATA PROCESSING.....	163
APPENDIX C: CELL CULTURING SOP	163
APPENDIX D: PCR PROCEDURES AND RESULTS.....	163
APPENDIX E: MARKET ANALYSIS FOR RAMAN BIOPSY TOOL.....	163
References	190
Abstract.....	208
Autobiographical Statement	210

LIST OF TABLES

Table 1.1: Truth table for calculation of sensitivity and specificity	5
Table 2.1: Number of spectra and samples for adrenal gland, neuroblastoma, ganglioneuroma, nerve sheath tumor, and pheochromocytoma	36
Table 2.2: Classification sensitivity and specificity results at the spectral and tissue level for each 2-group analysis	38
Table 2.3: Three-group classification results for discrimination between normal adrenal gland, neuroblastoma, and ganglioneuroma	39
Table 3.1: Number of fresh and frozen specimen and spectra measured for each type of tissue.....	47
Table 3.2: Tissue-Level Classification Results	49
Table 3.3: Individual Spectra Classification Results.....	50
Table 4.1: Most commonly diagnosed ages for each small round blue cell tumors.....	54
Table 4.2: Samples and spectra used for identification of neuroblastoma from other small round blue cell tumors	62
Table 5.1: Definition of the Shimada system of classifying favorable and unfavorable neuroblastoma, ganglioneuroblastoma, and ganglioneuroma	71
Table 5.2: Number of unfavorable, favorable, and treated neuroblastomas in preliminary fresh tissue analysis	78
Table 5.3: Classification of favorable and unfavorable neuroblastoma	79
Table 5.4: Classification results comparing untreated and treated neuroblastoma	80
Table 5.5: Classification of ganglioneuroma and treated neuroblastoma.....	80
Table 5.6: Classification of unfavorable, favorable, and treated neuroblastoma	81
Table 5.7: Data collected for fresh versus frozen study.....	84

Table 5.8: Classification of treated and untreated frozen neuroblastoma (“cases not selected” row) based on classification model of fresh neuroblastoma (“cases selected” row).....	85
Table 5.9: Classification of treated and ganglioneuroma frozen spectra (“cases not selected” row) based on classification model of fresh spectra (“cases selected row”)	86
Table 6.1: Classification results of untreated versus treated tissue using select peaks in the range from 600-1800 and excluding potential and obvious outliers	96
Table 6.2: Classification results of untreated versus treated tissue using select peaks in the range from 600-1800 cm^{-1} excluding only obvious outliers.....	96
Table 6.3: Classification results of favorable versus unfavorable tissue using select peaks in the range from 600-1800 and excluding potential and obvious outliers	97
Table 6.4: Classification results of favorable versus unfavorable tissue using select peaks in the range from 600-1800 cm^{-1} excluding only obvious outliers.....	97
Table 6.5: Classification results of untreated versus treated tissue using all peaks from 600-1220 cm^{-1} and excluding potential and obvious outliers	98
Table 6.6: Classification results of untreated versus treated tissue using all peaks from 600-1220 cm^{-1} and excluding only obvious outliers	99
Table 6.7: Classification results of unfavorable versus favorable tissue using all peaks from 600-1220 cm^{-1} and excluding potential and obvious outliers...	100
Table 6.8: Classification results of favorable versus unfavorable tissue using all peaks from 600-1220 cm^{-1} and excluding only obvious outliers.....	100
Table 6.9: Classification results of untreated versus treated tissue using 13 select peaks between 600-1220 cm^{-1} and excluding potential and obvious outliers	101
Table 6.10: Classification results of untreated versus treated tissue using 13 select peaks between 600-1220 cm^{-1} and excluding only obvious outliers	101

Table 6.11: Classification results of untreated versus treated tissue using 8 select peaks between 600-1220 cm^{-1} and excluding potential and obvious outliers	102
Table 6.12: Classification results of untreated versus treated tissue using 8 select peaks between 600-1220 cm^{-1} and excluding only obvious outliers	102
Table 6.13: Classification results of unfavorable and favorable tissue using select peaks between 600-1220 cm^{-1} and excluding potential and obvious outliers	103
Table 6.14: Classification results of untreated versus treated tissue using 8 select peaks between 600-1220 cm^{-1} and excluding only obvious outliers	103
Table 6.15: Comparison of tissue-level results using each classification method for treated versus untreated neuroblastoma. 453-spectra results represent analysis with obvious outliers removed, and 419-spectra results represent analysis with obvious and potential outliers removed	105
Table 6.16: Comparison of tissue-level results using each classification method for favorable versus unfavorable neuroblastoma. 453-spectra results represent analysis with obvious outliers removed, and 419-spectra results represent analysis with obvious and potential outliers removed.....	106
Table 7.1: Classification results using all peaks from 924-1800 cm^{-1} . Group 1 is the control group at t=24h, Group 2 is the control.....	119
Table D.1: Relative concentration of RNA and 260/280 ratio for each sample.....	173
Table D.2: Calculations for each sample to determine the concentration of RNA and water needed to initiate cDNA generation.....	173
Table D.3: Relative quantification PCR results, calibrated to 100ng sample K and the GAPDH housekeeping gene.....	179
Table E.1: Annual incidence of the most common types of cancer	184
Table E.2: Projected Year 1 revenue	185
Table E.3: Predicted five year revenue of surgical instrument	186
Table E.4: Potential first-year revenue from pathology laboratory-based systems for breast cancer.....	188

Table E.5: Five-year revenues for laboratory-based diagnostics and surgical diagnostics.....	189
--	-----

LIST OF FIGURES

Figure 1.1: Conversion from tyrosine to norepinephrine and epinephrine.....	7
Figure 1.2: Infrared-active and inactive molecules	9
Figure 1.3: Changes in polarizability caused by shifting dipole moments.....	10
Figure 1.4: Anti-Stokes, Stokes, and Rayleigh scattering.....	11
Figure 1.5: Raman spectrometer schematic.....	14
Figure 1.6: Examples of Raman spectra before and after preprocessing.....	15
Figure 1.7: Data analysis flowchart	18
Figure 1.8: Following tumor resection, a pathologist performs a quick analysis, then a more detailed analysis. If tumor cells are found, more tissue must be removed	23
Figure 1.9: Proposed Raman system for margin assessment should provide quicker results with higher accuracy	24
Figure 2.1: Mean spectra of each tissue type with correlating histological images. Labeled circled peaks are areas of difference between tissue types.....	37
Figure 2.2: Discriminant function results show separation between normal adrenal tissue and neuroblastoma and ganglioneuroma. Results also show an overlap between neuroblastoma and ganglioneuroma.....	40
Figure 3.1: Mean fresh (solid black line) and frozen (dotted line) spectra of normal adrenal gland, neuroblastoma, ganglioneuroma, nerve sheath tumor, and pheochromocytoma	48
Figure 4.1: Decision Tree for discriminant function analysis peak selection.....	61
Figure 4.2: mean spectrum and histology images of neuroblastoma, Ewing sarcoma, rhabdomyosarcoma, and non-Hodgkin lymphoma with key diagnostic peaks marked.....	64
Figure 5.1: Mean spectra of favorable and unfavorable neuroblastoma	79

Figure 5.2: The mean spectra of untreated neuroblastoma, treated neuroblastoma, and ganglioneuroma with discriminant function analysis results shown	82
Figure 5.3: Discriminant function analysis and histology images of three tumors from one patient.....	83
Figure 5.4: fresh (solid black line) and frozen (dashed red line) mean spectra of unfavorable, favorable, and treated neuroblastoma	85
Figure 6.1: mean spectra of favorable, unfavorable, and treated training data, and mean spectrum of unknown data measured with Nikon lens.....	92
Figure 6.2: Mean spectrum of all training data measured with Leica lens (black) and four distinct populations measured by the Nikon lens.....	93
Figure 6.3: Mean spectrum of unfavorable, favorable, and treated training data with unknown data measured using the replacement Leica lens	94
Figure 6.4: Mean Raman spectra of favorable, unfavorable, and treated spectra measured with original Leica lens and unknown spectra measured with replacement Leica lens before (top) and after (below) data truncation.....	99
Figure 6.5: Key peaks in the range of $600-1220\text{ cm}^{-1}$ for classification of unfavorable, favorable, and treated neuroblastoma	104
Figure 7.1: Representative Raman spectra of a MYCN-3 cell (top) and UV quartz slide (below)	116
Figure 7.2: Schematic showing cell measurement setup	117
Figure 7.3: a) shows an ideal cell for measurement. The cell is clearly separated from surrounding cells and displays a white 'halo'. b) and c) show examples of cells which would not be measured because they are out of focus and too close to each other.....	117
Figure 7.4: Mean spectrum of each group in the 3-flask experiment.....	119
Figure 9.1: Experimental design. Control cells were tested at time = 0 hours. Control and MYCN-amplified cells were tested at time = 6 hours, 24 hours, and 48 hours.....	129
Figure D.1: Layout of 96-well plate for PCR	178

Figure D.2: PCR amplification curves for sample B (top), K (middle), and L (bottom). 180

Figure D.3: Relative quantitative PCR results with sample K as the control..... 182

CHAPTER 1 BACKGROUND AND SIGNIFICANCE

1.1 Neuroblastoma

The second most common cause of death in children from ages 1-14 in the United States is cancer (Jemal, A. et al., 2008). 8-10% of all pediatric cancers are neuroblastoma, however it accounts for about 15% of all cancer deaths in children (Cotran, R. S. et al., 1994; Howman-Giles, R. et al., 2007). There are 400-650 new diagnoses in the United States each year ("What Are the Key Statistics About Neuroblastoma?," 2009; Young Jr, J. L. et al., 1986). Neuroblastoma is most common in infants and toddlers. In approximately half of all cases, children begin to show symptoms before age 2, and 90% of cases present by 5 years old (Howman-Giles, R. et al., 2007).

Neuroblastoma develops in neural cells of the sympathetic nervous system ("What is Neuroblastoma," 2009) which are derived from the neural crest, an embryologic structure (Jessen, K. R. Mirsky, R., 2005). The malignant immature developing neural cells are called neuroblasts (neural = nerve, blast = immature).

The sympathetic nervous system is part of the autonomic nervous system, meaning that it is controlled automatically, or without conscious input. The sympathetic nervous system runs throughout the body, and consists of nerve cells (neurons) and glial cells. Glial cells support neural cells by performing several important functions, including myelinating nerve axons, releasing neurotransmitters, and forming connective tissue to hold neurons in place. Detailed reviews of the origin, formation, and function of glial cells of the peripheral nervous system are available from many sources (Jessen, K. R. Mirsky, R., 2005).

Just over 1/3 of neuroblastomas are found in the medulla of the adrenal gland, which contains sympathetic nervous system glial cells derived from the neural crest ("What is Neuroblastoma," 2009). Another 1/3 of neuroblastomas are found in the sympathetic ganglia and sympathetic chain elsewhere in the abdomen, and the rest can be found in the sympathetic ganglia of the chest, neck, and pelvis (Orkin, S. H. et al., 2009).

1.1.1 Neuroblastoma Diagnosis

Symptoms of neuroblastoma vary based on where the tumor is located. When the tumor is found in the abdomen, symptoms include an abdominal mass which may be accompanied by pain or fullness. Other symptoms such as swelling or hypertension can be caused by compression of local vessels. When neuroblastoma metastasizes, frequent symptoms are bone and joint pain, fever, failure to thrive, bruising, low white blood cell levels, and proptosis (eye dislocation) or periorbital ecchymoses (raccoon eyes) which can both be caused by metastasis to the periorbital bones. Another symptom of neuroblastoma is increased levels of catecholamine byproducts in the urine caused by increased release of neurotransmitters by glial cells. Opsoclonus-myoclonus syndrome and vasoactive intestinal peptide syndrome are two paraneoplastic syndromes which are associated with neuroblastoma (Orkin, S. H. et al., 2009).

While a suspected diagnosis of neuroblastoma can be made based on a patient's symptoms, the only way to make a definite diagnosis is to perform a biopsy and examine the tumor cells using histology or other pathology methods. To look at the histology, the pathologist cuts a thin slice of tissue (~10 microns) and mounts it on a clear glass slide. The tissue is then stained with hematoxylin and eosin (H&E).

Hematoxylin binds to nucleic acids within the cell nucleus and stains them blue. Likewise, eosin stains the cytoplasm pink. Once the stained tissue sample dries, the pathologist can view it under a microscope to examine the cellular behavior within the tumor. Remaining portions of the tumor are saved and may be used for other pathology tests, if a conclusive diagnosis cannot be made with histology alone, or if more detailed diagnostic information is required.

The histology and aggressiveness of neuroblastoma varies from tumor to tumor. Representative histology images of neuroblastoma are shown in Figures 2.1 and 4.2. Some neuroblastomas are fully encapsulated, while others invade the surrounding tissue. The most common histological appearance contains sheets of small, embryonic-appearing cells that have dark blue nuclei, little cytoplasm, and indistinct cell walls (Cotran, R. S. et al., 1994). This histologic appearance is similar to a class of childhood tumors called small round blue cell tumors. This group of tumors includes neuroblastoma, Ewing sarcoma, rhabdomyosarcoma, and non-Hodgkin lymphoma. Tumors with this histology often require further testing including immunohistochemistry (Finegold, M. J. et al., 1983; Gregorio, A. et al., 2008), cytogenetics including fluorescence in situ hybridization (Taylor, C. et al., 1993), and polymerase chain reactions (PCR) (Chen, Q.-R. et al., 2007), or complementary DNA microarrays (Khan, J. et al., 2001) to confirm the diagnosis.

The second typical histology of neuroblastoma shows some differentiation. While the tumor is still predominantly composed of immature neuroblast cells, there are also some larger, differentiated cells. Cell differentiation can be identified by the larger

cell size, larger nuclei and nucleolus, and higher amounts of cytoplasm (Cotran, R. S. et al., 1994).

Ganglioneuroma is composed of similar cells to neuroblastoma, however its histologic appearance contains all differentiated cells which look like mature neurons or ganglion cells (Cotran, R. S. et al., 1994) instead of immature neuroblasts. In this case, the tumor is benign. In some cases, malignant neuroblastoma cells can mature to ganglioneuroma cells.

Ganglioneuroblastoma is a condition between ganglioneuroma and neuroblastoma ("What is Neuroblastoma," 2009). It contains a mixture of benign mature ganglion cells and malignant immature neuroblasts. Because it still contains malignant cells, ganglioneuroblastoma is treated like neuroblastoma. For the purposes of this document, ganglioneuroblastomas will simply be referred to as neuroblastomas.

Following a positive diagnosis of neuroblastoma, the pathologist assigns several sub-classifications. The tumor is given a stage from I-IV based on the spread of the tumor through the lymphatic system and the rest of the body. A favorable or unfavorable assignment is also assigned based on the histology and the patient's age, according to a methodology called the Shimada classification. Tumor favorability is used to determine the patient's prognosis, as well as to predict the optimal treatment plan for each patient. The histologic factors included in identifying the favorability include the degree of maturation of the tumor cells, the presence or absence of stromal cells (connective tissue), and the ratio of cells undergoing mitosis or karyorrhexis. Section 5.1 explains tumor favorability based on the Shimada classification and other prognostic markers of neuroblastoma in depth.

Additionally, the pathologist may test the genetic profile of the tumor to see if it displays genetic features which are associated with a positive or poor prognosis. These sub-classifications are further described in Chapters 5 and 7.

1.1.2 Screening for Neuroblastoma

Neuroblastoma has no major risk factors. Some studies show only 1-2% of cases are hereditary ("What are the Risk Factors for Neuroblastoma?," 2009), but other sources say as many as 20% of cases may be due to hereditary factors (Cotran, R. S. et al., 1994). Neuroblastomas may be caused by neuroblast cells which do not fully mature during fetal development due to some type of genetic mutation ("Do We Know What Causes Neuroblastoma?," 2009). The MYCN oncogene is over expressed in many neuroblastomas, and the TrkA tumor suppressor gene is under expressed in many neuroblastomas. There are no known causes for the genetic changes which occur in neuroblastoma.

Non-invasive or minimally invasive screening methods have had high success rates in detecting other types of cancer. These screening techniques tend to have lower sensitivity and high specificity. Truth tables are often used to calculate sensitivity and specificity, as shown in Table 1.1. Sensitivity is defined as the number of true positives divided by the sum of true positives and false negatives, while specificity is defined as the number of true negatives divided by the sum of true negatives and false positives.

		Actual Diagnosis	
		Positive	Negative
Predicted Diagnosis	Positive	True Positive	False Positive
	Negative	False Negative	True Negative

Table 1.1: Truth table for calculation of sensitivity and specificity

High specificity is important so that there are no false negatives (the test misses a true cancer case). Sensitivity relates to the number of true positives detected, so lower sensitivity means that not all cancer cases are detected with the given test. An added benefit of screening tests is that they can reduce the mortality rate of the cancer for which they are screening (Mandel, J. S. et al., 1993), although this is not always the case (Olsen, O. Gøtzsche, P. C., 2001). Examples of widely accepted screening tests are:

- The papanicolaou cervical smear test (PAP smear) is used to detect cervical cancer with 30-87% sensitivity and 86-100% specificity (Nanda, K. et al., 2000).
- Mammography is used to detect breast cancer with approximately 75% sensitivity and approximately 88% specificity (Houssami, N. et al., 2003).
- Fecal occult blood testing to detect colon cancer or other disease of the anus had 12-82% sensitivity and 95% specificity in one study (Nakama, H. et al., 1997), but results have been significantly lower in other studies (Winawer, S. J., 2007). Annual screening instead of sporadic screening can increase detection rates.

More than 35 years ago, researchers in Japan noticed that there was an increase in the catecholamines homovanillic acid (HVA) and vanillylmandelic acid (VMA) in the urine of patients with neuroblastoma. Figure 1.1 briefly describes the conversion of tyrosine to epinephrine and norepinephrine (Vuguin, P. M., 2009). Epinephrine and norepinephrine are then converted to VMA and HVA. Typically, the release of norepinephrine and epinephrine is governed by the sympathetic nervous system. In the case of neuroblastoma, ganglia within the tumor can synthesize catecholamines, and

release can be triggered by physical or chemical triggers outside of the sympathetic nervous system.

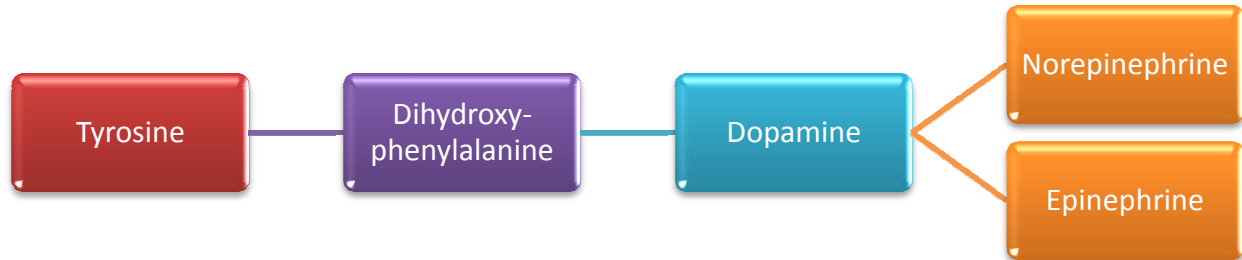


Figure 1.1: Conversion from tyrosine to norepinephrine and epinephrine

Since neuroblastoma is most common in young children, screening tests were developed to test the level of VMA and HVA in urine samples of newborns (Sawada, T. et al., 1991; Treuner, J. Schilling, F. H., 1995). These tests were implemented internationally, but never in the United States.

These urine screening tests were shown to accurately identify neuroblastoma at much higher rates than it was previously identified. Long-term studies showed that screening tests were not actually beneficial, however, because the majority of neuroblastomas identified were a special type of neuroblastoma described as ‘Stage 4S’ (described below) which would not require treatment ("Can Neuroblastoma be Found Early?," 2009).

1.1.3 Neuroblastoma Treatment and Outcomes

Neuroblastoma has two unusual outcomes which make it stand out from other types of cancer. Under specific circumstances, neuroblastomas can undergo spontaneous regression, and patients can go into complete remission with little or no

medical intervention ("What is Neuroblastoma," 2009). This is called stage 4S neuroblastoma.

In other cases, the immature cancer cells can develop into mature ganglion or nerve sheath cells, and the neuroblastoma as a whole develops into a ganglioneuroma. This is also significant because ganglioneuroma is a benign condition and poses significantly fewer risks to the patient, whereas neuroblastoma is a malignant condition. Typically, however, neuroblastoma must be treated.

1.2 Raman Spectroscopy

1.2.1 Raman Scattering

The following series of equations can be used to describe the relationship between energy, wavelength, frequency, and wavenumber in radiating light.

$$E = h \nu$$

$$\lambda = c / \nu$$

$$\sigma = \nu / c = 1 / \lambda$$

The energy (E) is equal to Planck's constant ($h = 6.626 \times 10^{-34} \text{ m}^2 \text{ kg} / \text{s}$) multiplied by the frequency (ν) of the light. The wavelength of the light is equal to the speed of light ($c = 3 \times 10^8 \text{ m/s}$) divided by the frequency. Finally, the wavenumber (σ) is equal to the frequency divided by the speed of light, or the inverse of the wavelength.

Typically, when light is incident on a molecule, it interacts only with the electron cloud surrounding the molecule, and there is only a tiny energy interaction between the electrons and the incident light. This interaction is very unstable. The molecule quickly returns back to its original state, and the light is scattered at its original wavelength and frequency. This is elastic scattering known as Rayleigh scattering (Smith, E. Dent, G.,

2005). In rare cases, however, the photon (unit of light energy) interacts with the nucleus, causing a shift in the vibration of the nucleus.

Infrared spectroscopy is a vibrational spectroscopy technique complimentary to Raman spectroscopy. It measures the change in the dipole moment of a molecule. Molecules which have no net dipole moment, however, cannot be measured using infrared spectroscopy. Figure 1.2 illustrates this concept. The left hand molecule is infrared-active because the net dipole moment can be changed while the right hand molecule is infrared-inactive because there is no net dipole moment. Therefore, there can be no shift in the dipole moment.

Complimentary to infrared spectroscopy, Raman spectroscopy measures the resulting change in polarizability caused by interaction of the incident light with the nucleus. Polarizability is the tendency of the electron cloud to distort caused by the shift in the dipole moments. While Infrared spectroscopy cannot detect the presence of the right-hand molecule in Figure 1.2, note that the same molecule could be measured using Raman spectroscopy, as shown in Figure 1.3.

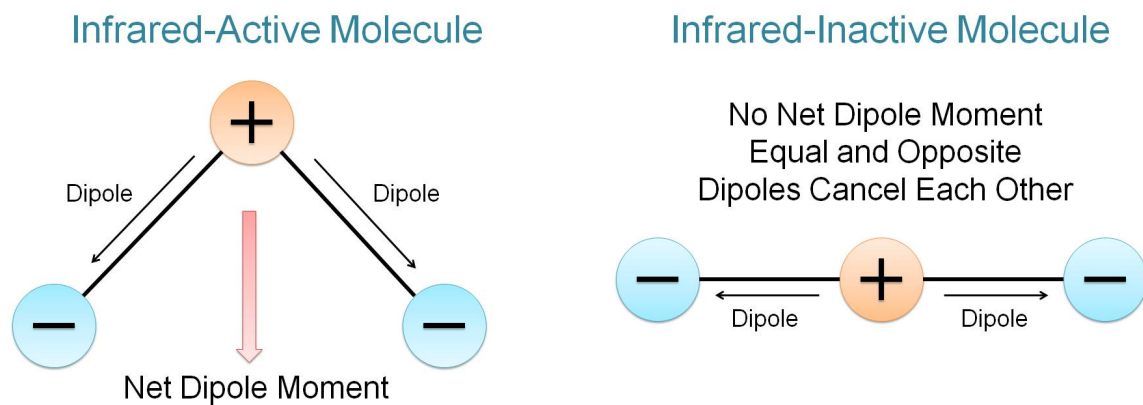


Figure 1.2: Infrared-active and inactive molecules

There are two types of vibrational scattering. In Stokes scattering, some of the energy of the incident photon is absorbed by the molecule. Due to conservation of energy, the loss in energy of the scattered photon from the incident photon is equal and opposite to the energy change of the shift in the dipole moment.

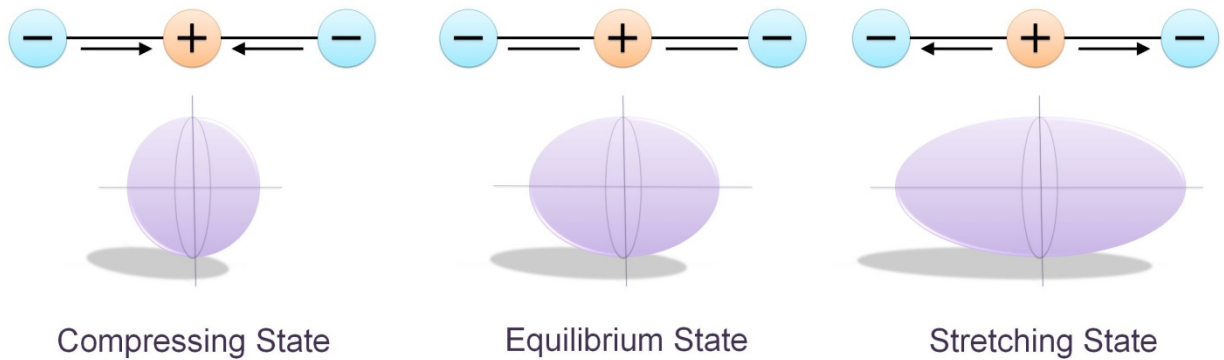


Figure 1.3: Changes in polarizability caused by shifting dipole moments.

Anti-Stokes scattering occurs when the molecule is already in an excited vibrational state. In this case, the scattered photon absorbs some of the energy from the molecule as it returns to its ground state. The scattered photon, then, has a higher energy and shorter wavelength than the incident photon. Note that Stokes and anti-Stokes scattering result in a wavelength shift due to the change in energy of the test molecule, whereas Rayleigh scattering has no shift in wavelength because there is no vibrational change within the molecule. Figure 1.4 shows the energy diagram for Rayleigh, Stokes, and anti-Stokes scattering.

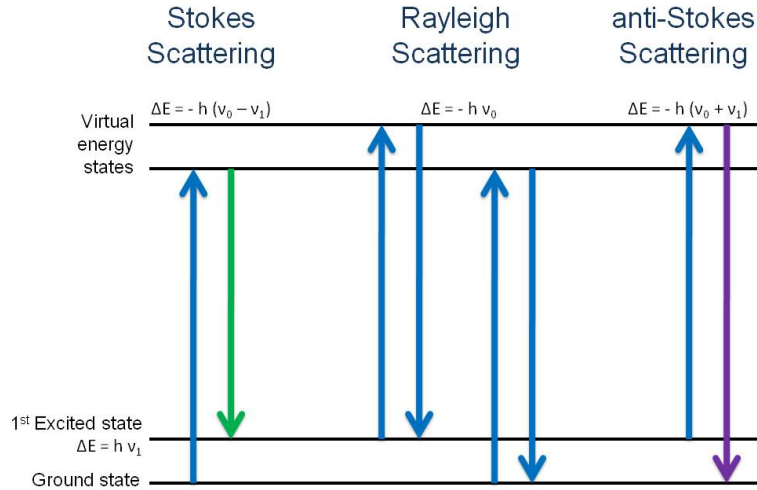


Figure 1.4: Anti-Stokes, Stokes, and Rayleigh scattering.

Typically, most of the molecules within a test sample will be at the ground state, rather than an excited state. Therefore, Stokes scattering is far more common than anti-Stokes scattering. For that reason, most Raman instrumentation is only setup to measure Stokes scattering. Even measurement of Stokes scattering posed a large challenge for decades, however, because only about 1 in 10^7 incident photons trigger the Raman effect. Current systems use single-wavelength lasers as excitation sources, sensitive charge coupled devices to count the scattered photons, and advanced computer processing to analyze data. The combination of these advances make Raman spectroscopy a reasonable tool for biological applications.

For a given particle, it is possible to theoretically predict the change in polarizability (α).

$$\alpha = p / \bar{E}$$

Polarizability is defined as the ratio between the dipole (p – calculated in general as the integral of the charges multiplied by the distance) of the molecule and the electric field of the incident light (\bar{E}). The electric field of the incident light is defined as

$$\bar{E} = \bar{E}_0 \cos(2 \pi \nu t)$$

where ν is the frequency of the light, t is time, and E_0 is the initial electric field.

The polarizability is defined as

$$\alpha = \alpha_0 + \alpha_{vib} \cos(2 \pi \nu_{vib} t)$$

where ν_{vib} is the vibrational frequency of the incident molecule. These two terms can be multiplied to calculate the dipole (Colthup, N. B. et al., 1990):

$$p = \frac{\alpha_{vib} E_0}{2} \{ \cos[2 \pi t (\nu + \nu_{vib})] + \cos[2 \pi t (\nu - \nu_{vib})] \}$$

1.2.2 The Raman Spectrum

Quantum mechanics states that a molecule can only vibrate a specific number of ways. Linear molecules containing N atoms have $3N-5$ modes, and nonlinear molecules have $3N-6$ vibration modes. Based on the change in energy of the vibrational frequency, the wavelength of the scattered photon can be calculated. For a given molecule, the exact Raman shift in wavenumbers can be calculated using the formula

$$\omega = \frac{1}{\lambda_{incident}} - \frac{1}{\lambda_{scattered}}$$

A Raman spectrum is the plot of the wavenumbers on the x-axis versus the count on the y-axis. The y-axis represents how many Raman shifts were measured. Because each molecule has a unique set of possible vibrations, a single molecule can be identified based on the wavelength shifts of the incident light (wavenumber). When a sample is composed of different types of molecules, there will be peaks at several

wavenumbers. The relative height of the peaks represents the relative ratios of each molecule within the sample.

Using known biochemicals to establish known peaks, Raman spectroscopy can provide information about the underlying biochemistry of a sample. Each chemical has a characteristic Raman peak or combination of Raman peaks. Some chemicals have overlapping peak regions. Analysis of Raman peaks becomes more and more complicated as more and more chemicals are added to a sample (Socrates, G., 2001). Raman peaks for a given chemical may shift slightly based on the characteristics of the other chemicals it is surrounded by (Socrates, G., 2001).

1.2.3 Raman Spectrometer

Because the Raman effect is so small (approximately 1 in 10^7), specialized instrumentation is required to obtain efficient Raman measurements. Figure 1.5 shows a simplified schematic of a Raman spectrometer. A laser source is used to provide high power light at a specific wavelength with a highly focused beam. The beam is focused on the sample through the microscope lens. The lens then collects the scattered light. It passes through a notch filter which removes all the Rayleigh scattered light of the same wavelength. It is then focused on a grating which separates all the wavelengths of light, and then focused on a charge coupled device detector (CCD). The CCD counts the number of photons at each wavelength and sends the information to the computer.

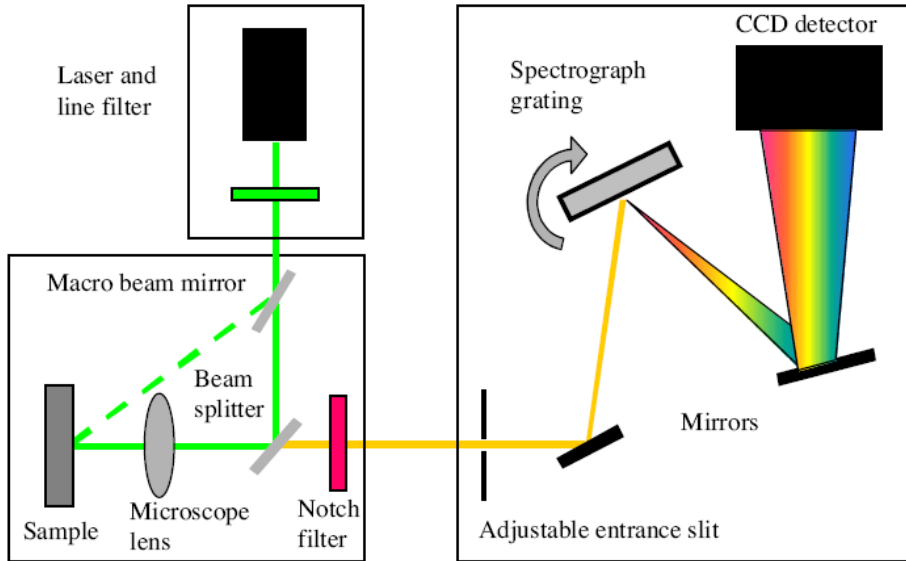


Figure 1.5: Raman spectrometer schematic

All experiments described here were performed using a Renishaw In-Via Raman spectrometer using a 500 mw 785 nm GaAs laser excitation source and 1200/mm grating. The system resolution is 3 cm^{-1} .

1.2.4 Analysis Methods Used in Raman Diagnostics

1.2.4.1 Preprocessing

Following Raman measurement, a two-column text file is created by the measurement software. The first column contains the wavenumbers measured, and the second column contains the number of photons counted at each wavenumber. Before any processing can be done, however, files must be pre-processed to standardize the spectra.

In-house automated pre-processing software is used to remove cosmic rays, noise and tissue fluorescence, and then normalize data on a scale from 0 to 1 (Cao, A. et al., 2007). Wavelet filtering is used to remove noise and smooth the data.

For fluorescence removal, the software matches a polynomial background to local minima along the spectra. The software was programmed to identify which order of polynomial best fit each spectrum based on its fluorescence pattern. Figure 1.6 shows two example spectra plotted before and after preprocessing. Note that the underlying fluorescence pattern is different between the two spectra, and the background subtraction was adjusted accordingly for each.

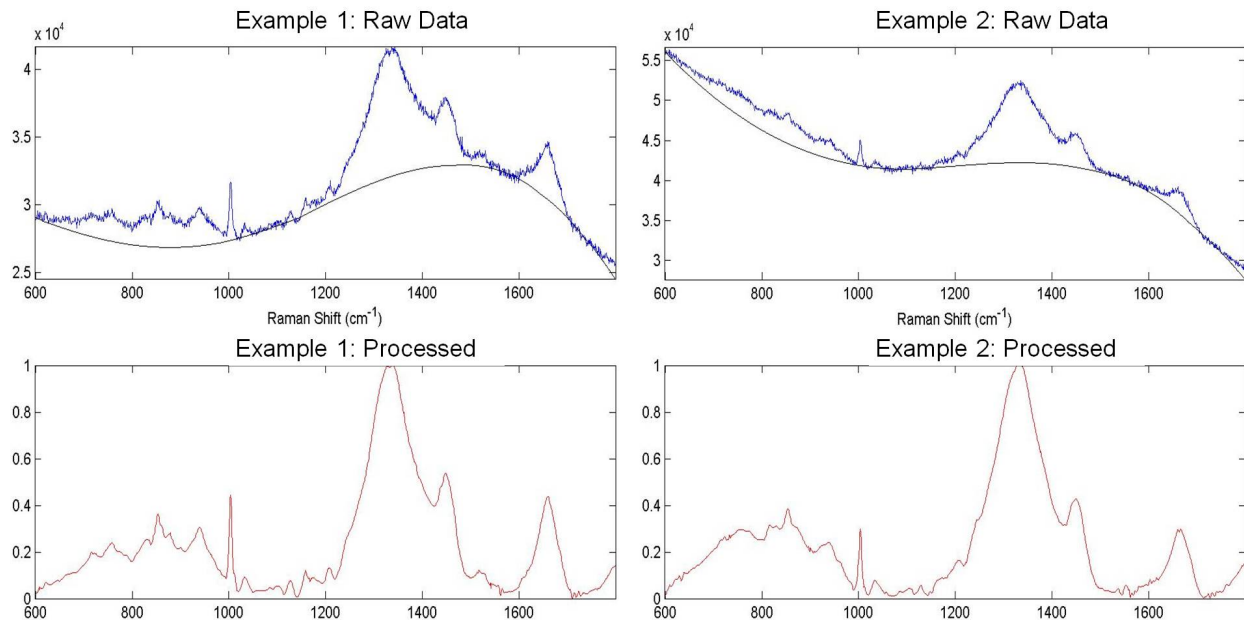


Figure 1.6: Examples of Raman spectra before and after preprocessing.

Data is stored on a secure online server until processing. An in-house database stores information about the files, including the date collected and measurement parameters, as well as the diagnosis and notes made by the pathologists. This database was described extensively in previous work (Weber, R. E., 2007).

1.2.4.2 Data Analysis

Several options exist for analyzing and classifying Raman spectra, including neural networks (de Paula, A. Sathaiah, S., 2005; Gniadecka, M. et al., 2004; Weber, R. E., 2007), principal component analysis (Frausto-Reyes, C. et al., 2005; Guicheteau, J. et al., 2008; Kawabata, T. et al., 2008; Sato-Berru, R. et al., 2007; Ye, Z. Auner, G., 2004a), and discriminant function analysis (Brown, K. L. et al.; Jarvis, R. Goodacre, R., 2004; Kawabata, T. et al., 2008), amongst other methods (Krafft, C. et al., 2009; Ye, Z. Auner, G., 2003, 2004b). Previous work showed good agreement between neural network analysis and discriminant function analysis when both were performed on the same dataset (Weber, R. E., 2007).

Principal component analysis (PCA) is a technique which can be used to compress the data set from many variables to a manageable set of 20 or less. PCA rotates the data in such a way that the new first variable (component) represents the maximum variability within the dataset. The second component explains the next-most variability, and it is orthogonal to the first component. The components continue in this pattern until all the variability is explained. The final number of principal components is equal to the original number of variables; however, the only significant components will be at the beginning of the dataset. A cutoff can be assigned so those only the variables which explain X% new variance (example: .05% of variance) are saved. This allows the data to be condensed from thousands of variables to a much smaller set which often contains 75% of the variance or more. In depth description of PCA is available in several texts (Jolliffe, I. T., 1986) (Geladi, P. Kowalski, B. R., 1986; Stevens, J. P.,

2002; Tabachnick, B. G. Fidell, L. S., 2007), and description of PCA used for analysis of Raman spectra is also available (Dai, H., 2005).

While PCA is a helpful tool for data compression, it is not an ideal diagnostic tool. Discriminant function analysis (DFA) is the classification technique used for all experiments described here. While Raman spectroscopic data often does not meet the statistical requirements assumed for DFA (Klecka, W. R., 1980), it has been applied to several types of Raman data (Brown, K. L. et al.; Kast, R. E. et al., 2008; Pandya, A. K. et al., 2008; Wills, H. et al., 2009b). PCA components can be used as input to discriminant function analysis, or a combination of peak data can be used as input. A benefit of DFA is that the analysis results allow the user to determine which variables in the analysis are significant from which variables are noisy or insignificant. Like PCA, DFA rotates the dataset, aligning the most variation along the first variable (canonical function), the second most variability along the second variable, etc. Data points are plotted along the rotated variables.

When performing analysis, a 'gold standard' diagnosis is assigned to each spectrum. The gold standard diagnosis is assigned by the pathology staff as the 'known' diagnosis based on the tissue histology and other methods when necessary. To ensure accuracy of the gold standard diagnosis, two or more pathologists review each case. The DFA model is created based on the known gold standard diagnosis. For each diagnosis group, a centroid point is calculated based on the average location of all points within that group. Diagnosis of new spectra, then, is based on the closest centroid. Again, there are many books available which describe DFA in depth (Klecka, W. R., 1980; Stevens, J. P., 2002; Tabachnick, B. G. Fidell, L. S., 2007). While DFA is

the classification methodology used in this work, neural networks, logistic regression, or other methods may be used with Raman spectroscopic data.

Classification results provide a predicted diagnosis for each individual spectrum. Sensitivity and specificity are calculated at the spectral level based on these results, using pathology diagnosis as the gold standard. Once spectra-level results are calculated, the same results are calculated for each tissue. Each tissue's diagnosis is made based on the majority classification of the individual spectra. Figure 1.7 outlines the data processing methodology.

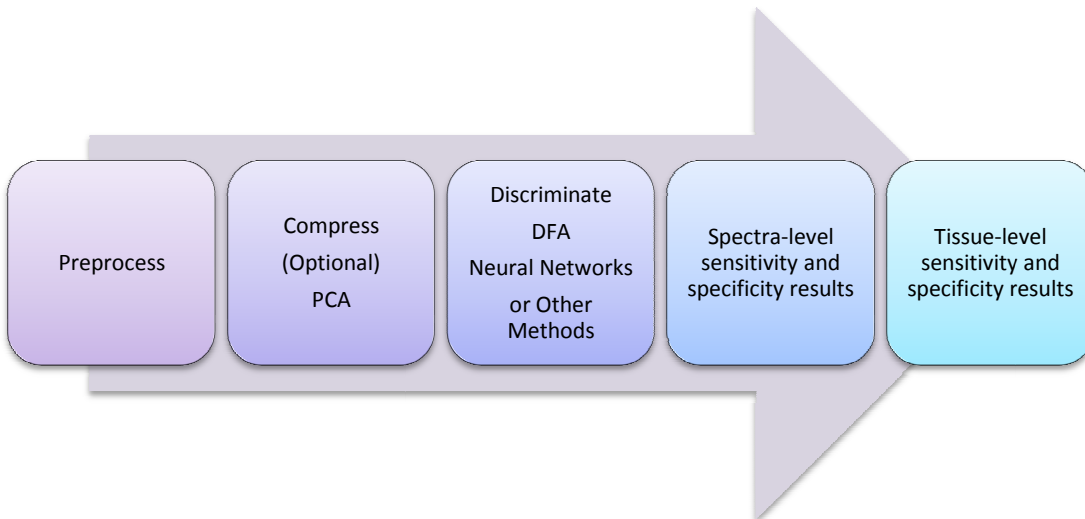


Figure 1.7: Data analysis flowchart

1.2.5 History of Raman Spectroscopy as a Biological Detection Tool

Raman spectroscopy was used in biological applications as early as 1936 to identify amino acids and fatty acids, among other compounds (Edsall, J. T., 1936). It was not commonly used as a laboratory practice, however, until commercial lasers, spectrometers, and computers became available in the 1960's (Gremlich, H.-U. Yan, B., 2001). In 1977, Cancer Research published an article which examined the plasma

membranes from normal and cancerous hamster lymphocytes using Raman spectroscopy (Verma, S. P. et al., 1977). This marked the beginning of the modern era of Raman spectroscopy for tissue diagnostics.

In the past 20 years, Raman spectroscopy has been applied to several whole-tissue cancer diagnostic applications, including breast (Frank, C. J., 1994; Haka, A. S. et al., 2002; Haka AS, V., Gardecki, Nazemi, Lyons, Hicks, Fitzmaurice, Dasari, Crowe, Feld, 2006; Haka, S.-P., Fitzmaurice, Crowe, Dasari, Feld, 2005; Manoharan, R. et al., 1998; Redd, D. C. B. et al., 1993), brain (Krafft, C. et al., 2003; Wolthuis, R. et al., 2001), cervical (Mahadevan-Jansen, A. et al., 1998a; Mahadevan-Jansen, A. et al., 1998b; Utzinger, U. et al., 2001), thyroid (Teixeira, C. et al., 2009), pancreatic (Pandya, A. K. et al., 2008), bladder (Stone, N. et al., 2002), lung (Draux, F. et al., 2008; Huang, Z. et al., 2003b; Kaminaka, S. et al., 2001), kidney (Lieber, C. Kabeer, M.; Wills, H. et al., 2009b), prostate (Crow, P. et al., 2003a), esophageal (Kendall, C. et al., 2003; Li, X. et al., 2004; Shetty, G. et al., 2006a), and skin cancer (Fendel, S. Schrader, B., 1998; Gniadecka, M. et al., 1997; Hata, T. R. et al., 2000; Johansson, C. K. et al., 1999), amongst others.

Once Raman spectroscopy was proven as a diagnostic technique, researchers began developing portable tools for Raman spectroscopic measurement *in-vivo* (Mahadevan-Jansen, A. et al., 1998b; Motz, J. T. et al., 2005; Motz, J. T. et al., 2004; Shim, M. G. et al., 1999; Utzinger, U. Richards-Kortum, R., 2003). Rather than trying to miniaturize an entire spectrometer, however, these designs focus on development of fiber optic delivery and collection fibers for Raman measurement. They still require attachment to a larger spectrometer which must be within the length of the fiber probe.

Several studies used portable fiber optic devices to measure Raman spectra from easily-accessible tissues, including skin (Caspers, P. J. et al., 2003; Fendel, S. Schrader, B., 1998) and cervical tissue (Robichaux-Viehoever, A. et al., 2007). In 2006, the first in-vivo Raman measurement of breast cancer resection surgery was published (Haka, A. S. et al., 2006a).

Raman spectroscopy has also been used to measure individual cancer cells in many applications, including breast and cervical cancer (Yazdi, Y. et al., 1999), lung cancer (Draux, F. et al., 2008; Verrier, S. et al., 2004), prostate cancer (Crow, P. et al., 2005a; Harvey, T. J. et al., 2008; Taleb, A. et al., 2006), leukemia and lymphoma (Chan, J. W. et al., 2008; Chan, J. W. et al., 2006), cervical cancer (Matthaus, C. et al., 2007), liver cancer (Hawi, S. et al., 1996), and bladder cancer (Harvey, T. J. et al., 2008). It has also been used outside of cancer research. In cellular studies, it has been used to measure cell death (Huang, Y. et al., 2005; Notingher, I. et al., 2002; Verrier, S. et al., 2004), cell proliferation (Short, K. W. et al., 2005), identify individual bacteria cells (Schuster, K. et al., 2000), identify specific biochemical constituents within a cell (Hellerer, T. et al., 2007; Matthaus, C. et al., 2007), identify immune cell activation (Brown, K. L. et al., 2009a, b; Mannie, M. D. et al., 2005). Several studies have also been performed to identify ideal measurement parameters for cells in culture. Research showed that the ideal collection wavelength for single cell measurements was near 785 nm (Notingher, I. et al., 2002). Lower wavelength lasers damaged cells, even at reduced power levels. It was also found that cells which were dehydrated and then tested exhibited significant artifact (Mariani, M. M. et al., 2009; Mourant, J. et al., 2003).

Cells should instead be measured while suspended in an aqueous solution. Third, water does not interfere with Raman signals because it vibrates symmetrically.

Raman spectroscopy offers several distinct advantages as a diagnostic tool. First, it does not require any biomarkers or tags (Gremlich, H.-U. Yan, B., 2001). Second, Raman signals can be measured from a broad range of molecules (Gremlich, H.-U. Yan, B., 2001). This offers a distinct advantage over infrared spectroscopy (Gremlich, H.-U. Yan, B., 2001).

1.3 The Problem and Proposed Solution

1.3.1 Raman Spectroscopy as a Diagnostic Tool for Neuroblastoma

To accurately diagnose neuroblastoma, it must be distinguished from histologically similar tumors or geographically close tumors. Current pathology methods are slow, and can be biased by the surgeon's skill in removing the affected area, and the pathologist's skill and experience in diagnosing a relatively rare pediatric neoplasm such as neuroblastoma. Methods including immunohistochemistry (Finegold, M. J. et al., 1983; Gregorio, A. et al., 2008), cytogenetics (Taylor, C. et al., 1993), polymerase chain reactions (PCR) (Chen, Q.-R. et al., 2007), electron microscopy, and karyotyping are often required in addition to traditional tissue staining and light microscopy.

Once neuroblastoma is diagnosed, the aggressiveness of the tumor must be identified. The Shimada classification is the gold standard method for diagnosing tumor favorability; however, it can vary based on the pathologist and the region of tissue under examination. Other factors such as the genetic profile of the tumor may also be examined to determine aggressiveness and plan treatment.

Raman spectroscopy can be exploited as a non-biased, quick, and accurate method for cancer diagnosis. A portable Raman instrument can be developed for biopsy use, or biopsy samples can be tested using a traditional desktop Raman spectrometer in the pathology laboratory. We hypothesize that Raman can accurately identify neuroblastoma from other neural tumors and from histologically similar small round blue cell tumors. Furthermore, we hypothesize that Raman spectroscopy can identify subtle characteristics of tumor aggressiveness such as favorability and amplification of key genes. Even if a biopsy sample were tested in the pathology lab after resection, a thorough diagnosis could be provided within an hour of surgery, instead of waiting days using current pathological methods.

1.3.2 Raman Spectroscopy as a Surgical Tool for Neuroblastoma

When a tumor is removed, the surgeon removes a margin of normal-appearing tissue outside of where he or she thinks the tumor boundaries are. The pathologist quickly cuts, stains, and views frozen sections of the margin tissue to ensure there are no remaining tumor cells and the whole tumor is removed. This process takes approximately 20 minutes, and must be repeated if tumor cells are found within the margin. Throughout this process, the surgeon and the patient's family wait, while the patient is kept sedated in the operating room.

If the pathologist's initial review shows that there are no cancer cells in the tissue margin, the surgeon finishes the surgery. However, the initial review by the pathologist is simply a best guess. Over several days, the pathologist performs a more thorough review of the tumor margin to verify that there were no tumor cells. In the case that tumor cells are found, the patient must have a second surgery to remove the remaining

cancer cells. This is expensive and puts the patient at a higher risk. Figure 1.8 shows a flow chart of the current surgical and pathology system used.

We suggest that Raman spectroscopy can be used as an alternative to the frozen section diagnosis in tumor section. Engineers are developing a hand-held Raman spectrometer for surgical use which can be used in open surgery, laparoscopic surgery, or attached to a robot arm for robotic surgery. Unlike other portable Raman spectroscopy probe designs, this design miniaturizes all the components of the spectrometer, rather than attaching a long fiber optic probe to a traditional spectrometer.

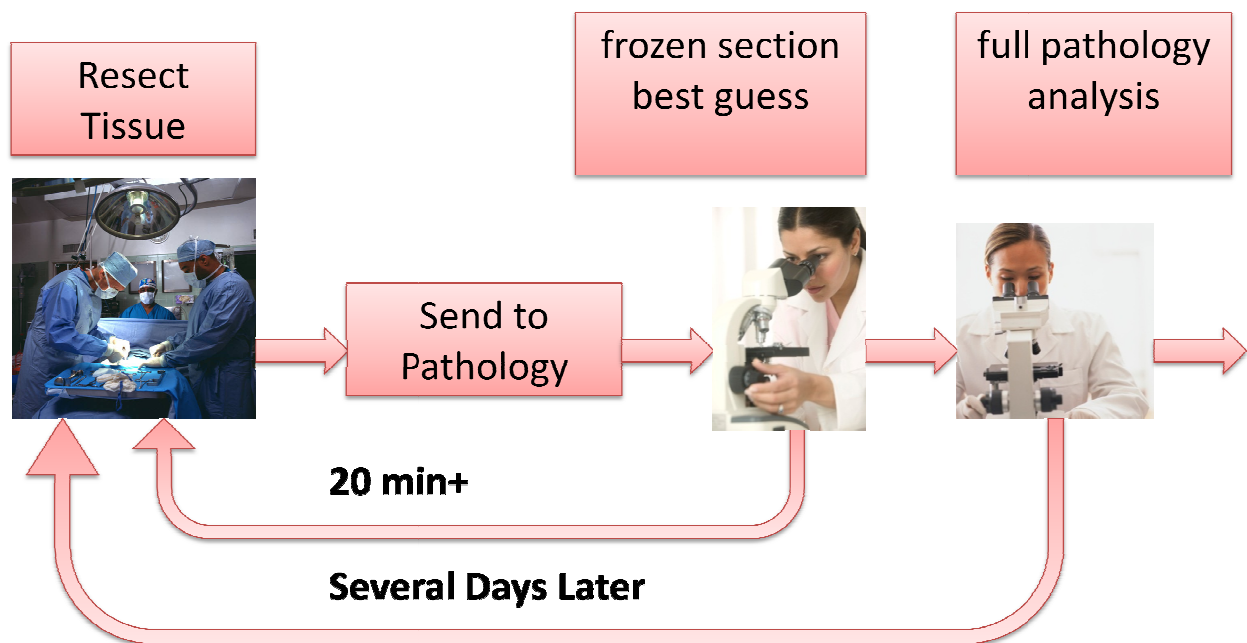


Figure 1.8: Following tumor resection, a pathologist performs a quick analysis, then a more detailed analysis. If tumor cells are found, more tissue must be removed.

Once the tumor is removed, the Raman probe can be used to scan the margin area for any remaining cells. When integrated with real time diagnostic and mapping software, this should provide an accurate assessment of the tumor margin in less than 20 minutes. The portable Raman probe could even be attached to a surgical robot to

fully automate the scanning process. A pathologist would still perform a thorough analysis of the margin following surgery, but we expect a much higher accuracy in diagnosing tumor margins.

Figure 1.9 shows a schematic of our proposed methodology. As shown, the portable Raman probe can be used in a traditional open or laparoscopic surgery, or it can be attached to a robotic arm. The probe will interface with 3-D mapping of the tumor area to scan the margin (Reisner, L. A. et al., 2007). Once scanning shows a clear margin, the surgery will end and the resected tissue will be sent to pathology for a full workup. The rate of positive margins should be much lower than the current rate, because the Raman probe should be able to obtain more detailed biochemical information about the sample. Previous studies showed that Raman spectroscopy may be able to identify abnormal, potentially pre-cancerous cells before they can be identified by pathology (Kast, R. E. et al., 2008).

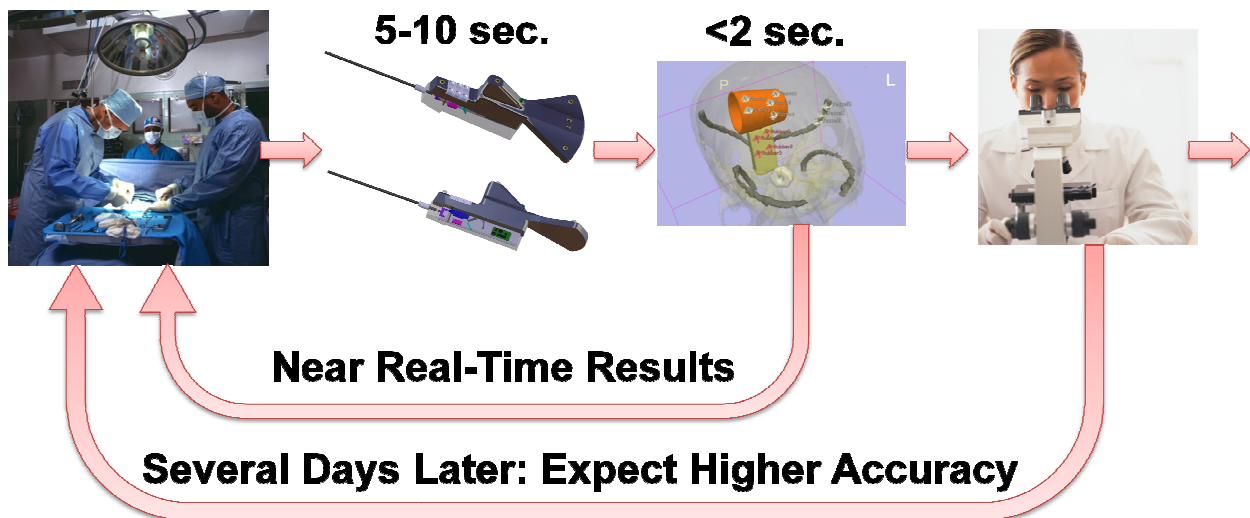


Figure 1.9: Proposed Raman system for margin assessment should provide quicker results with higher accuracy

1.4 Scope of Work

The goal of this research is to develop a detailed classification methodology for neuroblastoma. The two major steps of this goal are:

- 1) Use Raman spectroscopy to develop a methodology for identifying neuroblastoma from normal adrenal gland tissue, other neural diseases, and histologically similar small round blue cell tumors.
- 2) Use Raman spectroscopy to identify the prognostic markers of neuroblastoma to provide specific diagnostic details and allow rapid development of an optimal treatment plan.

The following hypotheses were developed based on this research goal:

- 1) Raman spectroscopy can distinguish neuroblastoma from other tissues, including histologically similar small round blue cell tumors and other pathologies of the adrenal gland, using standard histology as the gold-standard for diagnosis.
- 2) Raman spectroscopy can identify prognostic markers of the disease (tumor markers, histology, genetics, etc) to provide specific details about the diagnosis and optimal treatment plan.

1.5 Research Plan

This dissertation is divided into three main segments: identification of neuroblastoma tumor tissue, identification of prognostic markers of neuroblastoma, and conclusions and future work.

1.5.1 Identification of Neuroblastoma Tumor Tissue

Chapter 2 examines identification of neuroblastoma from normal adrenal gland tissues and from other peripheral nervous system tumors, including ganglioneuroma,

peripheral nerve sheath tumor, and pheochromocytoma. This work was originally published in the Journal of Pediatric Surgery (Rabah, R. et al., 2008).

In Chapter 3, neuroblastoma is compared to the same types of tissues; however, tumors from a frozen tumor bank were also included in the study. Because neuroblastoma and the related tumors have such low occurrence, development of a robust tissue database would take many years. If frozen tumors could be included, a database could be built more expediently. This work was also originally published in the Journal of Pediatric Surgery (Wills, H. et al., 2009a).

Chapter 4 compares neuroblastoma with the other common small round blue cell tumors, non-Hodgkin lymphoma, rhabdomyosarcoma, and Ewing sarcoma. This work was accepted for publication in the June 2010 edition of the Journal of Pediatric Surgery (Kast, R. et al., Accepted for June 2010).

1.5.2 Identification of Prognostic Markers

Chapter 5 marks the beginning of the second portion of the dissertation: identification of prognostic factors associated with neuroblastoma. In this chapter, favorable histology, unfavorable histology, and treated neuroblastoma are compared. This work was also included in the two Journal of Pediatric Surgery papers from Chapters 2 and 3 (Rabah, R. et al., 2008; Wills, H. et al., 2009b).

Chapter 6 further expands on differentiation between favorable histology neuroblastoma, unfavorable histology neuroblastoma, and treated neuroblastoma, by including frozen, blinded tumor samples received from the Children's Oncology Group, a national tumor bank.

Chapter 7 examines another prognostic factor associated with neuroblastoma: amplification of the MYCN gene. A cell line which alters its gene expression level based on tetracycline treatment was used to model normal and amplified levels of MYCN.

1.6 Novelty and Significance

This work is novel because it is the first major study using Raman spectroscopy to diagnose a pediatric tumor in a human model. Many Raman spectroscopic studies in the literature diagnose cancer in adult tissues, but this is the first investigation of neuroblastoma.

Furthermore, most of the prognostic markers of cancer have not been examined in detail. Adding this increased capability to Raman spectroscopic diagnosis will add a new degree of clinical relevance. Raman spectroscopy could offer an immediate, objective evaluation of tumor aggressiveness, and provide immediate information regarding patient prognosis. The two specific factors which will be examined are tumor histology and MYCN gene amplification.

Raman spectroscopy could offer significant improvements over existing diagnostic techniques for neuroblastoma. A methodology for real-time diagnosis would bring physicians one step closer to making immediate treatment decisions directly from the operating room. When integrated into a biopsy needle or laparoscopic surgical probe, Raman spectroscopy could provide an immediate, accurate diagnosis. This is especially significant for diagnosing small round blue cell tumors and identifying genetic amplification because existing diagnosis methods are expensive, subjective, or slow.

Accurate diagnosis could prevent patients from undergoing unnecessary treatment. Alternately, it could allow patients to begin treatment immediately based on

the real-time diagnosis. Quick identification of prognostic markers will allow rapid, individualized treatment plans.

CHAPTER 2 IDENTIFICATION OF NEUROBLASTOMA FROM NEURAL TUMORS

2.1 Introduction

Because neuroblastoma is derived from the neural crest, it can arise on sympathetic ganglia or on the sympathetic chain anywhere in the body. About one third of neuroblastomas present on the adrenal gland because it is a common site of migration for cells derived from the neural crest ("What is Neuroblastoma," 2009). This is the most common primary neuroblastoma site (Orkin, S. H. et al., 2009).

Other tumors which can arise on neural tissue include ganglioneuroma, peripheral nerve sheath tumor, and pheochromocytoma. While peripheral nerve sheath tumor and pheochromocytoma have unique histologies, ganglioneuroma is closely related to neuroblastoma.

2.1.1 *Ganglioneuroma*

As described in the introduction, ganglioneuroma is closely related to neuroblastoma (Cotran, R. S. et al., 1994). It is composed of the same types of cells of neuroblastoma, except they are mature. Ganglioneuroma is a benign condition, and usually requires no treatment. In some cases, it may need to be removed if it causes secondary symptoms

2.1.2 *Nerve Sheath Tumor and Peripheral Nerve Sheath Tumor*

A nerve sheath tumor is a neural tumor, and a peripheral nerve sheath tumor is simply a nerve sheath tumor which is found in the peripheral nervous system. There are several types of nerve sheath tumor, including Schwannoma, neurofibroma, and malignant peripheral nerve sheath tumor (Cotran, R. S. et al., 1994).

Schwannomas come from Schwann cells, which are found in the neural crest. Schwannomas are most commonly found on the eighth cranial nerve, but can be found on the other cranial nerves, in the dorsal roots of the spinal cord (and sometimes extending past the vertebral foramen), or at large nerve trunks which contain both motor and sensory nerves (Cotran, R. S. et al., 1994). Schwannomas grow attached to nerves, however, they do not invade nerves; therefore, they can typically be separated from the nerve with relative ease, as long as the tumor capsule does not surround the nerve.

Conversely, neurofibromas infiltrate the fascicles of the nerve, making it difficult to fully resect the tumor mass (Cotran, R. S. et al., 1994). Neurofibromas can be found on any nerve, though they tend to be found in larger, communicating areas more than terminal branches of the nerve. Neurofibromas consist of Schwannian cells, fibroblasts, and inflammatory cells. Since the tumor invades the actual nerve, axons can also be found within neurofibromas.

Malignant peripheral nerve sheath tumors are not caused by degeneration of Schwannomas, but they can be caused by degeneration of plexiform neurofibromas or they can occur spontaneously or as a result of radiation therapy (Cotran, R. S. et al., 1994). They are classified as sarcomas (tumor of soft tissue) and considered very malignant. Tumor recurrence and metastasis are common in malignant peripheral nerve sheath tumors, and there is a poor prognosis. Malignant peripheral nerve sheath tumors infiltrate both the host nerve as well as other local soft tissue.

2.1.3 Pheochromocytoma

Pheochromocytoma is a rare neoplasm which is found in the medulla of the adrenal gland in about 85% of cases and found on other paraganglia in the remaining 15% of cases (Cotran, R. S. et al., 1994). Less than 10% of adrenal pheochromocytomas are malignant, however 20-40% of non-adrenal pheochromocytomas are malignant. Because benign and malignant tumors share nearly identical histology, the only way to verify malignancy is the presence of metastasis.

Approximately 10% of pheochromocytomas come from familial syndromes, while the other 90% appear sporadically. Pheochromocytoma is most common in those between 40 and 60 years old, however, pediatric occurrence is common in those with familial syndromes. In the United States, the overall rate of pheochromocytoma is 1 in 100,000; however, only 10-20% of those cases occur in children (Vuguin, P. M., 2009). Pheochromocytomas tend to occur in slightly older children than neuroblastoma, with the average age at diagnosis between 6 and 14 years.

Like neuroblastoma, pheochromocytomas secrete epinephrine or norepinephrine, which lead to increased levels of catecholamines throughout the body and in the urine (Cotran, R. S. et al., 1994; Vuguin, P. M., 2009). Catecholamine release is triggered by physical or chemical changes around the tumor, rather than neural stimulation, because pheochromocytomas are not innervated. Key symptoms of pheochromocytoma are hypertension, paroxysms (strong emotional outbursts), increased levels of urinary catecholamines, and circulatory problems caused by surging

levels of catecholamines, including pulmonary edema, heart attack, congestive heart failure, cerebral hemorrhage, and ventricular fibrillation (Cotran, R. S. et al., 1994).

2.1.4 Research Goal

The goal of this chapter is to determine whether Raman spectroscopy can distinguish between neuroblastoma, ganglioneuroma, peripheral nerve sheath tumor, pheochromocytoma, and normal adrenal gland.

2.2 Materials and Methods

2.2.1 Internal Review Board Approval

All tissue-based studies described in this work were approved by the Wayne State University Internal Review Board Human Investigation Committee (IRB #0506002366). Supporting documentation, including the protocol, 2009 continuation form for 2010, and a signed approval for the 2009 continuation are included in Appendix A.

2.2.2 Data Collection

Samples of neuroblastoma, ganglioneuroma, peripheral nerve sheath tumor, pheochromocytoma, and normal adrenal gland were collected fresh from the operating room from routine surgical procedures. After arriving in the pathology lab, half of the sample was reserved for routine pathology. The other half was used for Raman spectroscopy testing. An experienced pathologist selected regions of normal tissue and/or tumor tissue for each sample.

Raman testing was performed using the Renishaw Raman spectrometer using a 20x magnification Leica objective. At least twelve different points were measured on each sample, in case any single measurement was made over non-tumor area such as

vessels, fat, or inflammation. Whenever a tissue was big enough and time allowed, more than twelve spectra were measured. Each measurement consisted of 2 or 3 accumulations of 10 seconds each over the range of 600-1800 cm^{-1} . This region is known as the fingerprint region. Raman shifts for biological molecules, including proteins, amino acids, lipids, and carbohydrates are all found within this region, and it offers the most diagnostic information.

Following Raman measurements, each sample was placed in 10% neutral buffered formalin to preserve the tissue structure, and later sent for routine histology processing. Samples were embedded in paraffin by an experienced laboratory technician, and a 5 μm section was cut, mounted on a standard glass slide, and stained with hematoxylin-eosin. The remaining tissue was preserved in paraffin. In the case of classification disagreement between the control sample and the Raman-tested sample, or in disagreements between the pathologic diagnosis and Raman diagnosis, more hematoxylin-eosin slides were made for review from the preserved paraffin-fixed sample.

All tissue slides were reviewed by two or more experienced pediatric pathologists, who agreed on the diagnosis of the tissue. In cases of neuroblastoma, pathologists also identified whether the tumor was favorable or unfavorable based on the Shimada classification, or whether the tissue was treated. Samples which displayed extensive damage due to trauma (such as cauterization during surgery) were excluded from the study. In some cases, just a few tumor cells were present in an area of otherwise normal tissue. Samples with this characteristic were included in this study, to gauge the sensitivity and specificity of the Raman technique.

2.2.3 Data Processing

Data was processed as described in section 1.2.4. Appendix B provides a detailed statement of procedure protocol for data processing. After pre-processing, each spectrum was visually examined. Spectra which showed clear measurement errors, including spectra where measurement was stopped mid-measurement, spectra where the glass slide was measured instead of the tumor or out of focus measurements were deleted from the dataset. For each group of tissues examined, the mean spectrum was calculated to get an overall understanding of the differences between tissue groups.

Data was averaged into intervals of 2.25 cm^{-1} and imported into SPSS for analysis. 2.25 cm^{-1} was selected because it was the smallest interval size which allowed SPSS to perform principal component analysis. This compressed the data from 1310 variables to 534 variables. Within SPSS, principal component analysis was used to reduce the dimensionality of the binned data set of 534 variables to 20 or less. Next, discriminant function analysis was used to build a classification model. Sensitivity (true positives / (true positives + false negatives)) and specificity (true negatives / (true negatives + false positives)) based on the gold standard diagnoses were used to judge the classification models.

The results of discriminant function analysis were examined at the spectral level and the tissue level. Because normal and tumor tissue are both heterogeneous, a given Raman spectrum may be representative of a pocket of fat, inflammation, or a vessel rather than tumor tissue. Therefore, it would not be unexpected to have a misclassified spectrum in an analysis. For this reason, a classification rule was developed for whole

tissues. Each whole tissue's classification was determined based on the classification of a majority of its spectra. For example, in a sample with 12 measured spectra, if seven or more spectra were classified as 'neuroblastoma', the whole tissue was diagnosed as neuroblastoma. Likewise, if six spectra were classified as neuroblastoma, three as normal, and three as ganglioneuroma, the overall tissue diagnosis of neuroblastoma was assigned. Usually 12 spectra were measured per sample, but that number could be more if tissue tested was large or less if some spectra from the tissue were excluded from analysis. Spectra were only excluded from analysis if they displayed clear signs of measurement error, including saturation, background signal of glass slide, or cut-off of data mid-measurement.

2.3 Results

2.3.1 Data Collected

The data consisted of 698 spectra from 31 tissue samples as shown in Table 2.1. Within the neuroblastoma group of tumors, there were 106 spectra from 6 tissue samples of unfavorable histology neuroblastoma, 114 spectra from 5 cases of favorable neuroblastoma, and 82 spectra from 5 treated neuroblastomas. As mentioned in the materials and methods section, at least twelve points were measured for each sample; however some samples were quite large and allowed significantly more measurements with no sample degradation.

Diagnosis	Number of Samples	Number of Spectra
Normal adrenal gland	3	78
Neuroblastoma	16	302
Ganglioneuroma	5	189
Nerve Sheath Tumor	6	117
Pheochromocytoma	1	12
Total	31	698

Table 2.1: Number of spectra and samples for adrenal gland, neuroblastoma, ganglioneuroma, nerve sheath tumor, and pheochromocytoma.

2.3.2 Visual Examination of Raman Spectra

The mean Raman spectrum of each tissue type and correlating representative histology images are shown in Figure 2.1. As shown, there were clear differences in the histology from tissue to tissue which correlated to clear differences in the Raman spectra. Normal adrenal gland tissue was clearly different from each of the four types of tumors. On visual inspection, normal tissues had higher peaks at 1102, 1160, and 1518 cm^{-1} , which correlates to a higher concentration of carotenoids in normal tissues (Schulz, H. et al., 2005). These peaks are circled in the normal spectrum of Figure 2.1. Note that the carotenoid peaks at 1160 and 1518 cm^{-1} were absent from the mean spectra of every tumor type.

Conversely, the tumor samples, especially ganglioneuroma and neuroblastoma had higher intensities at peaks which correlate to proteins, specifically 754, 853, 938, 1002, 1300 through 1345, 1447, 1550, 1620, and 1660 cm^{-1} .

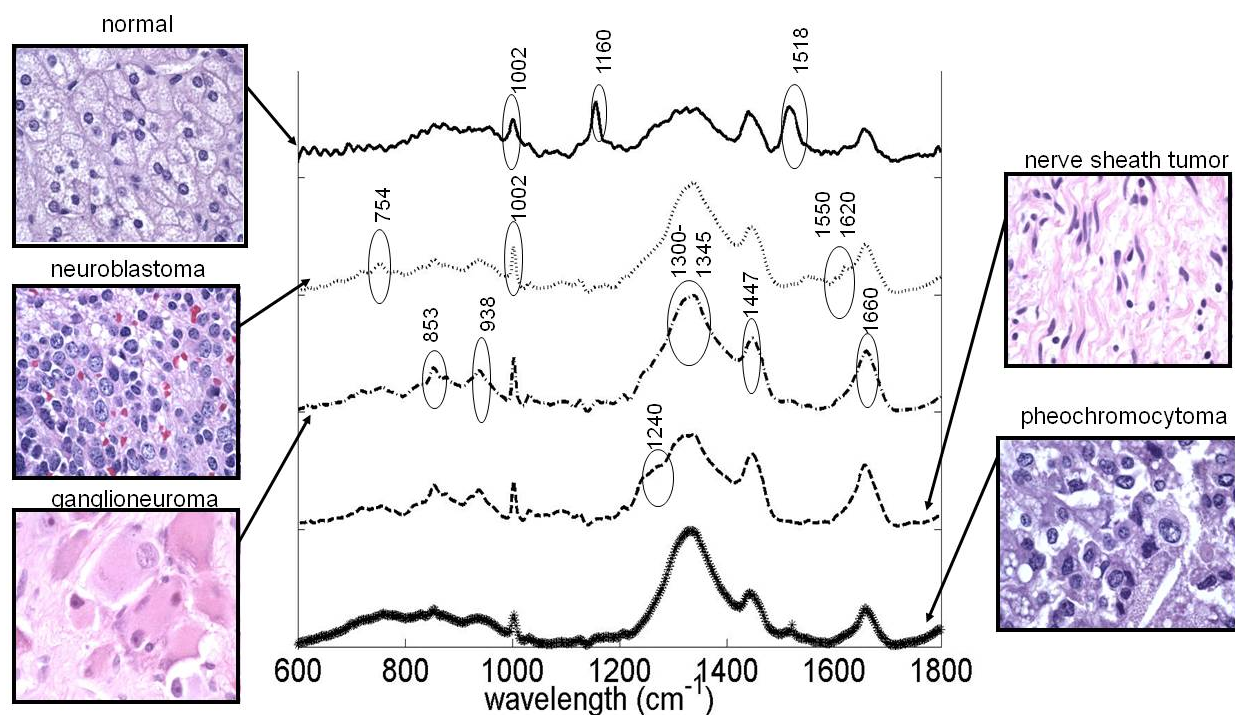


Figure 2.1: Mean spectra of each tissue type with correlating histological images. Labeled circled peaks are areas of difference between tissue types.

2.3.3

2.3.4 Classification Results

Neuroblastoma was separated from normal adrenal gland with 100% sensitivity (302/302 neuroblastoma spectra correctly identified) and 92.3% specificity (5/78 adrenal gland spectra correctly identified). The five misclassified spectra came from two tissue samples. In both cases, the misclassified spectra represented only a fraction of the overall spectra. In the first sample, 3 of 22 spectra were misclassified, and in the second sample, 2 of 44 spectra were identified. Using tissue level diagnosis, there was 100% sensitivity (16/16 neuroblastoma tissues) and 100% specificity (3/3 normal adrenal gland tissues) in diagnosing between normal adrenal gland and neuroblastoma. Classification results for this analysis and the other two-group comparisons are summarized in Table 2.2.

	Normal AG v NB		NB v GN		Normal AG v GN		NB v Pheo		NB v NST	
	Sen	Spec	Sen	Spec	Sen	Spec	Sen	Spec	Sen	Spec
Spectral-level	100%	100%	96.3%	95.7%	100%	94.8%	100%	88.1%	79.5%	85.1%
Tissue-level	100%	100%	100%	100%	100%	100%	100%	100%	66.6%	87.5%

Table 2.2: Classification sensitivity and specificity results at the spectral and tissue level for each 2-group analysis (AG = adrenal gland, NB = neuroblastoma, GN = ganglioneuroma, Pheo = pheochromocytoma, NST = nerve sheath tumor, Sen = sensitivity, and Spec = specificity)

Next, the separation between neuroblastoma and ganglioneuroma was examined. Neuroblastoma was correctly identified from ganglioneuroma with 96.3% sensitivity (291/302 neuroblastoma spectra correctly identified) and 95.7% specificity (181/189 ganglioneuroma spectra correctly identified). The eleven misclassified neuroblastoma were split between 3 tissues (2 of 18, 3 of 14, and 6 of 36 misclassified) and the eight misclassified spectra of ganglioneuroma were split between three tissues (1/55, 1 of 19, and 6 of 59 misclassified). Using the tissue-level classification, neuroblastoma and ganglioneuroma were separated with 100% sensitivity (16/16 neuroblastoma) and 100% specificity (5/5 ganglioneuroma). These results are summarized in Table 2.2.

Ganglioneuroma was separated from normal adrenal gland with 100% sensitivity (189/189 ganglioneuroma spectra correctly identified) and 94.8% specificity (74/78 adrenal gland spectra correctly identified). The four misclassified normal spectra came from two different tissues (2/22 and 2/55 spectra misclassified). The tissue level classification was 100% sensitivity and 100% specificity, as shown in Table 2.2.

A three-group analysis was performed between normal adrenal gland, neuroblastoma, and ganglioneuroma. The results are shown in Table 2.3. While each

these tissues were easy to distinguish in a two-group model, any of the three may be present in a clinical example. Overall classification was 90%, with 91% of normal adrenal gland correctly identified, 87.1% of neuroblastoma correctly identified, and 94.2% of ganglioneuroma spectra correctly identified.

Classification Results^a

Diagnosis			Predicted Group Membership			Total
			Normal	Neuroblastoma	Ganglioneuroma	
Original	Count	Normal	71	6	1	78
		Neuroblastoma	0	263	39	302
		Ganglioneuroma	0	11	178	189
	%	Normal	91.0	7.7	1.3	100.0
		Neuroblastoma	.0	87.1	12.9	100.0
		Ganglioneuroma	.0	5.8	94.2	100.0

a. 90.0% of original grouped cases correctly classified.

Table 2.3: Three-group classification results for discrimination between normal adrenal gland, neuroblastoma, and ganglioneuroma.

Figure 2.2 shows a plot of the discriminant function scores for the analysis. Normal adrenal gland spectra were represented in a single group, while there was some overlap between the neuroblastoma and ganglioneuroma groups.

Finally, neuroblastoma was compared to peripheral nerve sheath tumor and pheochromocytoma. Summarized results are shown in Table 2.2. Neuroblastoma and peripheral nerve sheath tumor were separated with 79.5% sensitivity and 85.1% specificity. At the tissue level, two neuroblastoma and two nerve sheath tumors were misclassified. Neuroblastoma and pheochromocytoma were distinguished with 100% sensitivity and 81.1% specificity at the spectral level and 100% sensitivity and specificity at the tissue level. Nerve sheath tumors and maturing neuroblastomas and ganglioneuromas both display a collagenous Schwannian stromal component. On examination of the mean Raman spectra, nerve sheath tumors had higher intensities at

854, 938, 1003, 1447, and 1657 cm^{-1} . These peaks have all been associated with protein and collagen components (Shim, M. G. Wilson, B. C., 1997).

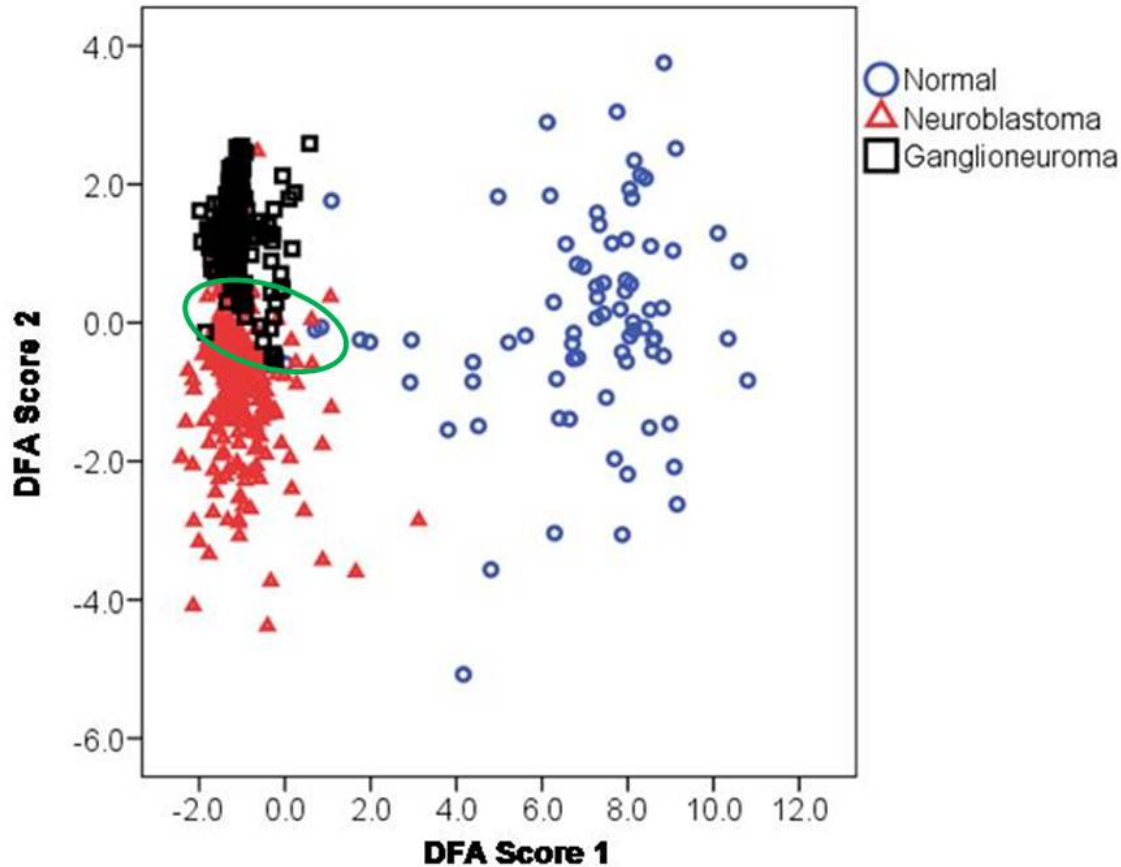


Figure 2.2: Discriminant function results show separation between normal adrenal tissue and neuroblastoma and ganglioneuroma. Results (circled) also show an overlap between neuroblastoma and ganglioneuroma.

2.4 Conclusions

This study suggests that Raman spectroscopy can be used to distinguish between neuroblastoma, adrenal gland, and other tumors of neural origin, including ganglioneuroma, peripheral nerve sheath tumor, and pheochromocytoma. Neuroblastoma was differentiated from each of these tissues with high sensitivity and specificity. This is the first study to apply Raman spectroscopy to the diagnosis of

neuroblastoma, and the first study applying Raman spectroscopy to any pediatric cancer.

Visual examination of the mean spectrum of each tissue provided biochemical support towards validating Raman spectroscopy. In general, malignant tissues had higher protein content. This is consistent with previous findings (Malini, R. et al., 2006). Likewise, neuroblastoma and ganglioneuroma had significantly lower intensities at carotenoid peaks, signifying a lower carotenoid concentration. Again, this is consistent with previous findings which suggest that carotenoids can prevent the cancer process in colon, liver, skin, lung, and mammary gland (Hata, T. R. et al., 2000).

In the future, a cancer biologist will be consulted for further biochemical analysis of experimental Raman spectra. A biologist will be able to correlate the changing biochemistry with specific biologic processes. With this knowledge, Raman can be exploited not just as a diagnostic tool, but also as a basic science tool.

Data was compressed twice before performing discriminant function analysis (binning and principal component analysis) because existing software and hardware capabilities did not allow for analysis of the full spectral data. Even this simplified analysis method was able to provide a highly accurate diagnosis.

This method, however, does not provide biochemical information about the data. In order to confirm that the peaks which were visually identified as significant are truly significant, another analysis method must be used.

When comparing two groups of tissue at a time, different pathologies could all be distinguished with 100% sensitivity and specificity, except neuroblastoma and nerve sheath tumor. This suggests that there is a level of similarity between neuroblastoma

and nerve sheath tumor. To improve this classification result, more data can be added to both groups. Alternate classification methods, such as neural networks, support vector machines, or logistic regression can also be used to try to improve classification (Krafft, C. et al., 2009).

Three-group analysis comparing normal adrenal gland, neuroblastoma, and ganglioneuroma provided 90% overall accuracy, however, neuroblastoma was only classified with 87.1% accuracy. It is notable that neither neuroblastoma nor ganglioneuroma had any spectra misclassified as normal adrenal gland. This shows a high sensitivity, as no false negatives were identified during the analysis. Because neuroblastoma is a spectrum disorder with ganglioneuroma, it is not unusual that it would be slightly more difficult to distinguish between those two diseases.

In order to further validate these results, more data must be collected and blinded studies must be performed. Because these tumors are exceedingly rare, building a database of samples fresh from the operating room would take years. Chapter 3 examines the use of frozen tissues in data analysis to develop a classification database more expediently, and Chapter 6 describes a blinded study carried out with the Children's Oncology Group to test the classification database.

CHAPTER 3 INCLUSION OF FROZEN TUMORS IN TISSUE STUDIES

3.1 Introduction

In the previous study, it was shown that Raman spectroscopy can accurately identify neuroblastoma from adrenal gland and other neural tumors, including ganglioneuroma, peripheral nerve sheath tumor, and pheochromocytoma. Conceivably, one could build an extensive Raman spectra database of these tissues which could be used to diagnose new tumor incidences.

While this finding is significant, there is still a dilemma in developing the Raman spectral database because of the low incidence of these tumors. For example, there are between 400-650 cases of neuroblastoma diagnosed annually in the United States ("What Are the Key Statistics About Neuroblastoma?," 2009; Young Jr, J. L. et al., 1986). To develop a database of these tumors at a single institution, even a pediatric-specialty hospital, would take years. Furthermore, shipping fresh samples between institutions poses another set of logistical dilemmas.

Rather than focusing on only fresh from the operating room samples, this chapter focuses on the inclusion of frozen samples into the Raman spectral database. It is known that formalin-fixed tissues are less than ideal for Raman spectroscopic measurement because the fixation causes cross-linking of the collagen proteins, thereby altering the molecular vibrations and Raman spectrum of the sample (Huang, Z. et al., 2003a). This makes formalin-preserved tissues poor candidates for database development for identification of fresh tissues.

Several investigators have used frozen tissue samples in their Raman spectroscopic investigations (Crow, P. et al., 2005b; Haka, A. S. et al., 2005), however there is minimal, if any literature pertaining to the validity of frozen tissue use.

A histologic study performed on frozen liver and heart tissues showed smaller cells after freezing, with larger extracellular spaces. The changes became more pronounced over time. Furthermore, specific types of tissue react differently to freezing. For example, skeletal muscle and skin tend to harden after the freeze-thaw cycle, whereas spleen and brain tissues tend to soften (Schäfer, A. T. Kaufmann, J. D., 1999). It is not known how such changes would affect Raman spectroscopic measurements of frozen tissues.

A 1996 study recommended that the optimal preservation method for samples to be tested with Raman spectroscopy was freezing in optimal cutting temperature medium (OCT) (Shim, M. G. Wilson, B. C., 1996). While many researchers seemed to follow similar guidelines, there was little attention paid to the advances in measurement technique and processing since the time this paper was published. For example, the spectral resolution of the system described by Shim was 8 cm^{-1} ; the resolution of the system used for studies described in this text was 3 cm^{-1} .

3.1.1 Research Goal

The goal of this chapter is to determine whether Raman spectra of frozen tissues are a valid replacement for measurements of fresh tissues. This was studied in-depth in 1996, but has not been re-examined in the literature since then, even with major technological advances in Raman spectroscopic measurement and analysis. Spectra of peripheral nervous system tumors were collected frozen and compared to that of the

tumors measured fresh in Chapter 2. To judge classification, frozen tissues were classified based on a fresh model, and fresh tissues were classified based on a frozen model.

3.2 Materials and Methods

3.2.1 Data Collection from Fresh Tumors

The Raman spectra collected and described in Chapter 2 were used as the fresh samples for this study. Any fresh samples which became available throughout the period of data collection for frozen tumors were also included in the study. In these cases, the sample was divided into a piece for routine pathology and a piece for Raman spectroscopy, as described previously. In this case, however, the portion reserved for Raman spectroscopy was further divided into a piece to test fresh and a piece to test frozen, if enough tissue was available. The portion set aside to test frozen was placed in a labeled cryovial or eppendorf tube, and then put in the freezer for testing at a later date. All fresh tissues tested were preserved in formalin and later cut and stained for histology review by a trained pathologist as described in Chapter 2.

3.2.2 Data Collection from Frozen Tumors

Prior to initiating this study, a preliminary study was performed on fresh (never frozen) and frozen chicken muscle, fat, and bone obtained from a butcher to determine the best protocol for testing frozen samples (results not published). Information from a literature review was also used to develop the frozen tumor measurement protocol.

Whenever there was excess fresh tissue available from a pathology case, it was placed in a cryovial with no preservatives or fixatives, labeled, and put in a -80°C freezer to freeze slowly. The minimum freezing time for a sample was 24 hours;

however, some samples were banked by pathologists for several years, and then pulled for Raman testing.

Before Raman testing, the sample was removed from the freezer. The cryovial was filled with room-temperature saline and the specimen was allowed to defrost for 30 minutes. When the sample was thoroughly defrosted, it was removed from the vial and placed on a glass microscope slide for Raman testing. At this point, the sample was measured with the same procedures as the fresh samples, described in section 2.2.2. Following measurement, the sample was placed in fixative and sent for routine pathology testing.

3.2.3 Data Processing and Analysis

Raw data was stored on a secure server, and measurement parameters were stored in a customized database. Raw files were preprocessed, reviewed, binned, and imported into SPSS as described in Chapter 2 and Appendix B.

Data was then split into two groups: spectra which were measured from fresh specimens (called 'fresh' hereafter), and spectra which were measured from frozen, defrosted specimens (called 'frozen' hereafter). Principal component analysis and discriminant function analysis were performed on the fresh data, and then both models were applied to the frozen data. This showed how well the fresh data model could classify the frozen data. Next, principal component analysis and discriminant function analysis were performed on the frozen data, and then applied to the fresh data. This showed how well the frozen data model could classify frozen data. For each comparison, separate models were created.

Sensitivity, specificity, and accuracy were used to judge the classification methodologies. They were calculated at the spectral level and at the tissue level, where the tissue diagnosis was made based on the majority of the individual spectra.

3.3 Results

62 tissues were measured for this experiment. 45 of the samples were only measured fresh. Three samples came from the frozen tumor bank and were only measured frozen. Fourteen samples were split and tested both fresh and frozen.

The resulting data set consisted of 862 Raman spectra from 59 fresh tissue samples, and 252 Raman spectra from 17 frozen tissue samples. Table 3.1 shows the exact number of spectra measured for each fresh and frozen tissue type, as well as the total number of specimens examined.

	Fresh		Frozen		Total Spectra
	Specimens	Spectra	Specimens	Spectra	
Adrenal Gland	8	69	1	9	78
Neuroblastoma	26	416	11	141	557
Ganglioneuroma	14	206	2	22	228
PNST	8	117	1	12	129
Pheochromocytoma	3	54	2	68	122
Total	59	862	17	252	1114

Table 3.1: Number of fresh and frozen specimen and spectra measured for each type of tissue.

Figure 3.1 shows the fresh and frozen mean spectrum for each tissue type. Notice that overall, there is close correlation between fresh and frozen. Most peaks were preserved along the x-axis (wavenumber) with only minor shifts in the vertical axis (intensity).

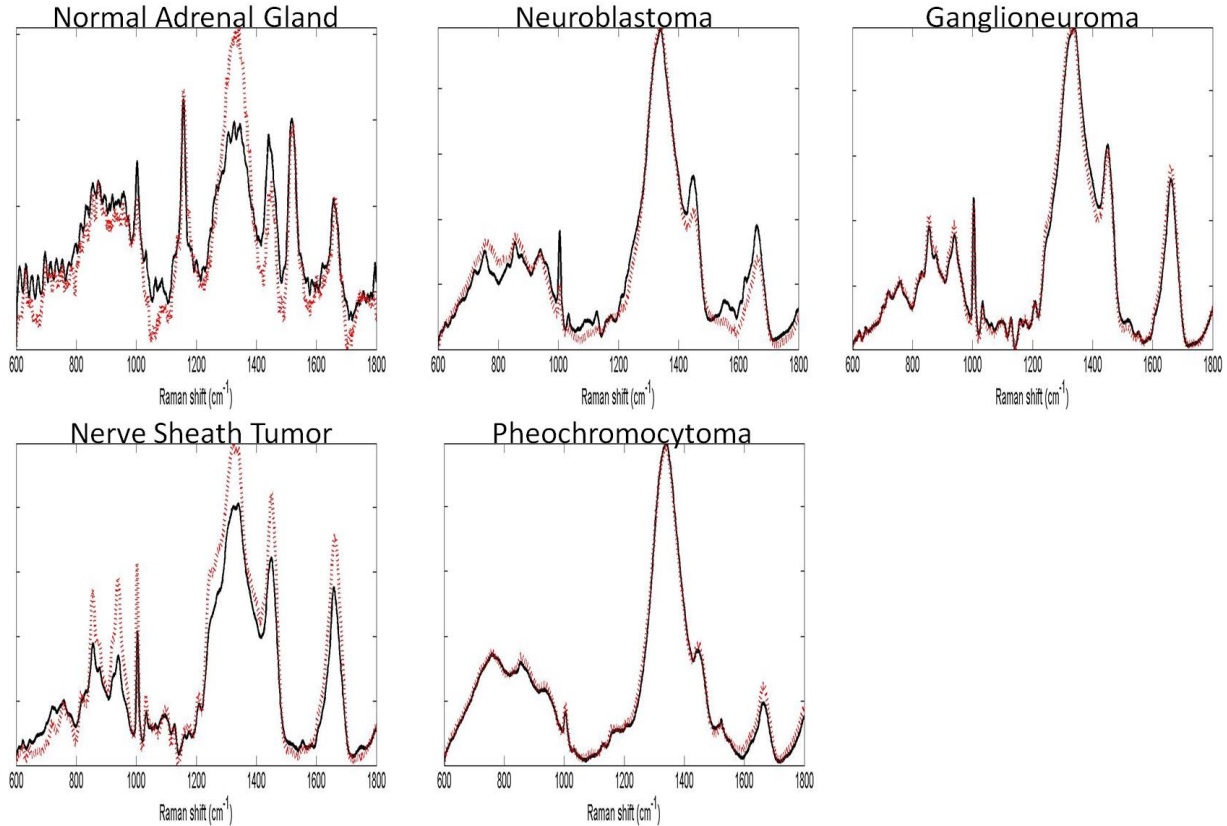


Figure 3.1: Mean fresh (solid black line) and frozen (dotted line) spectra of normal adrenal gland, neuroblastoma, ganglioneuroma, nerve sheath tumor, and pheochromocytoma.

Table 3.2 compares the tissue-level classification results using frozen data tested on a fresh model, fresh data tested on a frozen model, and fresh-only results obtained in Chapter 2. Table 3.3 shows the same results at the spectra-level.

When *frozen* data was tested with the *fresh* model, normal adrenal gland was distinguished from neuroblastoma, ganglioneuroma, nerve sheath tumor, and pheochromocytoma with 100% sensitivity and specificity. Likewise, neuroblastoma and ganglioneuroma were separated with 100% sensitivity and specificity at the tissue level.

When *fresh* data was tested against the *frozen* model, normal adrenal gland was distinguished from neuroblastoma, ganglioneuroma, and pheochromocytoma with 100% sensitivity and specificity at the tissue level. All normal tissues were distinguished from

nerve sheath tumor, but one of seven nerve sheath tumors was classified as normal adrenal gland tissue. When neuroblastoma and ganglioneuroma were compared, 5 of 14 ganglioneuroma were misclassified as neuroblastoma, and 5 of 26 neuroblastoma were misclassified and ganglioneuroma.

	NB v Normal		GN v Normal		NST v Normal		Pheo v Normal		NB v GN	
	Sen	Spec	Sen	Spec	Sen	Spec	Sen	Spec	Sen	Spec
Fresh Model Frozen Test	100	100	100	100	100	100	100	100	100	100
Frozen model Fresh test	100	100	100	100	87.5	100	100	100	80.8	64.3
Fresh only (Chapter 2)	100	100	100	100	100	100	100	100	100	100

Table 3.2: Tissue-Level Classification Results (results shown are percentages; (AG = adrenal gland, NB = neuroblastoma, GN = ganglioneuroma, Pheo = pheochromocytoma, NST = nerve sheath tumor, Sen = sensitivity, and Spec = specificity)

Frozen ganglioneuroma and nerve sheath tumor were classified from frozen adrenal gland with 100% sensitivity and specificity. All 141 frozen neuroblastoma spectra were correctly separated from frozen adrenal gland when tested against the fresh model; however two of nine of the frozen adrenal gland spectra were called neuroblastoma. Only one of 68 pheochromocytoma spectra was misclassified when compared to adrenal gland. All adrenal gland spectra were correctly identified from pheochromocytoma when frozen spectra were tested with the fresh model. When neuroblastoma and ganglioneuroma were compared, just 1 of 141 neuroblastoma spectra was misclassified. All ganglioneuromas were correctly identified.

	NB v Normal		GN v Normal		NST v Normal		Pheo v Normal		NB v GN	
	Sen	Spec	Sen	Spec	Sen	Spec	Sen	Spec	Sen	Spec
Fresh Model Frozen Test	100	77.8	100	100	100	100	98.5	100	100	99.3
Frozen model Fresh test	98.8	91.3	100	91.3	86.3	97.1	100	88.4	84.1	69.9
Fresh only (Chapter 2)	100	92.3	100	94.8	100	94.9	100	97.4	95	96

Table 3.3: Individual Spectra Classification Results (results shown are percentages; (AG = adrenal gland, NB = neuroblastoma, GN = ganglioneuroma, Pheo = pheochromocytoma, NST = nerve sheath tumor, Sen = sensitivity, and Spec = specificity)

When *fresh* neuroblastoma was compared to normal adrenal gland based on the *frozen* model, only 5 of 416 neuroblastoma and 6 of 69 adrenal gland spectra were misclassified. When ganglioneuromas were compared to adrenal gland, 6 of 69 adrenal gland spectra were misclassified and all ganglioneuroma spectra were correctly identified. 16 of 117 nerve sheath tumor and 2 of 69 adrenal gland spectra were misclassified when those groups were compared. 3 normal adrenal gland spectra were misclassified when compared to pheochromocytoma. All pheochromocytoma spectra were identified correctly.

3.4 Conclusions

This study showed that a fresh tissue model could be used to classify frozen tissues, and a frozen tissue model could be used to classify fresh tissues. Normal adrenal gland tissue was separated from neuroblastoma, ganglioneuroma, nerve sheath tumor, and pheochromocytoma, and neuroblastoma was distinguished from ganglioneuroma with high sensitivity and specificity at the tissue level and at the

spectral level. The tissue-level and spectra-level results obtained were comparable to the results found in Chapter 2 using only fresh tissues.

Likewise, there was high correlation between the mean fresh and frozen spectrum for each type of tissue. There was little horizontal shift in peaks, although there were some differences in peak intensities. Some of these differences appear to be due to normalization or background subtraction of the original data. Fine-tuning of background subtraction methods may make the differences between fresh and frozen tissues even more subtle. For example, the mean fresh Raman spectra of both normal adrenal gland and nerve sheath tumor display maximum values around 0.75, while a maximum value of 1 would be expected. This could signal that there are multiple populations within the data where background subtraction created maximum values at points other than $\sim 1320 \text{ cm}^{-1}$. Further review of the individual spectra for both fresh groups could show populations being normalized to different wavenumbers. This could signal multiple populations within the data, or it could signal multiple background fluorescence signals which are not properly or uniformly subtracted using the existing automatic background subtraction methodology.

In the cases of normal adrenal gland, ganglioneuroma, and nerve sheath tumor, less than 25 spectra were collected from frozen tissue. With a sample size this small, differences from the mean fresh spectra might simply be due to measurement of a non-tumor area, or purely from the small sample size.

Other reasons for differences between the fresh and frozen mean spectra from each tissue type could be caused by physical changes to the tissue caused by freezing. For example, when the cell membranes rupture, it disrupts the molecular bonds within

the cell wall. This will contribute to changes in the Raman signature, but it is not known how strong the impact will be.

Classification results of fresh tissue based on a frozen model were less than 100% in some cases. The size of the frozen tissue model was substantially smaller than that of the fresh tissue model (about $\frac{1}{4}$ of the total data). Every group except neuroblastoma only had one or two frozen cases. This does not offer enough variation to build a robust classification model. As more samples are added to the frozen tissue model, classification of new, unknown tissues should improve dramatically.

Additionally, a histological review of the frozen tissue sections offers another potential cause for misdiagnosis. Within the subset of frozen neuroblastoma tissues, one case of neuroblastoma was actually a ganglioneuroblastoma which had distinct regions of mature ganglioneuroma cells with islands of immature neuroblasts. Tissues were classified as neuroblastoma even if they had only a few neuroblast cells. Although the tissue in question looked predominantly like a ganglioneuroma, it was still called neuroblastoma because of the presence of neuroblast cells. It is possible that Raman measurement missed these islands of neuroblast cells. In the future, detailed scanning studies will determine the optimal minimum area to be measured with each scan.

Another tissue was a chemotherapy-treated neuroblastoma which had mostly mature cells with a region of immature neuroblast cells which appeared to be from a different clone than the mature cells. Because 2 out of 11 (18%) of the neuroblastoma samples in the frozen training model displayed non-textbook histology, this could cause a skew to the frozen tissue model.

The overall results suggest that the tissue changes due to the freeze-thaw process may not be significant in Raman diagnosis. While it is known that freezing causes cells to shrink, and may cause rupture of cells by ice crystals, it has not yet been specifically defined how this would alter the Raman spectrum (Schäfer, A. T. Kaufmann, J. D., 1999). For the time being, it does appear that inclusion of frozen tumor samples in studies applied to fresh tissues is still a valid technique.

This study implies that it might be possible to build a classification model based on frozen tissues from a cryopreserved tissue bank which could then be used to classify fresh tissues. This would allow rapid development of a large database of tissues which could include both common and extremely rare tissues. When Raman spectroscopy is combined with real-time software and a diagnostic model, nearly any tissue could be identified, potentially even from the operating room. An immediate diagnosis would offer a huge advantage over the traditional frozen section diagnosis. Frozen section diagnosis takes 20-30 minutes, and does not guarantee 100% accuracy. Raman might offer a near-real-time alternative with accuracy at least as good as the frozen section.

Furthermore, with proper privacy practices established, Raman spectra collected from a frozen tumor bank can be combined with other patient information, including treatment information and outcome. It might be used to determine the optimal treatment method or measure the effect of chemotherapy throughout treatment.

CHAPTER 4 IDENTIFICATION OF NEUROBLASTOMA FROM SMALL ROUND BLUE CELL TUMORS

4.1 Introduction: Small Round Blue Cell Tumors

The purpose of the previous chapters was to identify neuroblastoma from adrenal gland, it's most common origin site, and from other neural-derived tumors, including ganglioneuroma, nerve sheath tumor, and pheochromocytoma. The goal of this chapter is to distinguish neuroblastoma from other tumors which have similar histology but which are not neural-derived. In cases where neuroblastoma is found outside the adrenal gland, it must also be distinguished from these histologically similar tumors.

Neuroblastoma is a small round blue cell tumor (SRBCT). The main types of small round blue cell tumors are neuroblastoma, Ewing sarcoma, rhabdomyosarcoma, and non-Hodgkin lymphoma (Chen, Q.-R. et al., 2007; Gregorio, A. et al., 2008). Differentiation between these types of tumors is difficult, especially when the clinical context is unusual. Accurate diagnosis is essential with small round blue cell tumors because the treatment methods vary for each type of tumor (Chen, Q.-R. et al., 2007). Most commonly, diagnostic confusion occurs when a tumor metastasizes to a distant location, or when the tumor presents as a large mass in the abdomen and the exact origin cannot be determined (Orkin, S. H. et al., 2009).

The mean age at diagnosis for neuroblastoma, non-Hodgkin's lymphoma, Ewing sarcoma, and rhabdomyosarcoma are shown in Table 4.1 (Cotran, R. S. et al., 1994).

0-4 years old	5-9 years old
Neuroblastoma	Neuroblastoma
	Ewing's Sarcoma
Rhabdomyosarcoma	
	non-Hodgkin Lymphoma

Table 4.1: Most commonly diagnosed ages for each small round blue cell tumors.

4.1.1 Non-Hodgkin Lymphoma

Non-Hodgkin lymphomas are derived from lymph tissue and its cells, including lymphocytes, histiocytes, and their precursor cells. Non-Hodgkin lymphoma encompasses several sub-types, and a variety of systems exist for their classification. The most widely-accepted grouping is the 'World Health Organization Classification of Tumors of the Hematopoietic and Lymphoid Tissues'. This separates tumors based on the parent cell (B-cell, T-cell, or natural killer cell), then further groups tumors based on histology, genetics, immunophenotype, and clinical presentation. Pediatric tumors of B-cell origin include Burkitt's lymphoma, diffuse large B-cell lymphoma, and primary mediastinal large B-cell lymphoma (Orkin, S. H. et al., 2009). T-cell originating tumors include anaplastic large cell lymphoma and peripheral T-cell lymphoma.

4.1.2 Ewing Sarcoma

Ewing sarcomas are found predominantly in bone, though they can also be found in other soft tissues. Histologically, the tumor cells often appear to be of neural origin (Cotran, R. S. et al., 1994) and show similar histology patterns to neuroblastoma, however the progenitor cells may actually be mesenchymal stem cells (Meltzer, P. S., 2007).

4.1.3 Rhabdomyosarcoma

Rhabdomyosarcoma is the most common soft tissue tumor in children (Cotran, R. S. et al., 1994). The progenitor cell is the rhabdomyoblast, which is a primitive muscle cell. In the arms and legs, rhabdomyosarcoma is typically associated with skeletal muscle, however, in the rest of the body, it is typically found in areas with

minimal skeletal muscle, including the retroperitoneum, head and neck, and genitourinary track.

Embryonal rhabdomyosarcoma, including botryoid type, is the most common subtype of rhabdomyosarcoma (Cotran, R. S. et al., 1994). It is typically diagnosed in children less than 10 years old. The rhabdomyoblasts mimic muscle cells at differing points of embryonic development, including both round cells and spindle cells.

4.1.4 Existing Diagnostic Methods for Small Round Blue Cell Tumors

There are several methods for differentiating specific types of small round blue cell tumors, including immunohistochemistry (Finegold, M. J. et al., 1983; Gregorio, A. et al., 2008), cytogenetics including fluorescence in situ hybridization (Taylor, C. et al., 1993), and polymerase chain reactions (PCR) (Chen, Q.-R. et al., 2007), and complementary DNA microarrays (Khan, J. et al., 2001).

One of the more common methods uses groups of antibodies which recognize markers within specific types of tumors (Gregorio, A. et al., 2008). This is known as immunohistochemistry. There is no single antibody or test, however, which can clinically differentiate all the sub-types of small round blue cell tumors. Most research in developing diagnostic tests for small round blue cell tumors involves searching for new antibodies which can better identify tumor markers of the specific tumor types (Gregorio, A. et al., 2008). The downside of immunohistochemical methods is that they can only examine one protein or tumor marker at a time (Chen, Q.-R. et al., 2007).

Khan et al. used complementary DNA (cDNA) microarrays to identify 131 genes which have diagnostic capability for small round blue cell tumors (Khan, J. et al., 2001). They were able to predict disease classification using supervised clustering methods.

In 2007, the National Cancer Institute and Althea Technologies announced a methodology "capable of accurately differentiating the common forms of the disease: neuroblastoma, rhabdomyosarcoma, non-Hodgkin's lymphoma, and Ewing's family of tumors" ("Althea Technologies Announces the Development of a Diagnostic Capable of Differentiating Multiple Forms of Childhood Cancer," 2007). It allows a diagnosis based on a single test, rather than a series of up to six immunohistochemistry tests. The test was developed by using complementary DNA microarrays to identify genes which have diagnostic capabilities (Chen, Q.-R. et al., 2007). 39 total genes were selected for the final test, and neural networks were used to build a classification model. Next, a reverse transcription polymerase chain reaction (PCR) assay was developed to measure the gene levels and make a tissue diagnosis (Chen, Q.-R. et al., 2007).

The PCR test developed by Chen et al. is simpler and cheaper than the standard immunohistochemistry methods, and the required sample size is much smaller (Chen, Q.-R. et al., 2007). The turnaround time, however, is still 48 hours, and samples must be sent to an outside lab for the testing. The test and laboratory were CLIA certified in 2009 and began the FDA approval process. The test is still not real time, however, and it requires a specialized lab and lab technician to perform the test. The test began FDA testing in 2009 ("Childhood Cancer Panel," 2008).

Raman spectroscopy offers several distinct advantages over this test, which is the current 'state-of-the-art'. A Raman diagnosis can be made in minutes, right from the operating room or pathology lab without the need for specialized laboratory equipment or technicians. Sensitivity and specificity of previous work, including identification of neuroblastoma from other nervous system tumors are comparable to the sensitivity of

the Althea Technologies test. Assuming similar results in identification of small round blue cell tumors, Raman spectroscopy could offer equally accurate results in a fraction of the time.

4.2 Materials and Methods

4.2.1 Sample Measurement

Fresh and frozen samples of untreated neuroblastoma, Ewing sarcoma, rhabdomyosarcoma, and non-Hodgkin lymphoma were collected fresh from the operating room or frozen from our tumor bank. Frozen tissues were included in the study without confirmatory analysis because our results from Chapter 2 suggested frozen tissues were comparable to their frozen counterparts.

Half of each tumor sample was used for routine pathology, and half was used for Raman analysis using the same protocols described in Chapters 2 and 3. Because the small round blue cell tumors display extremely similar histological characteristics, pathology techniques other than light microscopy were necessary for tumor diagnosis. Other techniques which were used to diagnose the control pathology tissue sample include conventional karyotyping, FISH analysis, immunohistochemical staining, and electron microscopic examination as needed.

After Raman measurement, a hematoxylin-eosin slide was created from the Raman sample to confirm tumor presence in that region of tissue. Pathology diagnosis was not made based on microscopy review of the Raman sample, however, the pathologist did confirm that the Raman sample had similar histology to the gold standard pathology sample. In order to ensure the 'purest' samples, all treated tumors, tumors which displayed sparse malignant cells, and tumors with tissue damage such as

necrosis, freezing artifact, or trauma from surgery were excluded from the study. This selection process was more rigorous than that used for identification of neural-derived tumors, but it ensured that all samples included were predominantly composed of viable tumor. The goal of this study was to distinguish different types of tumors, rather than distinguish tumors from normal tissue. This is the reason for exclusion of less than pure tumor samples.

4.2.2 Data Processing

Data was pre-processed, binned, and imported into SPSS as described in Chapter 2. A mean spectrum was calculated for each type of tumor. Confirmatory analysis using Principal Component Analysis and Discriminant Function Analysis was performed to ensure that the tissues could be separated.

Once confirmatory analysis proved successful, a more detailed analysis was performed to identify specific peaks or regions of peaks which were diagnostically significant. Preprocessed, unbinned data were entered into SPSS. Unbinned data was used to obtain the most detailed possible information about the relevant peaks. Discriminant function analysis was performed on this data. The table containing the standardized canonical discriminant functions was exported from SPSS. This table contained a list of all peaks which were diagnostically significant in the analysis; however, one drawback of this table is that it tended to give higher significance to peaks with lower wavenumbers. This is purely because they were entered into the analysis first.

To combat this issue, the standardized canonical discriminant functions were further tested to reach the optimal combination of diagnostic peaks. Some of the peaks

represent redundant variation that is already explained by other peaks, and others are due to artificial weighting at the lower wavenumbers. An iterative process was followed to remove redundant peaks and come to as small of a peak set as possible.

First, all the peaks from the standardized canonical discriminant functions table were entered into a discriminant function analysis. A peak or a combination of peaks was then removed from the list and the discriminant function analysis was run again. Initially, a peak was selected for removal if it had a low standardized canonical discriminant function value, or if it was very close to another peak(s) included in the standardized canonical discriminant functions (such as 745, 746, 748 cm^{-1}).

If the classification results improved, the peak could safely be removed from the analysis. If the classification results got worse, the peak was again included in the analysis, and a new peak was selected for removal. The process of peak removal continued in this manner until all peaks in the model were tested, and none could be removed without lowering classification results. The peak selection process is illustrated in a flowchart in Figure 4.1.

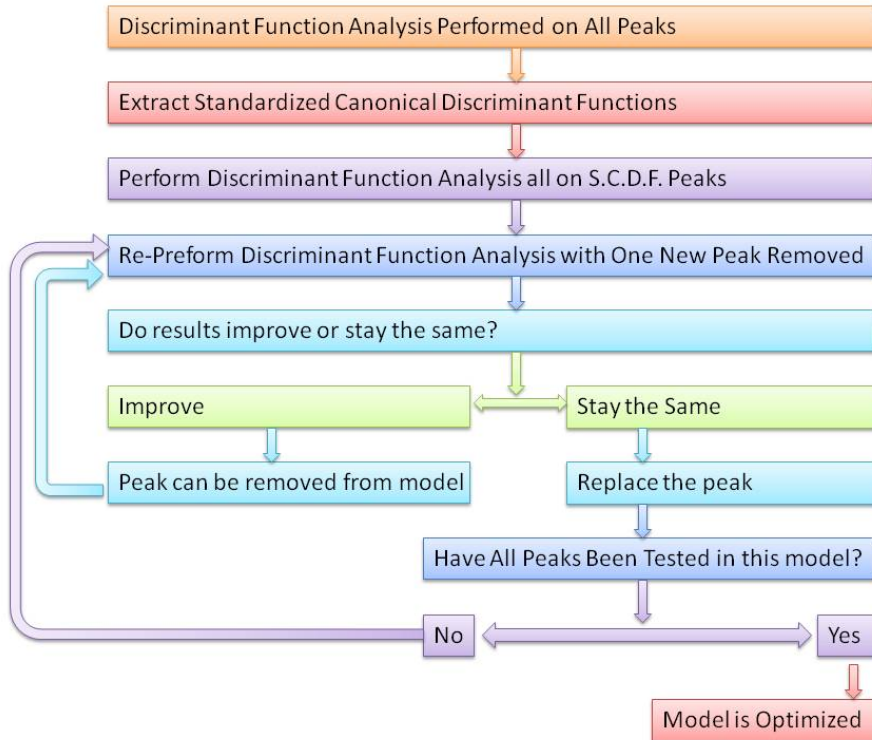


Figure 4.1: Decision Tree for discriminant function analysis peak selection

When the in-depth peak analysis was performed, a peak was excluded due to a low weighting value in the standardized canonical discriminant function table, or because it was a low wavenumber, or because there were two adjacent peaks which did not likely offer and more diagnostic ability than a single peak. After several peaks were removed, it became more difficult to judge which peaks could be removed. In this case, peaks were removed one-by-one until a peak which was not necessary for analysis was found.

Once the maximal spectral classification was reached, each tissue was again assigned an overall diagnosis. In the future, when an optimal classification model is determined, new tissues can be quickly diagnosed using the same model. As the size

of the data set increases, however, the data model should be revisited for validation purposes.

The combination of peaks which provided the highest diagnostic accuracy using discriminant function analysis was found. Then, the minimum combination of peaks which was necessary to identify all tissues with 100% accuracy was found. Data was analyzed at the individual spectra level, and then the tissue level results were calculated using the majority spectra rule.

4.3 Results

4.3.1 Tissues Studied

Table 4.2 shows the data available for this study. The data set included 179 neuroblastoma spectra from 9 surgical cases, 37 Ewing sarcoma spectra from 3 surgical cases, 100 non-Hodgkin lymphoma spectra from 6 surgical cases, and 164 rhabdomyosarcoma spectra from 4 surgical cases. Because some tumors had a large volume of viable tumor tissue, multiple samples were taken from some surgical cases.

	Surgical Cases	Samples	Spectra
Neuroblastoma	9	11	179
Ewing Sarcoma	3	3	37
non-Hodgkin Lymphoma	6	7	100
Rhabdomyosarcoma	4	11	164
TOTAL	22	32	480

Table 4.2: Samples and spectra used for identification of neuroblastoma from other small round blue cell tumors.

4.3.2 Visual Inspection of Raman Spectra

The mean spectrum and a representative hematoxylin-eosin microscopy image for neuroblastoma, Ewing sarcoma, non-Hodgkin lymphoma, and rhabdomyosarcoma

are shown in Figure 4.2. There were clear differences between each of the tissues. Some of the obvious changes are circled in Figure 4.2.

Neuroblastoma lacked the shoulder region in the range 1230.5-1275.0 cm^{-1} . It had a distinct signature in the range of 1500-1659 cm^{-1} , but it was not as predominant as the signature for Ewing sarcoma.

753.7, 1230.5, and 1630.9 cm^{-1} are all associated with tryptophan. Ewing sarcoma had the highest intensity at each of these peaks. It also had the highest value at the diagnostic peaks 1540.6, 1567.2, 1571.5, 1608.9, 1630.9, 1653.7, and 1655.4 cm^{-1} , which were all within the range of 1500-1659 cm^{-1} where it had a strong signature. Finally, Ewing sarcoma had a significant valley at 793.5 cm^{-1} which was not present in the other tissues.

The rhabdomyosarcoma and non-Hodgkin lymphoma spectra displayed only slight differences from each other. They lacked the strong signature between 1500 and 1659 cm^{-1} which was present in neuroblastoma and Ewing sarcoma. Rhabdomyosarcoma had a strong shoulder from 1230.5-1275.0 cm^{-1} while non-Hodgkin lymphoma had only a subtle shoulder. Other characteristics which visually distinguished non-Hodgkin lymphoma from rhabdomyosarcoma were higher-intensity peaks at 1092.5 and 1446.1 cm^{-1} in non-Hodgkin lymphoma.

4.3.3 Confirmatory Analysis

Confirmatory analysis correctly classified 90.4% of spectra using principal component analysis and discriminant function analysis. At the tissue level, all samples were correctly correlated with the pathology gold-standard as neuroblastoma, Ewing sarcoma, non-Hodgkin lymphoma, or rhabdomyosarcoma.

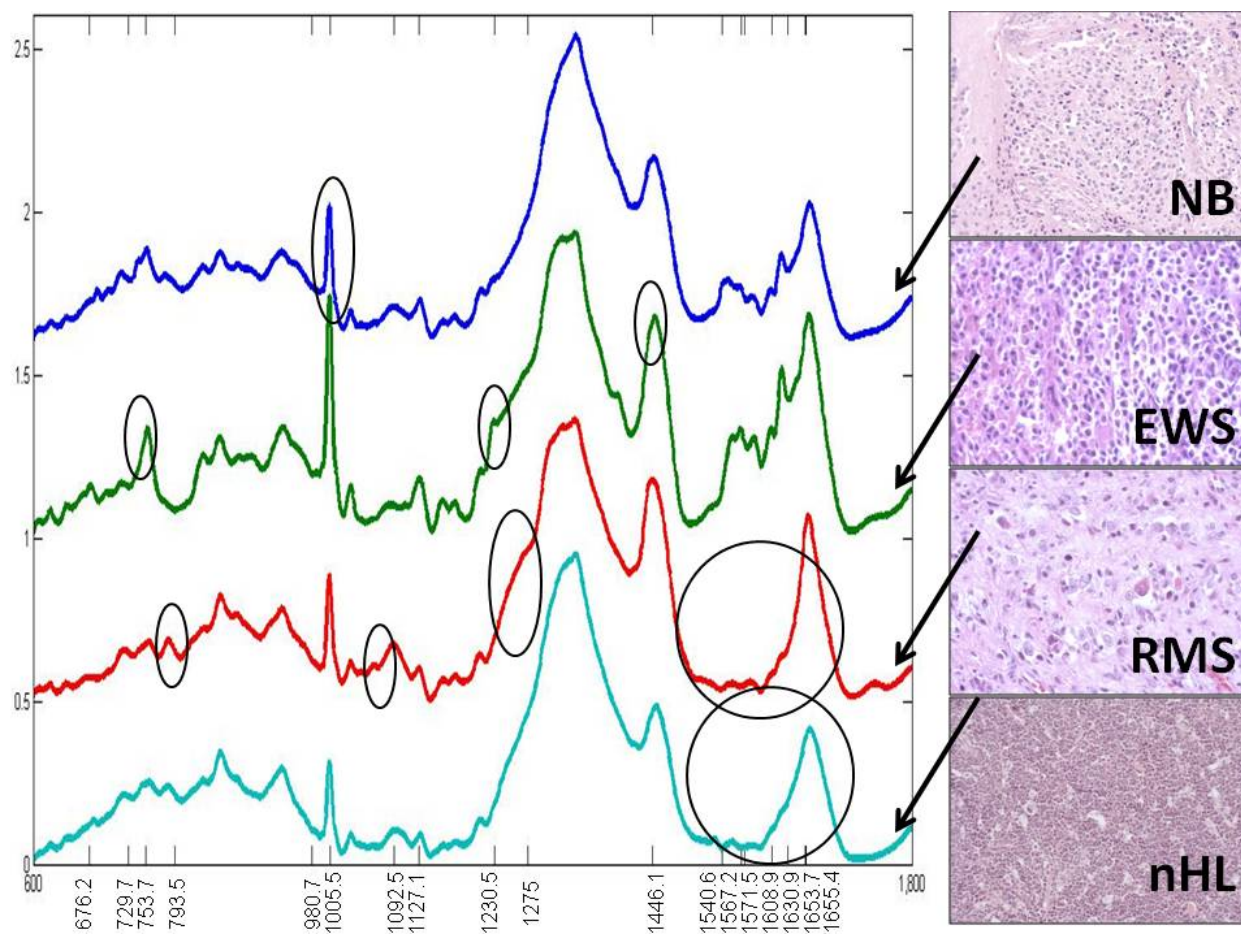


Figure 4.2: mean spectrum and histology images of neuroblastoma, Ewing sarcoma, rhabdomyosarcoma, and non-Hodgkin lymphoma with key diagnostic peaks marked.

4.3.4 Peak-by-Peak Analysis

Using, leave-one-out discriminant function analysis, 18 peaks identified neuroblastoma, Ewing sarcoma, non-Hodgkin lymphoma, and rhabdomyosarcoma with 94% accuracy. All sample-level diagnoses were correct. The 18 peaks were 676.2, 729.7, 753.7, 793.5, 980.7, 1005.5, 1092, 1127.1, 1230.5b 1275.0, 1446.1, 1540.6, 1567.2, 1571.5, 1608.9, 1630.9, 1653.7, and 1655.4 cm^{-1} . They are marked on Figure 4.2.

When determining the minimum number of peaks necessary to classify all tissues with 100% accuracy, only the following 10 peaks were needed: 676.2, 729.7,

793.5, 980.7, 1092.5, 1230.5, 1275.0, 1571.5, 1608.9, and 1655.4 cm^{-1} . These peaks are marked in Figure 4.2. With this combination of peaks, spectral classification was 87.9% accurate.

4.4 Conclusions

This is the first study using Raman spectroscopy to distinguish between neuroblastoma, Ewing sarcoma, non-Hodgkin lymphoma, and rhabdomyosarcoma, a class of cancers known as small round blue cell tumors.

Each of the small round blue cell tumors has a low incidence. Each year in the United States, there are about 387 neuroblastoma cases (other sources suggest the number may be slightly higher: 400-650 annual cases ("What Are the Key Statistics About Neuroblastoma?," 2009; Young Jr, J. L. et al., 1986)), 112 Ewing sarcoma cases, 191 rhabdomyosarcoma cases, and 386 non-Hodgkin lymphoma cases (Young Jr, J. L. et al., 1986), totaling less than 1100 diagnoses of the four most common small round blue cell tumors. In contrast, there are more than 214,000 new cases of breast cancer and 234,000 new cases of prostate cancer diagnosed annually in the United States ("Cancer Facts & Figures 2006," 2006). Even though the small round blue cell tumors only represent a fraction of the total number of annual cancer diagnoses, their similar histologies make them a major diagnostic problem.

Current clinical diagnostic methods to identify small round blue cell tumors in addition to traditional hematoxylin-eosin staining with light microscopy include immunohistochemistry, fluorescence in-situ hybridization, electron microscopy, and karyotyping. To get a definitive diagnosis might take several days. The current state-of-the-art test is being developed by Chen et al using polymerase chain reaction and

artificial neural networks to find unique genetic profiles for each type of small round blue cell tumors. The drawback to this test, however, is that it still has a 48-hour turnaround time. An existing, traditional Raman spectroscopy system stationed in a pathology laboratory could provide a diagnosis within hours of tumor resection. Classification time could be further reduced by introduction of a portable Raman spectroscopy surgical tool directly into the operating room. In that case, a surgeon could theoretically obtain a diagnosis even before the tumor is removed.

Discriminant function analysis showed that only 10-18 peaks were necessary to accurately classify the small round blue cell tumors. At the tissue level, small combinations of peaks classify data as well as the full range of peaks. Spectral-level classification actually improved when only peaks which were diagnostically significant were used. Identifying peaks which are diagnostically significant allows a simpler measurement and classification method than using the whole range of wavenumbers.

While the process of peak selection is time consuming, it allows much greater understanding of the Raman spectra. In the future, the selection process might be automated to reduce the time necessary for peak selection. The automation process could also address other questions regarding this technique, including whether the order of peak removal matters. In the data described here, peaks were removed from the analysis based on the standardized canonical discriminant functions, then based on the proximity of other diagnostic peaks, or on the magnitude of the wavenumber with lower wavenumbers selected for removal first. It is unknown whether the results of peak selection (including which peaks are selected as diagnostically significant, and the overall classification results) would change if peaks were removed from low-

wavenumber to high-wavenumber, vice-versa, or through another technique such as attempting to remove peaks in order of lowest standardized canonical discriminant function.

Peak-wise analysis was not performed on data prior to this point because the computing and software capability were not available. A new software release of SPSS combined with a better processing system allowed in-depth data analysis and peak selection, rather than an overall analysis which provided little information regarding underlying biochemical significance. In the future, other data included in this research can be reviewed and processed using similar techniques to improve classification results and draw conclusions about the biological significance of the diagnostic peaks.

Using select peaks also allows derivation of biochemically significant information from the data. Peaks which are diagnostically different correlate to varying concentrations of specific chemical bonds and biochemicals. As an example, tryptophan had the highest concentration in Ewing sarcoma, according to the peak intensities at 753.7, and 1230.5, cm^{-1} . An experienced cancer biologist might then be able to correlate this finding with the biology of Ewing sarcoma. One possible explanation is that tryptophan is over-expressed in Ewing sarcoma because it is key component in the CD99 protein and the EWS/FLI-1 gene. This hypothesis could only be proven with careful testing and review by an experienced cancer biologist, however.

Neuroblastoma had the sample size of each tumor group. As the number of specimen examined increases for neuroblastoma and for the other small round blue cell tumors, more variability will be introduced into the database. This will have several implications.

First, peaks which were originally thought to be diagnostically significant may not actually be significant. As the mean and standard deviation are adjusted to truly represent the total population for a given tumor, some peaks will become less significant while others become more significant. This means the data and classification models need to be adjusted over time to accommodate the fluid model.

Another implication is a broader range of tumors will be identifiable over time. As the significant peaks are fine-tuned, and more tumors are added to the database, classification ability should become more sensitive and specific over time.

Some of the Raman 'peaks' which were mathematically selected in data analysis actually correlated to valleys on the Raman spectra. This signifies the lack of a chemical or a region between two chemicals, or it may represent a horizontal peak shift. 793.5 cm^{-1} was a strong valley for Ewing sarcoma, and 1571.5 and 1630 cm^{-1} were valleys for both neuroblastoma and Ewing sarcoma. Another feature which was identified through mathematical peak selection was a shoulder at 1275 cm^{-1} . Re-measuring samples with a higher-resolution optical system might point to a combination of individual peaks which amounted to a shoulder using our existing optical system. Examination of these spectral features by an experienced biochemist or biologist may provide further insight towards the cause of these features.

CHAPTER 5 CLASSIFICATION OF UNFAVORABLE, FAVORABLE, AND TREATED NEUROBLASTOMAS

5.1 Introduction

Treatment and prognosis of neuroblastoma are based on several factors. The stage of the disease describes whether the tumor has metastasized, or spread to other locations. Histology markers are used to determine the Shimada favorability of the tumor. This allows doctors to identify the tumor's aggressiveness. Finally, the advent of genetic testing allows physicians to identify several genetic factors associated with a good or poor prognosis (Cohn, S. L. et al., 2009). Several different stratification methodologies exist for determining neuroblastoma prognosis. In general, the methodologies used depend on the geographic location of the hospital (North America, Europe, Asia, and Australia each have slightly different methodologies) and the pathologists' personal preference.

5.1.1 Shimada Classification Based on Histology Findings

In 1999, Shimada proposed a method for determining the favorability of neuroblastoma as favorable or unfavorable (Shimada, H. et al., 1999a). It considers the patient's age, development of stroma, grade of differentiation, and Mitosis Karyorrhexis Index (MKI). MKI is defined as the number of cells experiencing mitosis (process of separation of two sets of chromosomes in a splitting cell) or karyorrhexis (fragmentation of nucleus in the dying cell; measurable by the irregular distribution of chromatin in the cell) in a count of 5,000 total cells (Shimada, H. et al., 1999b). The pathologist must sample between six and twenty areas on the sample to count a total of 5,000 cells. Low MKI is defined as less than two percent of cells in mitosis or karyorrhexis, intermediate

is defined as two to four percent of cells, and high is defined as four percent of cells or more in mitosis or karyorrhexis.

Stromal cells are connective tissue cells. In stroma-poor neuroblastomas, there is little separation between neuroblast cells, and the stromal cells are poorly developed. In stroma-rich and stroma-dominant neuroblastoma, there are more stromal cells which are more developed (Shimada, H. et al., 1999b).

In differentiating neuroblastomas, at least 5% of cells are matured to ganglion cells. Poorly differentiating neuroblastomas have less than 5% of cells matured to ganglion cells. Ganglioneuroblastoma subtype exhibits a mix of neuroblastoma-like tumor and ganglioneuroma-like tumor (mature stromal cells with scattered mature ganglion cells). The undifferentiated subtype has small, unidentifiable undifferentiated cells. Generally, pathologic methods other than histology (such as electron microscopy, genetic testing) are required to identify undifferentiated tumors (Shimada, H. et al., 1999b).

This system became a standard because it strongly correlated with event free survival rates, and there is typically high rate of consensus among pathologists. Agreement can vary, however, based on the region of the tissue which is tested. Some areas display different characteristics than others. Table 5.1 shows the decision processing for diagnosing neuroblastoma as favorable or unfavorable, as well as ganglioneuroblastoma.

Prognosis	Age	Differentiation	MKI	Stroma
Favorable	<18 months	poorly differentiated	low	-
	<18 months	poorly differentiated	intermediate	-
	18 mo - 5 yr	differentiating	low	-
		ganglioneuroblastoma		rich
Unfavorable	<18 months	undifferentiated	-	-
	<18 months	-	high	-
	18 mo - 5 yr	undifferentiated	-	-
	18 mo - 5 yr	poorly differentiated	-	-
	18 mo - 5 yr	-	intermediate	-
	18 mo - 5 yr	-	high	-
	> 5 years	-	-	-
	-	ganglioneuroblastoma	-	composite

Table 5.1: Definition of the Shimada system of classifying favorable and unfavorable neuroblastoma, ganglioneuroblastoma, and ganglioneuroma. (adapted from (Shimada, H. et al., 1999a))

5.1.2 International Neuroblastoma Staging System

In 1988, the International Neuroblastoma Staging System was established for staging neuroblastoma and the International Neuroblastoma Response Criteria was established to track response to treatment (Brodeur, G. et al., 1988). This was revised in 1993 (Brodeur, G. et al., 1993). Howman-Giles *et al.* summarized the stages as follows:

Stage 1: Localized tumor without regional lymph node involvement.

Stage 2: Unilateral tumor with either incomplete gross resection or ipsilateral nodal involvement.

Stage 3: Tumor that crosses the midline or has contralateral nodal involvement.

Stage 4: Tumor disseminated to distant lymph nodes, bone, bone marrow, liver, etc.

Stage 4S: Special category: age <1 year, localized primary tumor, dissemination only to liver, skin, or bone marrow.”

5.1.3 Other Prognostic Factors

While the two previous methodologies, Shimada classification and International Neuroblastoma Staging System, are widely accepted for neuroblastoma diagnosis, several other markers exist which are associated with a good or poor prognosis. Prognostic markers cover a variety of information, from age to tumor markers (VMA, HVA, dopamine, ferritin levels, etc.) to histology (degree of differentiation, MKI, presence of stroma, etc) and genetics (growth fraction, N-myc copy number, presence or absence of oncogenes and tumor suppressor genes, etc) (Brodeur, G. et al., 1993). Several other key markers are described below:

Age: While age is included in the Shimada classification, it stands alone as a significant prognostic marker. Children who are diagnosed younger than 18 months are likely to have a good outcome ("How is Neuroblastoma Staged?," 2009). However the exception to this rule is that children diagnosed with stage 4S disease at less than 4 weeks old tend to have higher mortality rates due to complications from disease (van Noesel, M. et al., 1997).

Ploidy: Ploidy is the number of sets of chromosomes in a cell. Normal human cells are diploid, meaning they have two pairs of chromosomes. Cells expressing more sets of chromosomes are called hyperdiploid. For very young children, hyperdiploidy is associated with better outcomes ("How is Neuroblastoma Staged?," 2009).

MYCN Amplification: MYCN is a proto-oncogene. It normally prevents cells from multiplying too quickly, and it is normally expressed within a cell. When the level of MYCN is amplified, however, it turns into an oncogene, meaning it makes the cell

cancerous. MYCN over expression is associated with a poor prognosis ("How is Neuroblastoma Staged?," 2009).

Nerve growth factor (neurotrophin) receptors: Neurotrophin receptors are located on the surface of normal neural cells. They receive extracellular signals which induce the cell to mature. The presence of neurotrophins such as TrkA are associated with a favorable prognosis ("How is Neuroblastoma Staged?," 2009).

Serum Markers: Neuroblastoma cells may release chemicals such as ferritin, neuron-specific enolase, or lactate dehydrogenase into the blood, which are all associated with a poor prognosis ("How is Neuroblastoma Staged?," 2009). These can all be tested with blood serum tests. Another substance, ganglioside GD2 may be overabundant in neuroblastoma as well, but it's correlation to prognosis is not known ("How is Neuroblastoma Staged?," 2009).

5.1.4 International Neuroblastoma Risk Group Classification System

The stage of the neuroblastoma is based solely on the patient age, the tumor's location and the spread of disease, while the Shimada classification is based strictly on the tumor histology and patient age. Meanwhile, a variety of other markers also exist for predicting patient prognosis as described above, including VMA, HVA, dopamine, and ferritin levels, growth fraction, MYCN copy number and other genetic factors, and age. All of this information combined gives a more accurate prediction about the patient's prognosis and the best form of treatment. Based on these prognostic factors, patients are placed into low, intermediate, or high risk groups. In general, the 5-year survival rates for these groups are 90-95%, 85-90%, and ~30%, respectively ("How is Neuroblastoma Staged?," 2009).

From 2004 to 2006, researchers from all of the international neuroblastoma research groups met to establish a neuroblastoma prognostic and aggressiveness classification methodology based on statistical analysis of previous neuroblastoma prognostic factor, treatment, and outcome data in patients from 1990 through 2002 (Cohn, S. L. et al., 2009). Information was collected on 35 potential prognostic identifiers from 8,800 patients. The significance of prognostic identifiers was judged based on event free survival (EFS) rates. Because age was included as a factor, Shimada classification was split into tumor differentiation, MKI, and histology category.

Factors which were found to be significant included stage of disease (INSS), patient age, histology category (neuroblastoma, ganglioneuroblastoma intermixed differentiated, or nodular), tumor differentiation, MYCN amplification, chromosome 11q abnormality, and ploidy (Cohn, S. L. et al., 2009). From these seven factors, a decision tree was created for separating the different prognostic groups. A total of sixteen different groups were created for pre-treatment classification. The sixteen groups were further split into four risk groups: very low ($>85\%$ EFS), low ($>75\% - \leq 85\%$ EFS), intermediate ($\geq 50\% - \leq 75\%$ EFS), and high ($<50\%$ EFS).

It was suggested that treatment protocols should be customized for each of the sixteen groups. Generally, low risk patients are treated with surgery or no treatment, intermediate risk patients are treated with a moderate chemotherapy, and high risk patients are treated with aggressive chemotherapy and sometimes bone marrow transplants (Shimada, H. et al., 1999a). The new 16-group prognostic model, however, may change the recommended protocol for some patient groups.

5.1.5 Effects of Treatment

There are many variations in the effect of treatment on neuroblastoma. If an ineffective method of treatment is used, there may be no effect on the tumor. Other changes include tissue necrosis, hemorrhage, calcification of the tissue, or maturation of the tumor. When neuroblastomas mature, the neuroblast cells differentiate to ganglionic cells and the neurofibrillary stroma differentiate into collagenous Schwannian-type stroma. The combination of these changes makes matured, treated neuroblastomas have histologies similar to ganglioneuroma or ganglioneuroblastoma.

5.1.6 Previous Work in Identifying Specific Tumor Features

While certain treatments can cause necrosis to a tumor and the surrounding tissue, the presence of a tumor, even untreated, can also cause necrosis. A study of untreated glioblastoma tumors showed that it was possible to identify between tumor tissue and necrotic tissue with Raman spectroscopy using discriminant function analysis (Koljenovic, S. et al., 2002). Peak analysis showed a higher contribution of cholesterol in necrotic tissue regions.

Several studies have examined varying levels of dysplasia in different tissues, including cervix (Robichaux-Viehoever, A. et al., 2007), esophagus (Shetty, G. et al., 2006a), epithelial tissues (Stone, N. et al., 2002), the larynx (Stone, N. et al., 2000), and the bladder (Crow, P. et al., 2004). Dysplasia represents a shift from normal tissue towards cancer. It is often classified as high-grade or low-grade, or according to the types of cells present. While this varies slightly from cancer grading, it represents a similar classification methodology based on the underlying biochemistry of the abnormal tissue.

One Raman spectroscopy study was able to differentiate between three stages of bladder cancer, as well as identify them from other benign conditions and normal bladder tissue. Also of note in this study, authors were able to predict the stage of the disease (how far it penetrated into other areas) based on the biochemical composition of the primary tumor site (Crow, P. et al., 2004).

Prostate cancer represents another type of cancer where the designated aggressiveness of the disease (Gleason score) can vary between pathologists. A study was performed which examined the three grades of prostate cancer (Gleason score less than 7, equal to 7, or more than 7) and benign prostatic hyperplasia using Raman spectroscopy. Samples were only included if the two blinded pathologists studying the tissues came to the same Gleason score independently. Analysis of the four tissue groups showed high sensitivity (81-94%) and specificity (92-100%) in identifying each grade of tumor and the benign condition (Crow, P. et al., 2003b).

Rather than testing whole tissues, cell lines are sometimes used for Raman measurement. This allows evaluation of only cancer cells, rather than inclusion of other extra-cellular components and other cell types. One study was performed which looked at two aggressive prostate cancer cell lines (androgen insensitive, poorly differentiated) and two non-aggressive prostate cancer cell lines (androgen sensitive, well differentiated). A combination of principal component analysis and discriminant function analysis was able to differentiate between the aggressive and non-aggressive cell lines. Furthermore, it could distinguish each cell line from the other three cell lines tested (Crow, P. et al., 2005a).

A similar study was performed to identify cells transformed to have an extended cell cycle and lifespan and cells exposed to asbestos for immortalization from normal bronchial epithelial cells. Discriminant function analysis was able to identify the three groups of cells with 75-87% sensitivity and 85-96% specificity (Jess, P. et al., 2009).

Other attempts to measure specific grades of tumors, including breast (Clare, S. E. et al., 2006) and thyroid cancer (Teixeira, C. et al., 2009) have been unsuccessful to date, with many studies concluding that a larger dataset of tumors of each grade would increase classification ability.

5.1.7 Research Plan

The goal of this chapter is to identify neuroblastomas as either favorable histology or unfavorable histology as designated by the Shimada classification, or to identify a neuroblastoma tumor as treated. Raman spectroscopy should allow for easy and accurate evaluation of tumor histology, since it provides a biochemical fingerprint of the measurement area.

5.2 Materials and Methods

5.2.1 Data Collection

The Raman spectra of neuroblastoma from Chapters 2 and 3 were used for this study. At the time of pathology review, the pathologists assigned a favorable or unfavorable diagnosis to the untreated neuroblastomas according to the Shimada classification. Neuroblastomas which received treatment were all assigned to a single group, regardless of the Shimada classification pre-treatment, or the histological effects of the treatment. Following data analysis, slides were re-reviewed by pathologists when

there was a discrepancy between the Raman classification and the pathology classification.

5.2.2 Data Processing

Data was processed using the same methodology as described in section 1.2.4 and Appendix B.

5.3 Results

5.3.1 Preliminary Fresh Tissue Analysis

The initial data set consisted of 106 spectra from 6 unfavorable neuroblastomas, 114 spectra from 5 favorable neuroblastomas, and 82 spectra from 5 treated neuroblastomas, as shown in Table 5.2. Tissue favorability was determined by an experienced pediatric pathologist based on the Shimada classification.

Histology	Number of Tissues	Number of Spectra
Unfavorable Neuroblastoma	6	106
Favorable Neuroblastoma	5	114
Treated Neuroblastoma	5	82

Table 5.2: Number of unfavorable, favorable, and treated neuroblastomas in preliminary fresh tissue analysis.

Favorable and unfavorable tumors were classified with 95.3% sensitivity and 93.8% specificity, as shown in Table 5.3. Seven of 114 favorable spectra were misclassified, and five of 106 unfavorable spectra were misclassified. Using the majority of individual spectra within a tissue to diagnose the whole tissue, favorable and unfavorable tumors were distinguished with 100% sensitivity and specificity.

Classification Results^a

Subgroup		Predicted Group Membership		Total	
		Unfavorable	Favorable		
Original	Count	Unfavorable	101	5	106
		Favorable	7	107	114
	%	Unfavorable	95.3	4.7	100.0
		Favorable	6.1	93.9	100.0

a. 94.5% of original grouped cases correctly classified.

Table 5.3: Classification of favorable and unfavorable neuroblastoma

Figure 5.1 shows the mean spectrum for the preliminary favorable versus unfavorable neuroblastoma study. Based on visual inspection of the mean spectrum, favorable histology tumors had higher protein levels based on the elevated peaks at 1447, 1555, and 1660 cm^{-1} and the shoulder at 1264 cm^{-1} . Favorable tumors also seemed to exhibit increased amino acid peaks at 754, 938, 1004, 1034, 1210, and 1620 cm^{-1} . These peaks are marked for visual clarity.

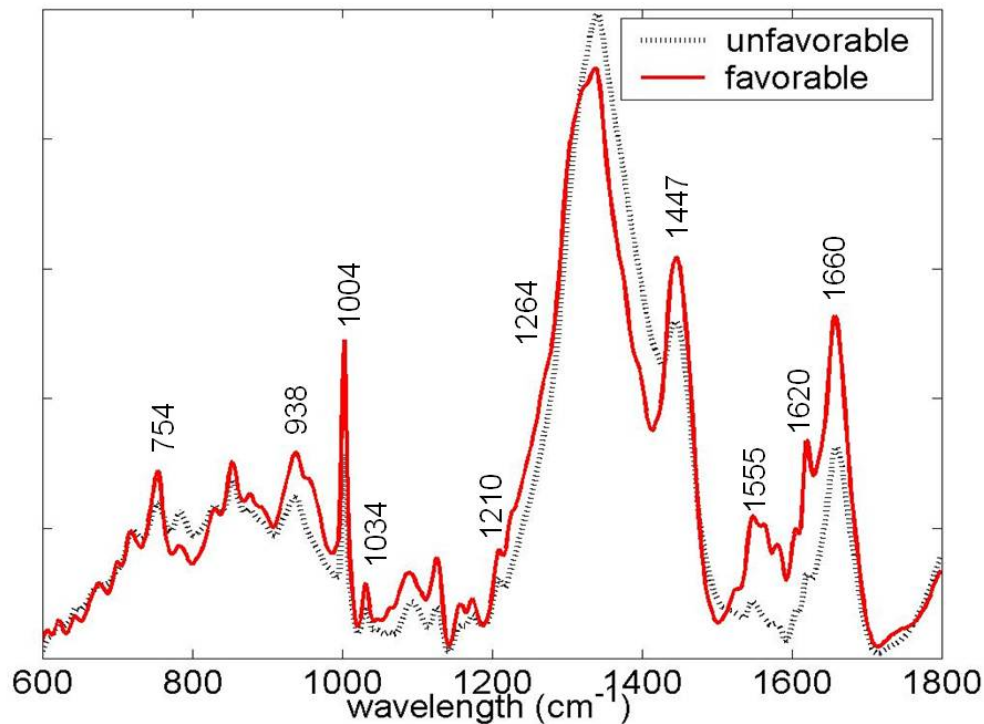


Figure 5.1: Mean spectra of favorable and unfavorable neuroblastoma

When classifying between treated and untreated neuroblastoma, favorable and unfavorable neuroblastoma were combined into a single untreated group. At the spectral level, treated and untreated tumors were separated with 93.2% sensitivity and 70.7% specificity as shown in Table 5.4. At the tissue level, all eleven untreated neuroblastoma were correctly identified, while three of the five treated neuroblastoma were correctly identified.

Classification Results^a

Treated			Predicted Group Membership		Total
			Untreated	Treated	
Original	Count	Untreated	205	15	220
		Treated	24	58	82
	%	Untreated	93.2	6.8	100.0
		Treated	29.3	70.7	100.0

a. 87.1% of original grouped cases correctly classified.

Table 5.4: Classification results comparing untreated and treated neuroblastoma

One of the effects of treatment may be maturation from neuroblastoma to ganglioneuroma. When treated neuroblastoma was compared with ganglioneuroma, they were differentiated with 90.2% sensitivity and 97.4% specificity, as shown in Table 5.5. Using the majority spectra rule, all ganglioneuroma spectra were correctly identified and four out of five treated neuroblastoma tissues were correctly identified.

Classification Results^a

Subgroup			Predicted Group Membership		Total
			Ganglioneurom a	Treated	
Original	Count	Ganglioneuroma	184	5	189
		Treated	8	74	82
	%	Ganglioneuroma	97.4	2.6	100.0
		Treated	9.8	90.2	100.0

a. 95.2% of original grouped cases correctly classified.

Table 5.5: Classification of ganglioneuroma and treated neuroblastoma

Finally, a combined data set of untreated neuroblastoma, treated neuroblastoma, and ganglioneuroma were compared. Figure 5.2 shows the discriminant function analysis plot for this classification, and the mean spectrum for each type of tissue. Note that there seems to be a clear progression from untreated tumor towards ganglioneuroma as treatment is applied. Classification results are shown in Table 5.6.

Subgroup		Predicted Group Membership			Total	
		Unfavorable	Favorable	Treated		
Original	Count	Unfavorable	92	11	3	106
		Favorable	5	99	10	114
		Treated	13	16	53	82
	%	Unfavorable	86.8	10.4	2.8	100.0
		Favorable	4.4	86.8	8.8	100.0
		Treated	15.9	19.5	64.6	100.0

a. 80.8% of original grouped cases correctly classified.

Table 5.6: Classification of unfavorable, favorable, and treated neuroblastoma

Visual inspection of the mean spectra peaks showed that treated neuroblastomas displayed a strong shoulder near 1240 cm^{-1} differentiating it from untreated neuroblastoma and ganglioneuroma. This might correlate to higher concentrations of collagenous stroma in treated neuroblastoma. Treated neuroblastoma also appeared to differ from ganglioneuroma in the region $1516\text{-}1622\text{ cm}^{-1}$. This is a region rich in protein and amino acids (Socrates, G., 2001).

Finally, a case study of three tumors from one patient was performed. One sample was available from the time of diagnosis, one sample was available following tumor treatment, and one sample was resected from an extradural brain metastasis one year following diagnosis. Figure 5.3 shows representative histology images from each tissue sample and the results of discriminant function analysis.

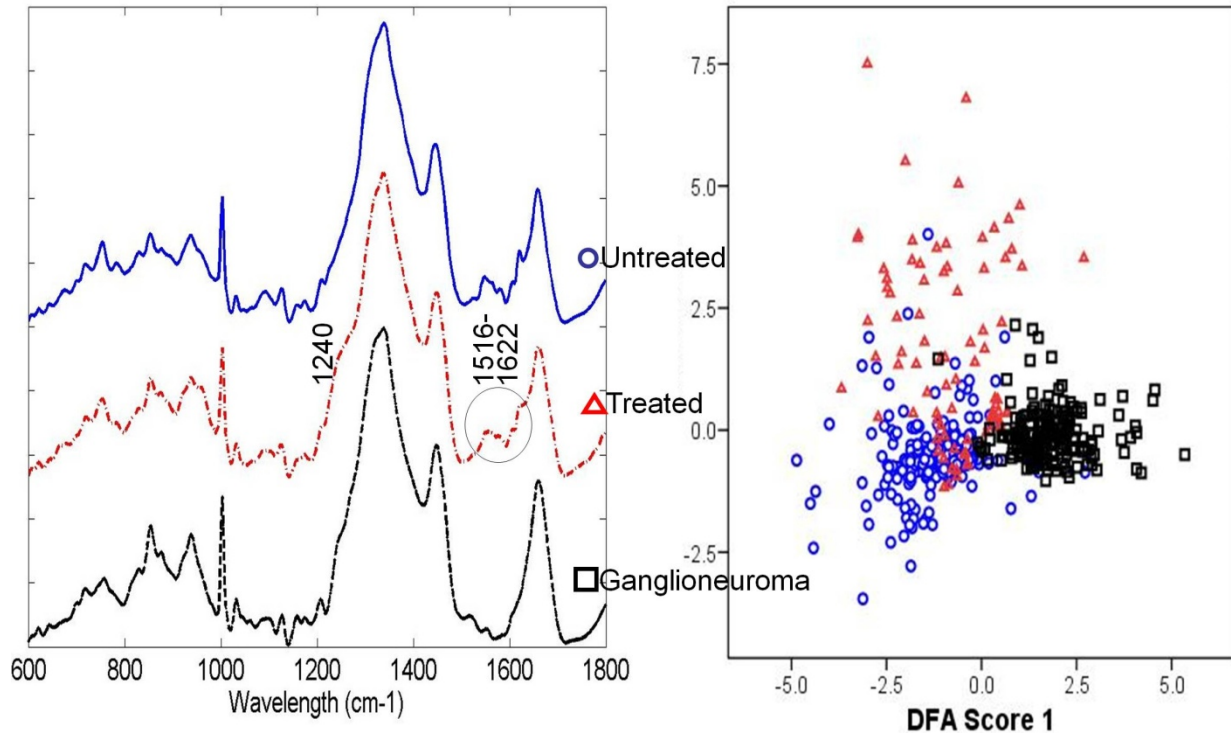


Figure 5.2: The mean spectra of untreated neuroblastoma, treated neuroblastoma, and ganglioneuroma with discriminant function analysis results shown.

Discriminant function analysis separated the diagnosis and treated sample with 100% sensitivity and specificity. This is consistent with the maturation shown in the histology images. The metastatic sample had two spectra which were diagnosed as the original tumor at the time of diagnosis. On examination of the tumor histology, the metastatic tumor sample showed a mixture of ganglionic maturing cells and immature neuroblasts, which were prevalent in the original sample. This likely explains the overlap between the two samples.

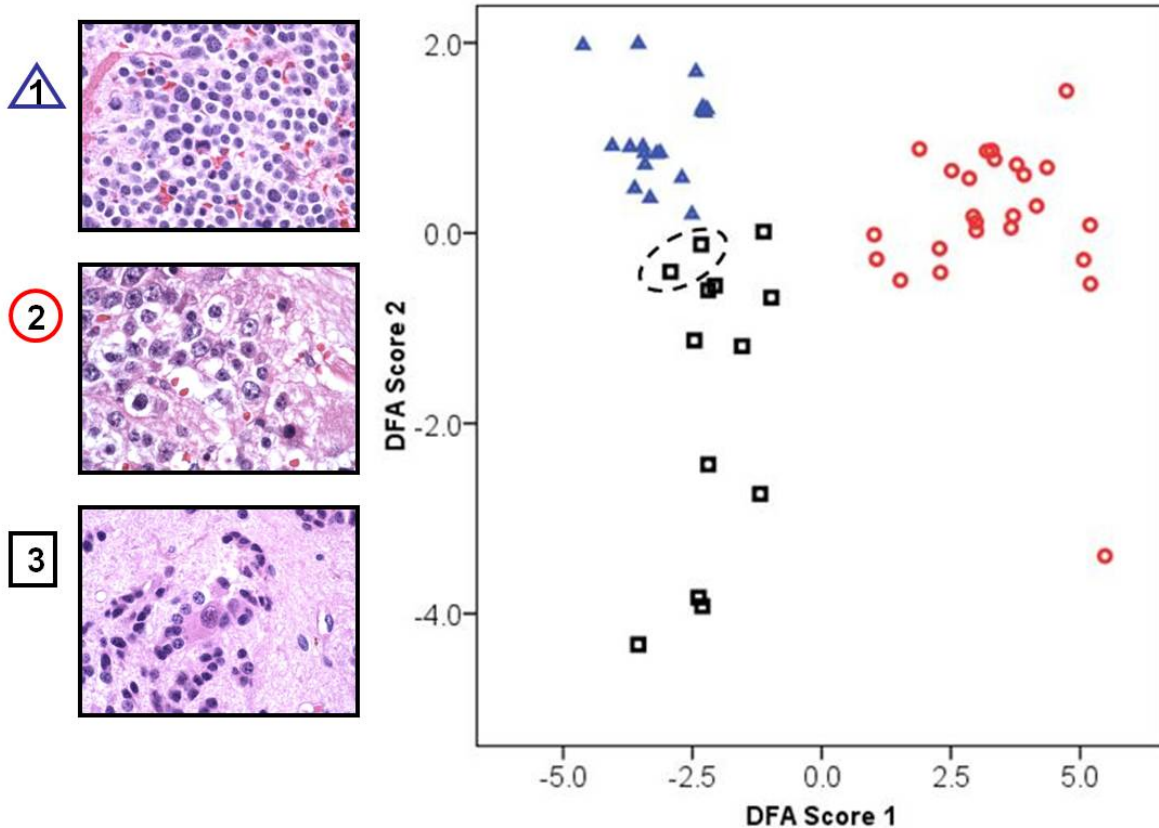


Figure 5.3: Discriminant function analysis and histology images of three tumors from one patient.

Once again, visual inspection of the Raman spectra for each sample showed that the treated sample had higher peaks at 719, 1000, 1031, 1093, 1152, 1444, 1547, 1578, 1604, 1621, and 1659 cm^{-1} , in addition to the characteristic shoulder around 1240 cm^{-1} . Again, these peaks may all be associated with various protein components. Also of note, there was a strong peak at 960 cm^{-1} in the Raman spectra of the metastatic sample. The biochemical origin of that peak could not be determined.

5.3.2 Preliminary Fresh and Frozen Tissue Analysis

Analysis of the original fresh neuroblastoma tissues showed promising results for distinguishing unfavorable, favorable, and treated neuroblastoma, and in distinguishing treated neuroblastoma from ganglioneuroma. Following this early analysis, frozen

tumors were included in the study to determine if they offered the same classification potential. Table 5.7 shows the number of fresh and frozen tissues and spectra available for the preliminary fresh and frozen analysis.

	Fresh		Frozen	
	Tissues	Spectra	Tissues	Spectra
Untreated	16	257	5	63
Favorable	8	130	4	47
Unfavorable	8	127	1	16
Treated	9	159	6	78
Ganglioneuroma	14	206	2	22

Table 5.7: Data collected for fresh versus frozen study

The mean spectra of fresh and frozen favorable, unfavorable, and treated neuroblastoma are shown in Figure 5.4. For each tissue type, the mean fresh and frozen spectra are extremely similar.

When frozen treated and untreated neuroblastoma were classified using the fresh tissue model, 10 of 78 untreated neuroblastoma spectra and 12 of 63 treated neuroblastoma spectra were misclassified (Table 5.8). As mentioned in Chapter 3, however, some of the frozen, treated neuroblastomas had nests of immature neuroblast cells although the majority of the tissue was composed of mature cells. Misclassifications of treated spectra may actually represent identification of immature cells within a sample which otherwise displays characteristics of a treated neuroblastoma.

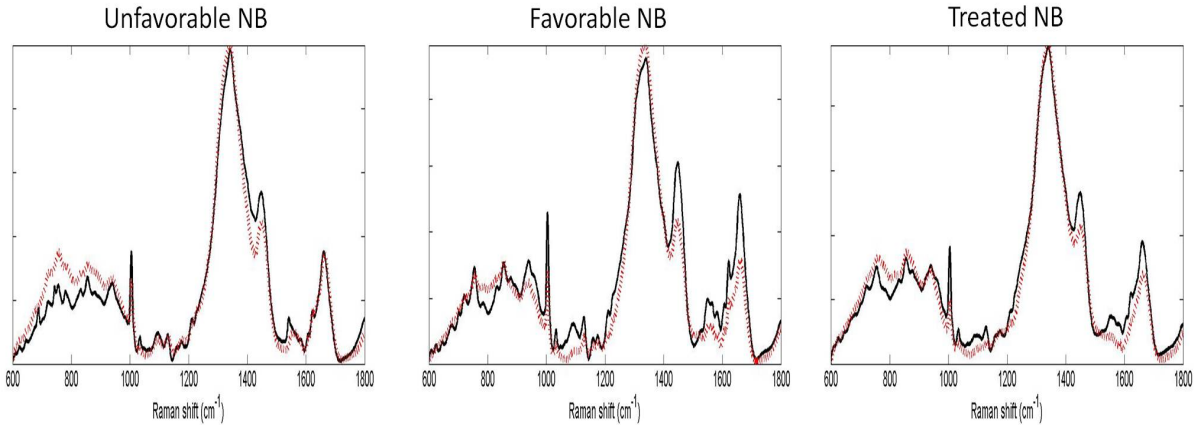


Figure 5.4: fresh (solid black line) and frozen (dashed red line) mean spectra of unfavorable, favorable, and treated neuroblastoma

Classification Results^{a,b}

				Treated		Predicted Group Membership		Total
				untreated	treated	untreated	treated	
Cases Selected	Original	Count	untreated	231	26	257		
			treated	43	116	159		
	%	untreated	89.9	10.1	100.0			
		treated	27.0	73.0	100.0			
Cases Not Selected	Original	Count	untreated	51	12	63		
			treated	10	68	78		
	%	untreated	81.0	19.0	100.0			
		treated	12.8	87.2	100.0			

a. 83.4% of selected original grouped cases correctly classified.

b. 84.4% of unselected original grouped cases correctly classified.

Table 5.8: Classification of treated and untreated frozen neuroblastoma (“cases not selected” row) based on classification model of fresh neuroblastoma (“cases selected” row)

Neuroblastoma morphology shifts to look more similar to ganglioneuroma when it is treated. When frozen treated neuroblastoma and ganglioneuroma spectra were compared based on the model of fresh tissues, ganglioneuroma was identified 100% of the time, and only 4 of 78 treated neuroblastoma spectra were misclassified, as shown in Table 5.9.

Classification Results^{a,b}

				Subgroup		Predicted Group Membership		Total
				Gn	tNB	Gn	tNB	
Cases Selected	Original	Count	Gn	196	10	206		
			tNB	24	135	159		
		%	Gn	95.1	4.9	100.0		
			tNB	15.1	84.9	100.0		
Cases Not Selected	Original	Count	Gn	22	0	22		
			tNB	4	74	78		
		%	Gn	100.0	.0	100.0		
			tNB	5.1	94.9	100.0		

a. 90.7% of selected original grouped cases correctly classified.

b. 96.0% of unselected original grouped cases correctly classified.

Table 5.9: Classification of treated and ganglioneuroma frozen spectra (“cases not selected” row) based on classification model of fresh spectra (“cases selected row)

Fresh tissues were not classified based on the frozen model because of the small size of the frozen data set.

5.4 Conclusions

This is the first study using Raman spectroscopy to identify histologic features of neuroblastoma tumors. Untreated tumors were classified according to the gold standard Shimada classification, as assigned by experienced pediatric pathologists. Favorable and unfavorable were distinguished with 100% sensitivity and specificity at the tissue level.

Unfavorable and favorable tumors were also combined into an untreated group and compared to treated tumors. Effects of treatment can include maturation and necrosis. When compared with untreated neuroblastoma and with untreated ganglioneuroma, untreated tumors were always differentiated from treated with 100% sensitivity at the tissue level. Some treated tumors, however, were still misclassified as untreated. This could be due to specific histologic features within the misclassified cases.

By visual examination, treated neuroblastomas exhibited a shoulder at 1240 cm^{-1} and an increased signature in the range of $1516\text{-}1622\text{ cm}^{-1}$. These may be due to increased protein and amino acid levels. Consultation with an experienced biologist or biochemist may provide a more complete understanding of the underlying biochemical changes from tissue to tissue.

Finally, frozen tissues were examined to gauge their similarity to the fresh tissues. Very few frozen tissues were available, so it was not possible to build a frozen model and then test it on fresh tissues. When the frozen tissue spectra which were available were tested based on the fresh model, there was high sensitivity in judging between untreated and treated neuroblastoma and between treated neuroblastoma and ganglioneuroma. In the future, more frozen tissues will be tested, and a more in-depth comparison between fresh and frozen unfavorable, favorable, and treated neuroblastoma will be performed.

This research opens a new door for both clinical and basic science cancer research using Raman spectroscopy. Previous research used Raman spectroscopy to distinguish between normal tissue and cancerous tissue, or between two types of cancerous tissue, however, it did not identify specific subtypes or prognostic groups within a cancer.

Rapid identification of aggressive and non-aggressive cancers through an objective methodology offers a great clinical advance. Although classification methodologies such as the Shimada classification offer a somewhat objective approach with fixed parameters for each grouping, results can still vary based on the area of tissue sampled or the pathologist's count of the specific features of the tumor. Raman

spectroscopy can reduce the subjectiveness of this identification by measuring the specific biochemical constituents. It can even reduce the error introduced by sampling different areas of the tissue if a scan is performed over several regions of the tissue.

Raman spectroscopy also has potential to identify the effects of treatment on neuroblastoma. Once a larger database is developed, it may have the sensitivity to identify exact changes due to drug treatment, including maturation or necrosis. At a basic science level, this may allow researchers to better understand the effects of treatments on tumors of a known histology through analysis of the Raman spectra. Furthermore, periodic monitoring of patients throughout treatment can also be used to identify a tumor's response to treatment. This could allow clinicians to quickly evaluate the effects of a new treatment to determine if it is the optimal treatment or if another treatment should be used.

CHAPTER 6 BLINDED STUDY WITH CHILDREN'S ONCOLOGY GROUP TO IDENTIFY FAVORABLE, UNFAVORABLE, AND TREATED NEUROBLASTOMA

6.1 Introduction

In order to prove the diagnostic capability of Raman spectroscopy, it must be used in a truly blinded study, and then in prospective, blinded studies. This chapter represents the first step towards proving diagnostic clinical capability in a blinded study performed in conjunction with the Children's Oncology Group, a national tumor bank.

Prior to this study, all human clinical studies were performed using the same Leica 20x objective. This objective was damaged immediately before receiving the shipment of samples from the Children's Oncology Group, and the new samples had to be measured with new lenses. This introduced an additional layer of variability into the data. In addition to describing the blinded study, this chapter also outlines the methods we used in an attempt to join our original data set with a blinded data set measured with another lens.

6.2 Materials and Methods

6.2.1 *Sample Procurement*

In order to perform a truly blinded study, the Children's Oncology Group agreed to share eight samples each of favorable, unfavorable, and treated neuroblastoma. All 24 samples could not be obtained because they do not allow depletion of any single tumor within their collection. However, they did share 22 samples. It is not known which diagnostic group the two unshared samples came from.

6.2.2 Sample Measurement

This experiment consisted of a training set of data which was used to build a diagnostic model, and a testing set of data, which the model was tested on. The training data consisted of all fresh and frozen specimens previously collected and described. The testing data consisted of the Raman spectra of the samples provided by the Children's Oncology Group.

Samples were individually wrapped in foil and placed in tissue cassettes by COG employees, then shipped overnight on dry ice. Upon arrival, samples were placed in a -80°C freezer until measurement time.

When samples were ready for measurement, they were removed from their wrapping and placed in an eppendorf tube or cryovial which was then filled with room temperature saline. Samples were allowed to defrost for 30 minutes, and then they were removed from the vial and placed on a glass microscope slide. Following measurement, samples were replaced in their foil wrapping and tissue cassette and placed in the -80°C freezer for storage.

As mentioned in the introduction, the microscope objective which was originally used for measurement was damaged prior to receiving the Children's Oncology Group samples. All samples were originally measured with a replacement 20x Nikon Plan-Flour microscope objective and replaced in the freezer. On data analysis, however, this data was incompatible with the previous data set collected with a Leica-brand lens (see results). After it was determined that data from the Nikon lens was incompatible, all samples were re-tested with a Leica 20x objective identical to the original objective.

6.2.3 Data Processing

Data was preprocessed as previously described. For classification, the original intent was to perform Principal Component Analysis on the training data and apply the results to the testing data, then perform discriminant function analysis on the training data and apply those results to the training data. Because of the spectral differences from objective to objective, however, this method was not feasible. The results section provides an in-depth description of the methods used throughout data analysis and the justification for each step of the analysis.

The end result of the analysis was three methods of discriminant function analysis. Because the study was blinded, there was no way to know which method was best without first consulting with the Children's Oncology Group.

A separate analysis was performed for treated vs untreated and for favorable vs unfavorable. Because treated neuroblastoma can cover a broad range of histologies, all treated neuroblastomas were excluded from the training data set when analyzing tumor favorability. That is why tumors marked as 'treated' also have a favorable or unfavorable diagnosis.

6.3 Results

6.3.1 Nikon Lens Results

Figure 6.1 shows the mean spectrum of processed data from the favorable histology training group, the unfavorable histology training group, the treated histology training group, and the Nikon lens testing group, which was composed of the samples sent from the Children's Oncology Group. Visual examination shows a clear difference between the original training data and the new data measured with the Nikon lens.

Clearly, there is a difference in the underlying background signal measured between the two lenses, as exhibited by the varying signal intensities. It is important to note, however, that most of the key peaks still align, just at different intensities. The two types of lenses used allow varying amounts of light into the objective, which may cause the differences in the underlying backgrounds. It may be possible to better align the peak intensities through software processing of the Raman spectra.

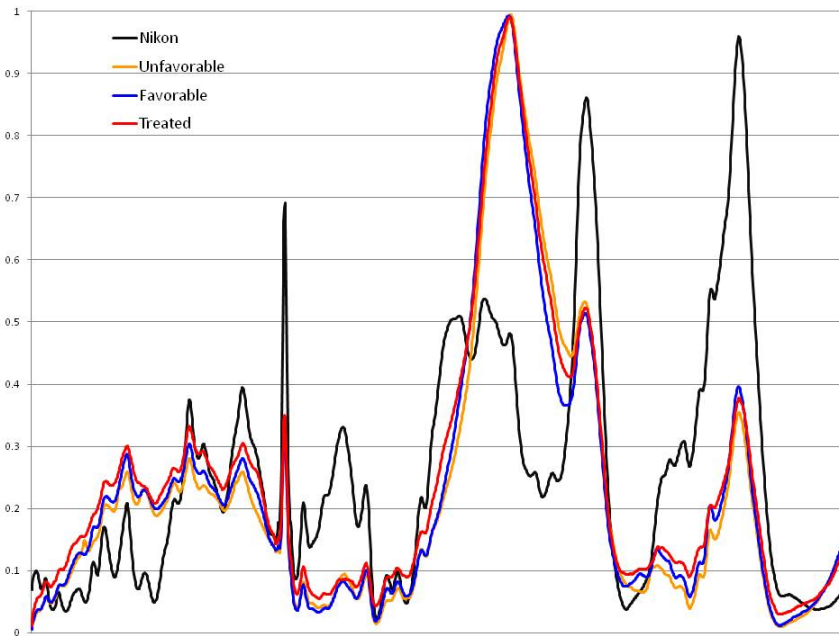


Figure 6.1: mean spectra of favorable, unfavorable, and treated training data, and mean spectrum of unknown data measured with Nikon lens

Further examination of the mean spectra shows that the mean spectra of the unfavorable, favorable, and treated histology training groups each have a maximum of about one, meaning that the data is relatively homogenous. Examination of the testing data measured with the Nikon lens, however, showed a maximum value of only approximately .95. This signifies a less homogenous data set, and likely signals multiple populations within the data set. The data was examined more in-depth to

check for different populations based on the location of the maximum value for each individual spectrum. The training data had very few spectra where the maximum value was outside the range of $1300\text{-}1350\text{ cm}^{-1}$. However, the Nikon testing data displayed four distinct populations, as shown in Figure 6.2. Note that the solid black line is the mean spectrum of the training data measured by the Leica lens and the red, blue, green, and yellow lines are the mean spectra from the four Nikon populations.

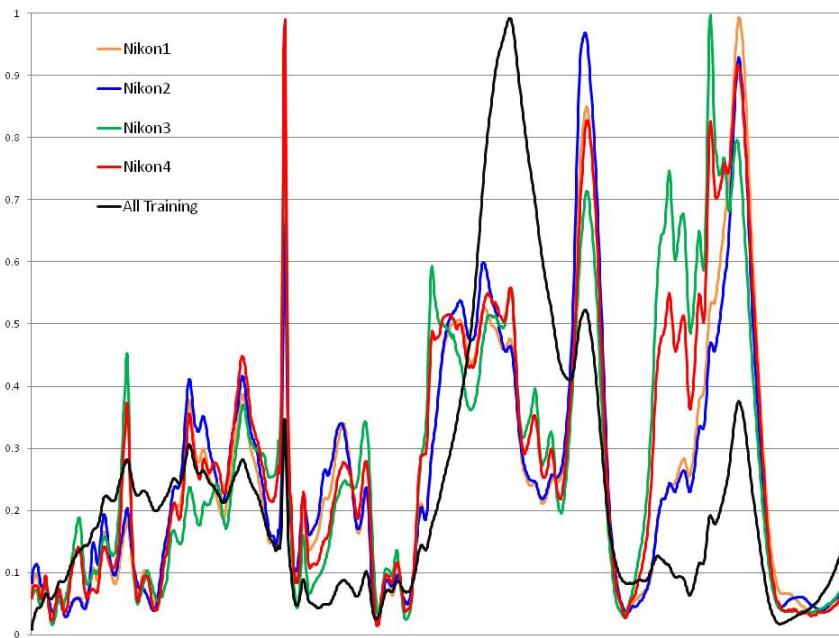


Figure 6.2: Mean spectrum of all training data measured with Leica lens (black) and four distinct populations measured by the Nikon lens.

Because the Raman spectra of the new tissue samples measured with the Nikon lens were so different from the Raman spectra of the training samples measured with the Leica lens, it was not possible to identify the histology of the new samples using existing processing and diagnostic methods. Data collected using the Nikon lens was saved for future use, once processing procedures are adjusted to solve this problem. In

the meantime, a replacement Leica lens identical to the original Leica lens was obtained, and samples were re-measured.

6.3.2 Leica Lens Results

Figure 6.3 shows the mean Raman spectra of the three training data groups measured with the original Leica lens and the Raman spectra of the unknown data measured with the replacement Leica lens. There is much better agreement between the two Leica lenses than between the Leica and Nikon lens, however, minor differences still exist. If the original Leica lens was damaged over time, this would slowly change the amount of light let in by the lens. This could be part of the reason for the measurement differences between the two lenses. Alternately, the lenses might simply provide slightly different signals due to small differences in the manufacturing process.

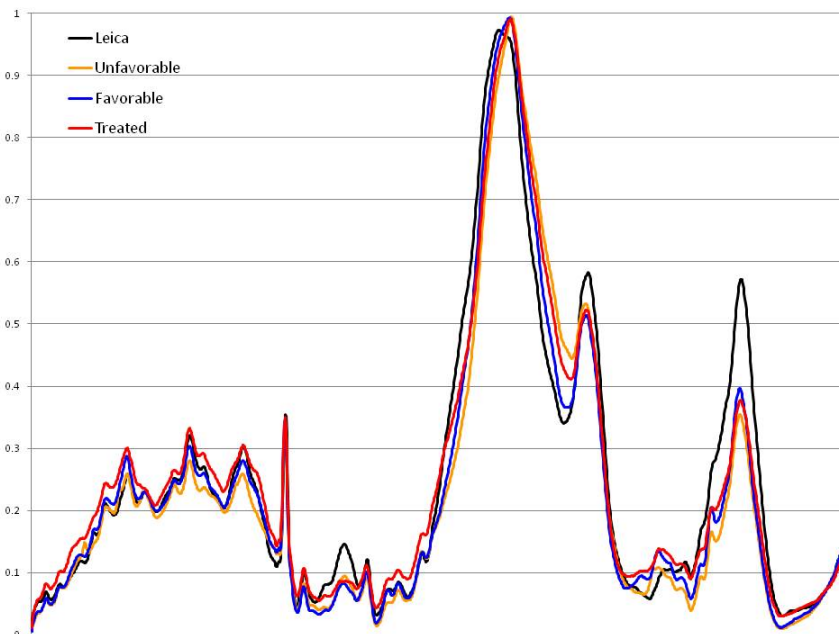


Figure 6.3: Mean spectrum of unfavorable, favorable, and treated training data with unknown data measured using the replacement Leica lens

Data was reviewed to remove any spectra with the maximum value outside the range of 1300 to 1350 cm^{-1} , and then the full spectral data was imported into SPSS. The spectra removed from this process will be referred to as 'obvious outliers'. Data review was also performed to remove any spectra with lower quality Raman spectra, potentially due to out of focus measurements, poor sample quality, or excess measurement noise. These spectra will be referred to as 'potential outliers'. For each method, data analysis was performed twice: once using all data with only obvious outliers removed, and once using data with both obvious outliers and potential outliers removed. The three classification methods which were used for data analysis are described below.

6.3.3 Method 1: Key Peaks from 600-1800 cm^{-1}

Data classification was first attempted using principal component analysis followed by discriminant function analysis. This did not work because the new data did not match closely enough with the old data to be compressed through principal component analysis then analyzed with discriminant function analysis. Next, discriminant function analysis without principal component analysis using all peaks as input was attempted. Again, this failed.

Visual examination of the Raman spectra between the two lenses showed clear intensity differences in some regions. It was hypothesized that classification difficulties might be partly caused by including those regions in data analysis. To try to circumvent this problem, peak selection was performed using the method described in section 4.2.2, based on the standardized canonical discriminant function results of discriminant function analysis using all peaks.

For classifying between treated and untreated neuroblastoma, the selected peaks of interest were 643.7, 655.9, 663.0, 666.1, 667.1, 699.5, 843.9, 855.6, and 1402.9 cm^{-1} . Overall classification of the training data was 77.4%. Table 6.1 shows the results excluding potential and obvious outliers, and Table 6.2 shows the classification results excluding only the obvious outliers.

Classification Results^a

treatment			Predicted Group Membership		Total
			untreated	Treated	
Original	Count	untreated	215	50	265
		treated	43	103	146
		Ungrouped cases	116	103	219
	%	untreated	81.1	18.9	100.0
		treated	29.5	70.5	100.0
		Ungrouped cases	53.0	47.0	100.0

a. 77.4% of original grouped cases correctly classified.

Table 6.1: Classification results of untreated versus treated tissue using select peaks in the range from 600-1800 and excluding potential and obvious outliers.

Classification Results^a

treatment			Predicted Group Membership		Total
			untreated	treated	
Original	Count	untreated	215	50	265
		treated	43	103	146
		Ungrouped cases	134	120	254
	%	untreated	81.1	18.9	100.0
		treated	29.5	70.5	100.0
		Ungrouped cases	52.8	47.2	100.0

a. 77.4% of original grouped cases correctly classified.

Table 6.2: Classification results of untreated versus treated tissue using select peaks in the range from 600-1800 cm^{-1} excluding only obvious outliers.

For classifying between favorable and unfavorable neuroblastoma, the peaks of interest were 614.1, 621.8, 622.3, 626.3, 631.5, 637.6, 638.6, 725.7, 744.7, 768.7, 797.5, 846.8, 825.2, 860.6, 917.1, 924.8, 951.8, 1152.2, 1158.7, 1173.5, and 1312.9 cm^{-1} . This represents significantly more diagnostic peaks than were necessary for

discriminating between treated and untreated neuroblastoma, however, overall classification of the training data was 93.6%. Table 6.3 shows the results excluding potential and obvious outliers, and Table 6.4 shows the classification results excluding only the obvious outliers.

Classification Results^a

Subgroup			Predicted Group Membership		Total
			UNb	FNb	
Original	Count	UNb	123	12	135
		FNb	5	125	130
		Ungrouped cases	61	158	219
	%	UNb	91.1	8.9	100.0
		FNb	3.8	96.2	100.0
		Ungrouped cases	27.9	72.1	100.0

a. 93.6% of original grouped cases correctly classified.

Table 6.3: Classification results of favorable versus unfavorable tissue using select peaks in the range from 600-1800 and excluding potential and obvious outliers.

Classification Results^a

Subgroup			Predicted Group Membership		Total
			UNb	FNb	
Original	Count	UNb	123	12	135
		FNb	5	125	130
		Ungrouped cases	71	183	254
	%	UNb	91.1	8.9	100.0
		FNb	3.8	96.2	100.0
		Ungrouped cases	28.0	72.0	100.0

a. 93.6% of original grouped cases correctly classified.

Table 6.4: Classification results of favorable versus unfavorable tissue using select peaks in the range from 600-1800 cm^{-1} excluding only obvious outliers.

6.3.4 Method 2: Full Data Range from 600-1220 cm^{-1}

Upon in-depth examination of the mean spectra over the range of 600-1800 cm^{-1} and examination of the key diagnostic peaks which were selected using the standardized canonical discriminant functions, it was determined that the mean spectrum of the replacement Leica lens closely matched the Raman fingerprint of the

training data measured with the original Leica lens below about 1250 cm^{-1} . Different cutoff points were iteratively tested to find the maximum classification within the training set. This was done by performing discriminant function analysis over all the peaks from the range of 600 cm^{-1} to the cutoff points being tested. Results of treated versus untreated analysis and favorable versus unfavorable analysis were recorded at each cutoff point. Optimal results for both groups were reached using a cutoff point of 1220 cm^{-1} , so analysis was performed over the range of $600\text{-}1220\text{ cm}^{-1}$.

Figure 6.4 shows the mean spectrum of the new lens and the three training groups over the full data range (left), and over the truncated data range (right). Notice that the black line which signifies the new testing data matches much closer with the training data in the right hand image.

Table 6.5 shows the classification results using all peaks in the range from $600\text{-}1220\text{ cm}^{-1}$ to distinguish between treated and untreated neuroblastoma with obvious and potential outliers excluded, and Table 6.6 shows the same results excluding only obvious outliers. Classification of the training data was 78.3%.

Treatment			Predicted Group Membership		Total
			untreated	treated	
Original	Count	Untreated	223	42	265
		Treated	47	99	146
		Ungrouped cases	143	76	219
	%	Untreated	84.2	15.8	100.0
		Treated	32.2	67.8	100.0
		Ungrouped cases	65.3	34.7	100.0

a. 78.3% of original grouped cases correctly classified.

Table 6.5: Classification results of untreated versus treated tissue using all peaks from $600\text{-}1220\text{ cm}^{-1}$ and excluding potential and obvious outliers.

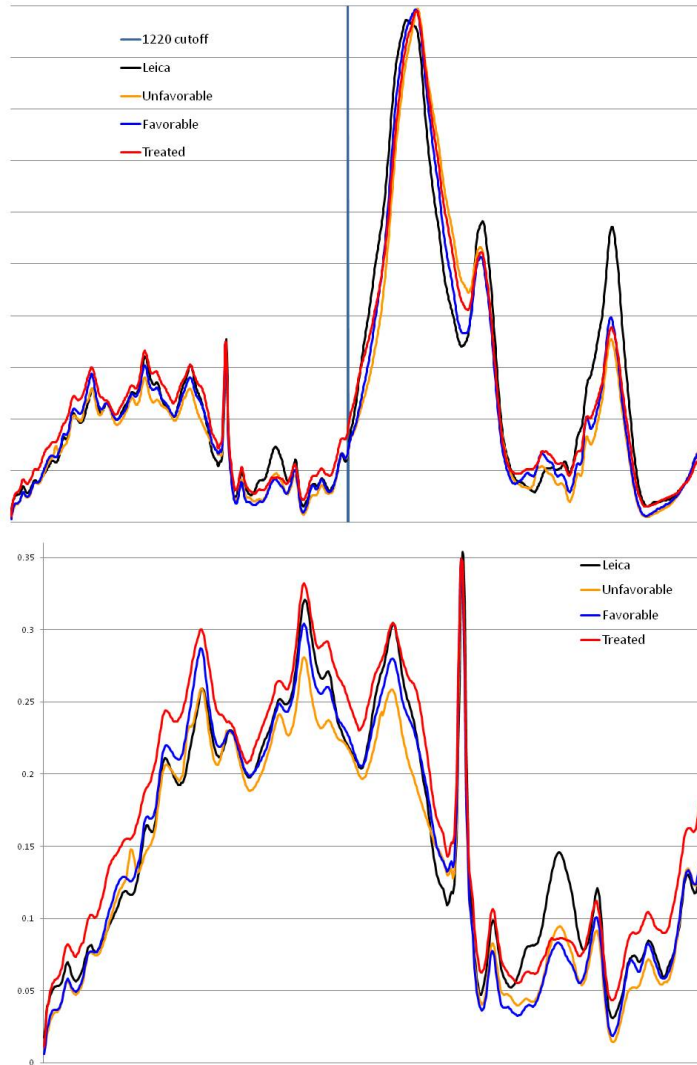


Figure 6.4: Mean Raman spectra of favorable, unfavorable, and treated spectra measured with original Leica lens and unknown spectra measured with replacement Leica lens before (top) and after (below) data truncation

Classification Results

treatment		Predicted Group Membership		Total	
		untreated	treated		
Original	Count	untreated	223	42	265
		treated	47	99	146
		Ungrouped cases	164	90	254
	%	untreated	84.2	15.8	100.0
		treated	32.2	67.8	100.0
		Ungrouped cases	64.6	35.4	100.0

a. 78.3% of original grouped cases correctly classified.

Table 6.6: Classification results of untreated versus treated tissue using all peaks from 600-1220 cm^{-1} and excluding only obvious outliers.

Table 6.7 shows the classification results using all peaks in the range from 600-1220 cm^{-1} to distinguish between favorable and unfavorable histology neuroblastoma with obvious and potential outliers excluded, and Table 6.8 shows the same results excluding only obvious outliers. Classification of the training data was 84.5%.

Subgroup		Predicted Group Membership		Total	
		UNb	FNb		
Original	Count	UNb	118	17	135
		FNb	24	106	130
		Ungrouped cases	119	100	219
		UNb	87.4	12.6	100.0
		FNb	18.5	81.5	100.0
		Ungrouped cases	54.3	45.7	100.0

a. 84.5% of original grouped cases correctly classified.

Table 6.7: Classification results of unfavorable versus favorable tissue using all peaks from 600-1220 cm^{-1} and excluding potential and obvious outliers.

Subgroup		Predicted Group Membership		Total	
		UNb	FNb		
Original	Count	UNb	118	17	135
		FNb	24	106	130
		Ungrouped cases	133	121	254
		UNb	87.4	12.6	100.0
		FNb	18.5	81.5	100.0
		Ungrouped cases	52.4	47.6	100.0

a. 84.5% of original grouped cases correctly classified.

Table 6.8: Classification results of favorable versus unfavorable tissue using all peaks from 600-1220 cm^{-1} and excluding only obvious outliers.

6.3.5 Method 3: Key Peaks from 600-1220 cm^{-1}

Since classification results were so promising using the full range of data from 600-1220 cm^{-1} , individual peak selection was performed within this specific range. For classifying between treated and untreated neuroblastoma, the peaks of interest were 614.1, 617.1, 618.2, 625.3, 704.5, 743.7, 854.6, 1015.0, 1041.6, 1051.1, 1052.2,

1155.9, and 1202.9 cm^{-1} . They provided 81.5% accurate classification of the training data. Table 6.9 shows the classification results using these peaks to distinguish between treated and untreated neuroblastoma with obvious and potential outliers excluded, and Table 6.10 shows the same results excluding only obvious outliers.

Classification Results^a

treatment			Predicted Group Membership		Total
			untreated	treated	
Original	Count	untreated	231	34	265
		treated	42	104	146
		Ungrouped cases	144	75	219
		untreated	87.2	12.8	100.0
		treated	28.8	71.2	100.0
		Ungrouped cases	65.8	34.2	100.0

a. 81.5% of original grouped cases correctly classified.

Table 6.9: Classification results of untreated versus treated tissue using 13 select peaks from 600-1220 cm^{-1} and excluding potential and obvious outliers.

Classification Results^a

treatment			Predicted Group Membership		Total
			untreated	treated	
Original	Count	untreated	231	34	265
		treated	42	104	146
		Ungrouped cases	165	89	254
		untreated	87.2	12.8	100.0
		treated	28.8	71.2	100.0
		Ungrouped cases	65.0	35.0	100.0

a. 81.5% of original grouped cases correctly classified.

Table 6.10: Classification results of untreated versus treated tissue using 13 select peaks from 600-1220 cm^{-1} and excluding only obvious outliers.

The number of peaks could be further reduced to 8 peaks while still maintaining 80% classification of the training data. These 8 peaks were 704.5, 743.7, 854.7, 1015.1, 1041.7, 1051.1, 1052.0, and 1202.9 cm^{-1} . Table 6.11 shows the classification

results using these peaks with obvious and potential outliers excluded, and Table 6.12 shows the same results excluding only obvious outliers.

Classification Results^a

treatment			Predicted Group Membership		Total
			untreated	treated	
Original	Count	untreated	229	36	265
		treated	46	100	146
		Ungrouped cases	143	76	219
		untreated	86.4	13.6	100.0
		treated	31.5	68.5	100.0
		Ungrouped cases	65.3	34.7	100.0

a. 80.0% of original grouped cases correctly classified.

Table 6.11: Classification results of untreated versus treated tissue using 8 select peaks from 600-1220 cm^{-1} and excluding potential and obvious outliers.

Classification Results^a

treatment			Predicted Group Membership		Total
			untreated	treated	
Original	Count	untreated	229	36	265
		treated	46	100	146
		Ungrouped cases	163	91	254
		untreated	86.4	13.6	100.0
		treated	31.5	68.5	100.0
		Ungrouped cases	64.2	35.8	100.0

a. 80.0% of original grouped cases correctly classified.

Table 6.12: Classification results of untreated versus treated tissue using 8 select peaks from 600-1220 cm^{-1} and excluding only obvious outliers.

For classifying between favorable and unfavorable neuroblastoma, the selected peaks of interest were 614.1, 618.2, 622.3, 626.3, 631.5, 637.6, 680.3, 715.6, 744.7, 768.7, 825.2, 846.8, 917.1, 924.8, 951.8, 1152.2, 1158.7, 1175.3, 1184.5, and cm^{-1} . Table 6.13 shows the classification results using these peaks with obvious and potential outliers excluded to separate unfavorable and favorable neuroblastoma, and Table 6.14 shows the same results excluding only obvious outliers. The overall classification was 86.4%.

Classification Results^a

Subgroup			Predicted Group Membership		Total
			UNb	FNb	
Original	Count	UNb	119	16	135
		FNb	20	110	130
		Ungrouped cases	111	108	219
		UNb	88.1	11.9	100.0
		FNb	15.4	84.6	100.0
		Ungrouped cases	50.7	49.3	100.0

a. 86.4% of original grouped cases correctly classified.

Table 6.13: Classification results of unfavorable and favorable tissue using select peaks from 600-1220 cm^{-1} and excluding potential and obvious outliers.

Classification Results^a

Subgroup			Predicted Group Membership		Total
			UNb	FNb	
Original	Count	UNb	119	16	135
		FNb	20	110	130
		Ungrouped cases	128	126	254
		UNb	88.1	11.9	100.0
		FNb	15.4	84.6	100.0
		Ungrouped cases	50.4	49.6	100.0

a. 86.4% of original grouped cases correctly classified.

Table 6.14: Classification results of untreated versus treated tissue using 8 select peaks from 600-1220 cm^{-1} and excluding only obvious outliers.

Peaks selected for treated versus untreated classification are marked in purple in Figure 6.5, and peaks selected for favorable versus unfavorable classification are marked in orange.

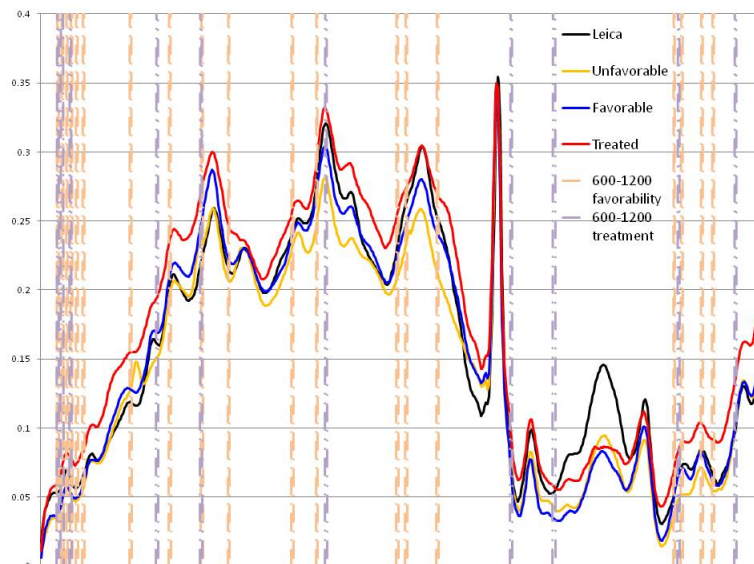


Figure 6.5: Key peaks in the range of 600-1220 cm^{-1} for classification of unfavorable, favorable, and treated neuroblastoma

6.3.6 Comparison of Classification Methods

The classification results for each method used to discriminate between treated and untreated neuroblastoma are shown in Table 6.15. A diagnosis was only assigned to each sample if at least 60% of the individual spectra had the same diagnosis. Samples with 50-60% agreement were not given a diagnosis. Results are shown for analyses excluding only obvious outliers and analyses excluding both obvious and potential outliers. There is also an 'overall diagnosis' which was made based on the combination of the three methods, if they agreed. The 'value' column represents the average diagnosis for each tissue, where 0 is unfavorable or untreated, and 1 is favorable or untreated. Samples with a value of less than 0.4 were untreated (purple), and samples with a value of more than 0.6 were treated (yellow).

Likewise, Table 6.16 shows the same results used to discriminate between favorable and unfavorable neuroblastoma. Samples with a value of less than 0.4 were unfavorable (green), and samples with a value of more than 0.6 were favorable (red).

	TREATMENT								treatment
	453 spectra				419 spectra				
	600-1800 15pk	600-1200 All	600-1200 13 pk	600-1200 8 pk	600-1800 15pk	600-1200 All	600-1200 13 pk	600-1200 8pk	
2001-07-P6020	0.86	1.00	1.00	1.00	0.86	1.00	1.00	1.00	treated
2001-12-P8023	0.50	0.25	0.33	0.17	0.63	0.25	0.50	0.25	untreated
2002-10-P8047	0.00	0.17	0.08	0.00	0.00	0.18	0.09	0.00	untreated
2002-11-P8008	0.78	0.56	0.67	0.67	0.71	0.57	0.57	0.57	treated
2002-12-P6025	0.73	0.18	0.09	0.18	0.78	0.22	0.11	0.22	untreated
2003-01-P8006	0.42	0.67	0.83	0.75	0.50	0.70	0.90	0.80	treated
2003-02-P8005	0.38	0.08	0.08	0.08	0.33	0.00	0.00	0.00	Untreated
2003-06-P8029	0.15	0.38	0.15	0.08	0.15	0.38	0.15	0.08	Untreated
2003-08-P8061	0.60	0.70	0.70	0.70	0.60	0.70	0.70	0.70	treated
2003-10-P8055	0.67	0.58	0.33	0.33	0.67	0.58	0.33	0.33	Untreated
2004-03-P0092	0.36	0.27	0.18	0.27	0.36	0.27	0.18	0.27	untreated
2005-04-P0518	0.00	0.20	0.00	0.00	0.00	0.22	0.00	0.00	untreated
2005-06-P0753	0.54	0.62	0.62	0.54	0.67	0.44	0.56	0.56	Treated
2006-02-P0791	0.91	0.45	0.73	0.73	1.00	0.56	0.78	0.67	Treated
2006-02-P0903	0.00	0.00	0.00	0.00	0.00	0.00	0.00	0.00	Untreated
2006-08-P0687	0.70	0.60	0.70	0.90	0.70	0.60	0.70	0.90	Treated
2006-11-P0514	0.46	0.54	0.31	0.38	0.29	0.57	0.43	0.57	
2006-12-P0503	0.17	0.08	0.00	0.08	0.18	0.09	0.00	0.09	Untreated
2007-01-P0160	0.25	0.17	0.00	0.00	0.25	0.17	0.00	0.00	Untreated
2007-04-P0365	0.50	0.36	0.43	0.50	0.50	0.25	0.42	0.50	Untreated
2007-05-P1011	0.85	0.23	0.31	0.31	0.85	0.23	0.31	0.31	Untreated
2007-09-P0478	0.83	0.08	0.58	0.67	1.00	0.00	0.60	0.60	

Table 6.15: Comparison of tissue-level results using each classification method for treated versus untreated neuroblastoma. 453-spectra results represent analysis with obvious outliers removed, and 419-spectra results represent analysis with obvious and potential outliers removed.

As shown in the Tables 6.15 and 6.16, there is fairly good agreement among classification methods for most tissues. However, some tissues, such as 2007-09-P0478 exhibited a shift from 83% treated to 92% untreated depending on the set of peaks used for diagnosis. In some cases, such as 2006-11-P0514, the diagnosis of the tissue shifted from one group to another when low-quality spectra were removed.

The right hand side of the tables shows the overall classification results. When there was fairly good agreement between the three methods, an overall diagnosis was made. However, samples which were still unclear were left blank.

Tissue ID	FAVORABILITY						Final DX
	453 SPECTRA			419 SPECTRA			
	600-1800 21 pk	600-1200 All	600-1200 19pk	600-1800 21 pk	600-1800 All	600-1200 19pk	
2001-07-P6020	0.86	0.43	0.57	0.86	0.43	0.57	
2001-12-P8023	0.75	0.67	0.75	0.63	0.63	0.75	favorable
2002-10-P8047	0.50	0.25	0.17	0.45	0.18	0.09	unfav
2002-11-P8008	0.56	0.56	0.44	0.71	0.57	0.57	
2002-12-P6025	0.73	0.45	0.45	0.78	0.56	0.56	
2003-01-P8006	0.92	0.67	0.50	0.90	0.60	0.40	
2003-02-P8005	0.77	0.46	0.38	0.83	0.42	0.33	unfav
2003-06-P8029	0.46	0.08	0.23	0.46	0.08	0.23	unfav
2003-08-P8061	0.60	0.20	0.40	0.60	0.20	0.40	unfav
2003-10-P8055	0.75	0.67	0.67	0.75	0.67	0.67	favorable
2004-03-P0092	0.55	0.27	0.27	0.55	0.27	0.27	unfav
2005-04-P0518	0.80	0.60	0.60	0.78	0.56	0.56	favorable
2005-06-P0753	0.54	0.62	0.62	0.56	0.56	0.67	favorable
2006-02-P0791	0.73	0.55	0.73	0.67	0.56	0.78	
2006-02-P0903	0.92	0.08	0.25	0.92	0.08	0.25	unfav
2006-08-P0687	0.70	0.60	0.70	0.70	0.60	0.70	favorable
2006-11-P0514	0.77	0.69	0.46	0.86	0.71	0.43	
2006-12-P0503	0.92	0.58	0.42	0.91	0.64	0.45	
2007-01-P0160	0.58	0.33	0.42	0.58	0.33	0.42	unfav
2007-04-P0365	0.93	0.50	0.64	0.92	0.50	0.58	favorable
2007-05-P1011	0.77	0.54	0.69	0.77	0.54	0.69	favorable
2007-09-P0478	0.75	0.67	0.58	0.80	1.00	1.00	favorable

Table 6.16: Comparison of tissue-level results using each classification method for favorable versus unfavorable neuroblastoma. 453-spectra results represent analysis with obvious outliers removed, and 419-spectra results represent analysis with obvious and potential outliers removed.

6.3.7 Comparison of Raman Diagnosis with COG Diagnosis

Results from Children's Oncology Group showed that Raman spectroscopy did not significantly distinguish between the blinded favorable, unfavorable, and treated samples. Section 6.4 discusses several possible sources for classification error within this study, and suggests possible methods for improvement. In the future, the data will be re-analyzed and results will be re-submitted to the Children's Oncology Group.

6.4 Conclusions

Based on the results of the blinded study, the classification methodology must be further refined to improve classification. Ideally, an ideal methodology will be established in the future, and the Children's Oncology Group will share more of their samples for development of a complete pediatric cancer Raman spectroscopic database.

At the time of preliminary analysis of unfavorable, favorable, and treated neuroblastoma, processing capability did not allow for in-depth peak wise analysis. Because SPSS now allows analysis of full spectral data, significant peak findings can be used to draw biochemical conclusions regarding the samples. In the future, cancer biologists and biochemists will be consulted to correlate the significant peaks with biochemicals, which should allow conclusions to be drawn about the tumor biology.

In the future, there are several ways to improve histologic classification. A further refinement on the terms 'favorable', 'unfavorable', and 'treated' will improve diagnosis. Tumor favorability depends on age (a non-histologic factor); however, age is not related to the underlying tumor biochemistry. Therefore, it should be removed as a factor from histologic diagnosis. Instead, future Raman spectroscopic studies of in-house and

Children's Oncology Group samples should examine the stromal index, MKI, and differentiation individually rather than favorability as a whole.

Likewise, a quantification of treatment, such as maturation, necrosis, etc. should be used instead of simply defining treated and untreated neuroblastoma. These specific descriptions have a concrete link to histology and tumor biochemistry and should allow more accurate Raman diagnosis.

Finally, further development of the Raman tumor database with more samples will increase our classification ability. Classification algorithms and processing techniques will also be continuously refined over time.

Outside of classification of blinded tumor samples, this study raised concerns about the validity of processing and classification methodology when hardware components are changed on the Raman system. The differences between the Leica brand lens and the Nikon brand lens were so pronounced that data from one could not be used to classify data from the other. The differences between the two Leica brand lenses were not as pronounced, however, lens-to-lens classification still posed a significant problem. Future work must be done to address this major problem.

Lenses are not the only spectrometer with a limited shelf life. Other components which may degrade over time include the laser excitation source, filters, and gratings. Furthermore, interchangeable hardware components may be changed over time for application of one Raman probe to different applications. The final software package developed for clinical use must be robust enough to handle the periodic change of hardware components without invalidation of the existing spectroscopic database.

Enhanced background subtraction and calibration techniques, as well as modifications to the data cataloging system should address this problem.

CHAPTER 7 IDENTIFICATION OF MYCN AMPLIFICATION IN NEUROBLASTOMA CELLS

7.1 Introduction

7.1.1 *Genetic Factors Associated with Neuroblastoma Prognosis*

Several genetic factors are associated with neuroblastoma prognosis. Known factors include amplification of the MYCN gene (myc myelocytomatosis viral related oncogene, neuroblastoma derived), change in cell ploidy (number of sets of chromosomes), changes to the 11q chromosome (long arm of chromosome 11), changes to the 1p chromosome (short arm of chromosome 1), and increase of genetic material on the 17q chromosome (long arm of chromosome 17) (Cohn, S. L. et al., 2009). The International Neuroblastoma Risk Group found that the genetic factors most significantly associated with disease prognosis included MYCN amplification, 11q changes, and cell ploidy. Of these genetic factors, MYCN was the most significant. Their study found that the 5-year overall survival rate dropped from 82% in non-amplified MYCN tumors (n=5,947 patients) to just 34% in MYCN amplified tumors (n=1,155 patients) (Cohn, S. L. et al., 2009).

The MYCN proto-oncogene is amplified (50-400 copies/cell) in 20-25% of neuroblastomas (Maris, J. M. Matthay, K. K., 1999). When found at normal expression levels, it is not hazardous; however, when found at increased expression levels, it helps turn healthy cells into cancerous cells. It produces the MYCN phosphoprotein, which interacts with MAX and MAD proteins and leads to changes in several downstream pathways.

It is unknown exactly how MYCN works beyond binding with MAX and MAD, but it is known that it can affect the expression of literally hundreds of other genes (Eilers, M. Eisenman, R. N., 2008). In general, it up-regulates genes involved in protein synthesis, ribosome creation, metabolism, and increasing cell mass, while it tends to down-regulate genes involved in stopping the cell cycle, causing cell adhesion, and allowing cell-to-cell communication (Eilers, M. Eisenman, R. N., 2008).

7.1.2 Regulation of MYCN Expression

Previous reports have shown that retinoic acid (vitamin A) can be used to control N-myc expression, and even cause neuroblastoma tumor cells to differentiate into neuron-like cells (Thiele, C. J. et al., 1985). However, retinoic may not be an ideal model because it can cause differentiation. Differentiation would cause significant changes in the biochemical composition and likely change the Raman signature of the cells, so another model is necessary.

The MYCN gene is particularly difficult to test in cell cultures because it cannot be transfected into animal models (Lutz, W. et al., 1996). This is a similar problem across many types of cells and many genes. To address this general problem, Gossen and colleagues developed a methodology to create cell lines with controllable gene expression (Baron, U. et al., 1995; Gossen, M. Bujard, H., 1992; Gossen, M. et al., 1995).

Using this method, there are two series of transfections into the cell. The first transfection contains the tTa and a plasmid for neomycin resistance. Many cells are transfected in the first step. Of those cells, only cells which exhibit tet-controlled luciferase expression are selected for the second round of transfection. The second

transfection contains tetracycline-controlled cDNA for the gene of interest (NMYC in the case of this research), and another plasmid for hygromycin-resistance. Finally, the selected cells must exhibit resistance to neomycin and hygromycin, and exhibit tetracycline-control of the gene.

Clearly, creation of a tetracycline-inducible cell line is quite complicated and outside the scope of this research. The following sections describe two cell lines previously developed by outside researchers which were considered for use in this study.

7.1.2.1 TET21 Cell Line

Lutz et al. created the first tetracycline-controlled cell line for neuroblastoma in 1996 (Lutz, W. et al., 1996). The original cell line used was SH-EP which is a sub clone of SK-N-SH. They used the transfection method described by Gossen and Bujard (1992) to develop their cell line. This cell line is an example of a TET-off system, because MYCN expression is highest when no tetracycline is present in the cell media. In this cell line, MYCN gene expression was increased 10-fold, and mRNA was increased at least 15-fold. Also of note, light microscopy showed no morphological differences between the induced and non-induced cells.

They found that increased MYCN expression increased the levels of ornithine decarboxylase and the level of α -prothymosin approximately three-fold. It also caused an increase in DNA synthesis and reduced the cell cycle from 16.5 hours in control cells to 11.5 hours in MYCN-amplified cells. Part of this was caused by a quicker transition (about 4 hours) from G₀ to S phase in the MYCN-amplified cells. The time to reach the

G2 phase was the same in both cell lines. The MYCN-amplified cells also grew to higher confluence.

Tests on the transfected cells led to several conclusions which can be applied to this experiment. First immunofluorescence showed that all of the cells in the population responded to the MYCN induction. This means that there should not be cell-to-cell variation in MYCN expression within a batch of treated or untreated cells. Furthermore, both the control cell and tetracycline-induced cell MYCN proteins were able to bind with the MAX protein, so the pathway of the gene should be the same between the treated and untreated cell lines.

When treated to amplify MYCN expression, MYCN protein was detectable in 4.5 hours, and MAX protein was detectable after 5 hours. Conversely, when amplified cells were treated to stop MYCN expression, the MYCN protein levels returned to normal after 4.5 hours.

7.1.2.2 MYCN-3 Cell Line

In 2005, Slack et al. described creation of a second neuroblastoma cell line, in which MYCN amplification could be controlled by tetracycline (Slack, A. et al., 2005). This cell line differs from the previous cell line because it displays MYCN amplification when treated with tetracycline, and it displays normal low-level MYCN when not treated with tetracycline. This is an example of a TET-on gene expression system.

They found the MYCN controls MDM2. That stops p-53 apoptosis. This cancels out the increased apoptosis caused by plain MYCN amplification. MDM2 was increased 1.5-2.5x after MYCN amplification. After induction, MYCN protein levels peak 12-16 hours. MDM2 was increased 2.8-3x after 24 hours MYCN induction.

7.1.3 Research Goal

The goal of this chapter is to determine whether Raman spectroscopy can distinguish between cells with normal levels of MYCN expression and cells with increased MYCN expression. It is unknown whether any changes detected would be due to increased MYCN protein expression or due to other downstream changes caused by increased MYCN expression.

7.2 Materials and Methods

7.2.1 Cell Culture

All cell culturing was performed in a clean room under a negative-pressure hood. The Tet-on MYCN-3 cell line was provided by Dr. Jason Shoet (Texas Children's Cancer Center, Houston, TX). Cells were grown in RPMI 1640 media (Invitrogen) with 10% tetracycline-free Fetal Bovine Serum (Invitrogen) and 1% penicillin/streptomycin (Invitrogen) supplementation. MYCN was induced by adding 1 $\mu\text{g}/\text{mL}$ doxycycline (Sigma Aldrich) to the media.

For the preliminary study, we started with a T75 flask at 100% confluence (~5,000,000 cells). Of those cells, 1/3 were re-plated into 3 T-25 flasks (totaling 1/9 of cells per T25). The other 2/3 of the cells were discarded. The following day, cells from one T-25 flask were isolated for Raman testing and PCR. These cells were called the time=24 hour control sample. At the same time, the media was changed in both of the other flasks, with one receiving plain media and the other receiving media with tetracycline supplementation. 24 hours later, cells from each flask were isolated for testing with Raman spectroscopy and PCR. These cells were called the time=48 hour control and time=48 hour tet-on samples. This experiment was repeated twice.

7.2.2 Cell Isolation

Following trypsinization, cells were centrifuged for 5 minutes at 1200 RPM. The supernate was removed, and cells were resuspended in phosphate buffered saline (PBS). Cells were split between two centrifuge tubes so that three quarters of the cells were reserved for PCR and one quarter of the cells were used for Raman spectroscopy. Both tubes were centrifuged again at 1200 RPM for 5 minutes, and the supernate was removed. The cells for Raman testing were resuspended in 1 mL of PBS. Cells earmarked for PCR testing were either resuspended in lysing buffer and placed on ice until RNA isolation or placed in RNAlater for future RNA isolation.

7.2.3 Raman Spectroscopy

Following isolation, cells were moved from the clean room to a negative-pressure laboratory hood. Cells were mixed with a micropipetter, and then a 200 μ L drop was placed on the end of a spectral grade UV-quartz slide. UV-quartz was selected because it has a relatively low contribution to the Raman spectrum as shown in Figure 7.1.

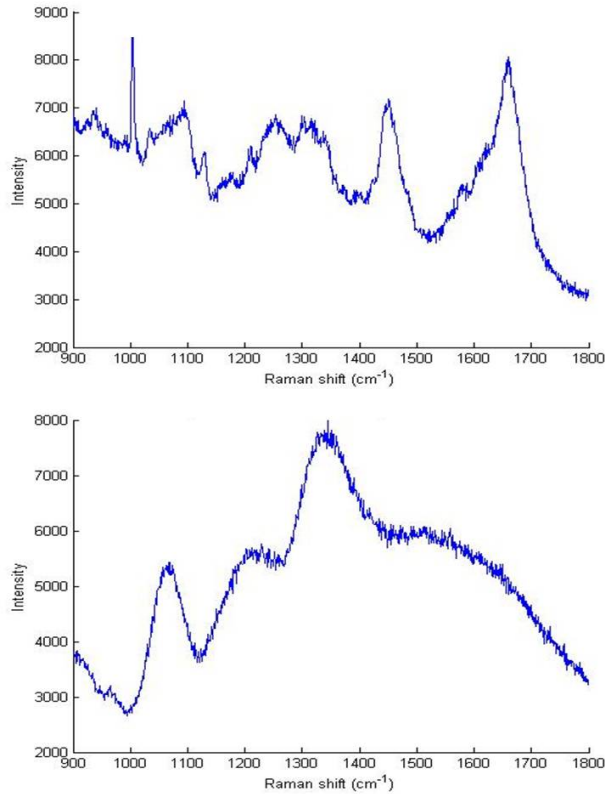


Figure 7.1: Representative Raman spectra of a MYCN-3 cell (top) and UV quartz slide (below)

Raman spectroscopy was performed using a Renishaw InVia Raman microscope with 785nm excitation wavelength and 1200 lines/mm grating identical to the system used in tissue studies. The slide was placed on the microscope objective with the drop end hanging over the edge, as shown in Figure 7.2. Because the cells in suspension and the UV-quartz slide are relatively invisible at 785 nm, the penetration depth of the laser is long enough to also excite the chemical bonds in the microscope stage. Therefore, the cells are hung over the edge of the stage to ensure there is no measurement error due to Raman signal from the microscope stage.

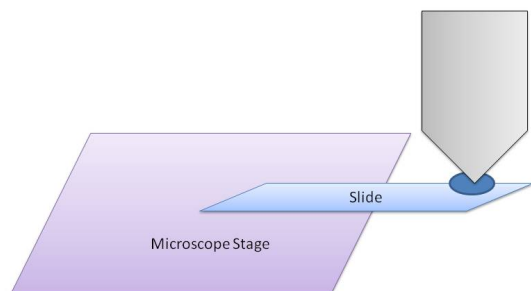


Figure 7.2: Schematic showing cell measurement setup

A 60x Nikon dipping objective was used for all cell experiments. The objective was lowered until it formed a bubble with the cell droplet, and then adjusted to focus on a single cell using the bright field microscope setting. Healthy-appearing, round, single cells were selected for measurement, as shown in Figure 7.3. The focus was adjusted so that cells were surrounded by a white 'halo' as shown in Figure 7.3. Consistent measurement parameters of 10 accumulations of 10 seconds each at 50% power over the range $900\text{-}1800\text{ cm}^{-1}$ were used for all cells. We could not measure the Raman spectrum over the entire Raman range because UV quartz is not entirely invisible at 785nm . We found that the UV quartz caused significant interference below 900 cm^{-1} .



Figure 7.3: a) shows an ideal cell for measurement. The cell is clearly separated from surrounding cells and displays a white 'halo'. b) and c) show examples of cells which would not be measured because they are out of focus and too close to each other.

When the drop of cells dried up or cells started exhibiting visible changes, a new 200 μL drop was placed on the slide. To ensure cells were as close to their true normal state as possible, measurements were only performed within two hours of cell isolation. This time constraint allowed us to measure 12-16 cells per batch.

7.2.4 Confirmation of MYCN Amplification Using PCR

Polymerase chain reaction (PCR) was used to verify the results of tetracycline treatment and amplification of MYCN. Specific details and results can be found in Appendix D.

7.3 Results

PCR results for trial 2 were inconclusive so it was excluded from further analysis. For trial 1, PCR showed that tetracycline-treated cells exhibited about 11.8 times more MYCN cDNA than the non-treated control cells. The time = 24 hour control cells displayed approximately 3 times more MYCN cDNA than the time=48 hour control cells. These results are shown in detail in Appendix D.

Following elimination of Raman spectra with measurement error, the resulting data set for this trial included 8 spectra from the $t = 24$ hour control cells, 6 spectra from the time = 48 h control cells, and 12 spectra from the time = 48h tet-on cells. The mean spectrum of each group is shown in Figure 7.4. As shown, the mean spectra for each group are extremely similar and display only subtle differences.

Preliminary confirmatory analysis was performed on the data using all peaks over the range of 924-1800 cm^{-1} . 924 cm^{-1} was selected as the minimum value because some variables had values of zero below 924 cm^{-1} which adversely affected discrimination results. The three groups were separated with 100% accuracy as shown

by the SPSS output in Table 7.1. Because the data set used was so small (26 spectra), in-depth peak analysis was not performed.

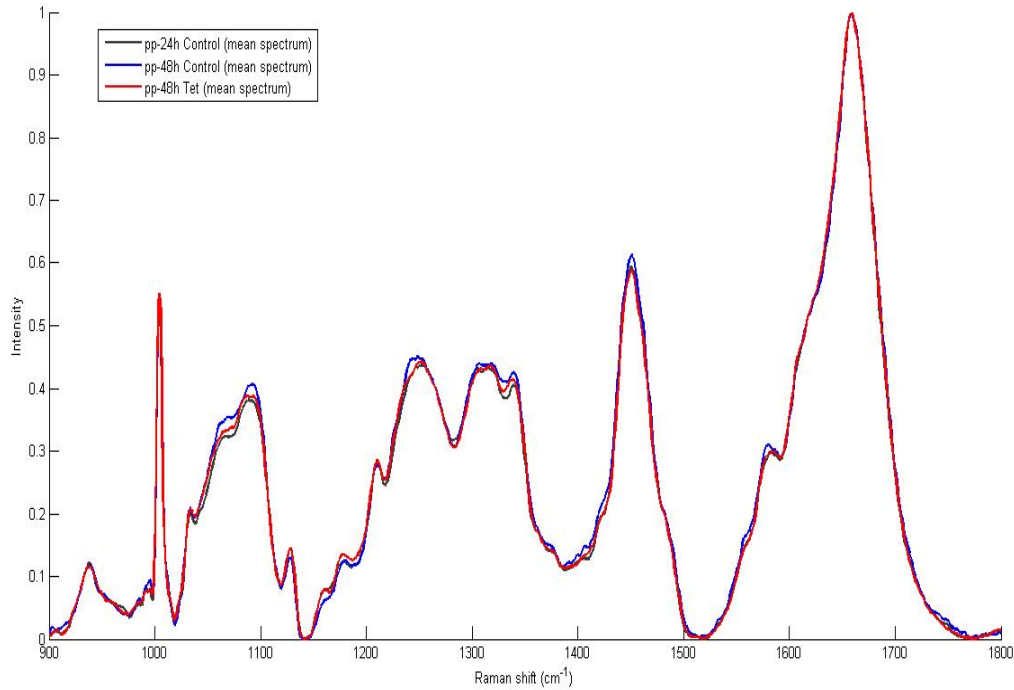


Figure 7.4: Mean spectrum of each group in the 3-flask experiment.

Classification Results^a

	Group	Predicted Group Membership			Total
		1	2	3	
Original Count	1	8	0	0	8
	2	0	6	0	6
	3	0	0	12	12
<hr/>					
	1	100.0	.0	.0	00.0
	2	.0	100.0	.0	00.0
	3	.0	.0	100.0	00.0

a. 100.0% of original grouped cases correctly classified.

Table 7.1: Classification results using all peaks from 924-1800 cm⁻¹. Group 1 is the control group at t=24h, Group 2 is the control

7.4 Conclusions

This is the first study to examine the changing Raman spectra in a tetracycline-controlled cell line. Tetracycline was used to increase the level of MYCN RNA within the cells. While it is not known if Raman spectroscopy is sensitive enough to measure the minor RNA changes in the cell, it should be sensitive enough to measure the effect of increased RNA and effects of other downstream regulatory changes, such as changes to the cell wall and receptors.

A tetracycline-inducible cell line model was chosen for preliminary testing for several reasons. First, the changes to the cell line caused by altered genetic expression are expected to be very subtle. Testing a tissue model might obstruct the subtle changes of MYCN amplification due to the other extra-cellular components.

Second, using a tetracycline-controlled cell lines allows isolation of all other experimental factors. MYCN is associated with other poor prognostic factors, including tissue histology. Testing MYCN amplification in a tissue model would inherently include histologic and other factors in the analysis, confounding the results. Likewise, confounding variables would be hard to eliminate when testing several cell lines with and without MYCN amplification. Tetracycline-inducible cell lines offer the most control over all other outside variables.

An extensive study is needed to confirm the results found here. A potential study design is described in Chapter 9, Future Work. Hopefully, that research will further pinpoint which peaks are diagnostically useful in measuring MYCN amplification. Once diagnostic peaks are selected, other neuroblastoma cell lines can be examined for MYCN amplification. Catalogues exist which identify the MYCN genetic status of

various neuroblastoma cell lines (Thiele, C. J., 1998). Finally, once MYCN amplification measurement is firmly established in cell lines, it can confidently be applied to tissue models. MYCN amplification is routinely tested during pathology workup, so existing measurements could be used by simply correlating patient records to current Raman spectroscopic data (with proper Institutional Review Board approval).

Some cells with MYCN deficiency still over express the MYCN protein (Cohn, S. et al., 1990; Wada, R. K. et al., 1993), but ALL cells with MYCN amplification have MYCN overexpression. While it might not be possible to guarantee the presence of the MYCN gene amplification, Raman spectroscopy could definitely act as a screening tool for detecting tumors at risk for MYCN gene amplification. If Raman could rule out 2/3 of cases which definitely do not have MYCN amplification and genetic tests were run only on the remaining 1/3 with MYCN protein, this would still offer a significant clinical improvement.

In performing this study, other incidental findings were made (not mentioned in text) which may have scientific significance. The Raman spectra of the MYCN3 cells exhibited changes when the CO₂ level of the cell incubator was low, and when the cells changed from low- to high-confluence. Further testing of these findings may show that Raman spectroscopy might have capability to act as a monitoring tool for cell viability.

While the results of this experiment are promising, they can only be counted as preliminary. Only 26 spectra were included in the data analysis. In order to validate these findings, the experiment must be repeated. Acquisition of more spectral data will also allow for identification of diagnostically significant peaks, which can provide

information about the underlying biochemical changes caused by increased MYCN gene expression levels.

CHAPTER 8 CONCLUSIONS

8.1 Summary of Findings

Neuroblastoma was successfully distinguished from other peripheral nervous system tumors, including ganglioneuroma, nerve sheath tumor, and pheochromocytoma. It was also distinguished from healthy adrenal gland. This is significant because it is the most common site of incidence for neuroblastoma. Likewise it was successfully distinguished from tumors with similar histology, including rhabdomyosarcoma, non-Hodgkin lymphoma, and Ewing sarcoma. Improved processing techniques allowed identification of specific peaks which were diagnostically significant.

Frozen tissues were evaluated to see if they could be used within a diagnostic database. Fresh tissue data classified frozen tissue data with 100% sensitivity and specificity. Frozen tissue data could classify fresh tissue data with high sensitivity and specificity as well, although the inclusion of more data should further improve results.

In-depth examinations of some prognostic markers of neuroblastoma were also performed. Raman spectroscopy was able to identify favorable and unfavorable histology neuroblastomas, as judged by the Shimada classification in fresh and frozen tissues. A blinded study of frozen tissues supplied by the Children's Oncology Group was performed to further gauge classification ability.

Finally, the tetracycline-controlled MYCN-3 cell line was used to identify the specific changes due to increased MYCN gene expression in a cell line. These results can later be validated with additional testing. It may be possible to extrapolate these findings to whole tissue samples.

8.2 Novelty and Significance

This is the first research using Raman spectroscopy to identify cancer in a human pediatric model, specifically, neuroblastoma. While many other types of cancer with higher incidence rates have been examined, tumors with lower incidence have largely been ignored. Neuroblastoma was identified from other tumors of the peripheral nervous system, and from tumors which had very similar histologies.

Identification of neuroblastoma from other small round blue cell tumors is especially significant, because current state of the art tests take two days or more. Rapid identification of neuroblastoma and other small round blue cell tumors offers a considerable improvement in patient care, and allows immediate treatment planning.

This is the first study using Raman spectroscopy to identify the favorability of a tumor. The histologic Shimada classification is an important factor in determining the prognosis of a neuroblastoma tumor. Using Raman spectroscopy could offer a more objective evaluation of tumor histology (and underlying biochemistry) and remove inter-observer bias.

Evaluation of frozen tissues provided by the Children's Oncology Group led to several questions which must be addressed in the future. Specifically, better methods for classifying tumor histology were proposed, removing age from an otherwise biochemical-based histologic classification, and judging effect of treatment by specific histologic changes which occur in the tissue. Additionally, future studies must also be performed to better understand the changes caused by switching components in the Raman spectrometer, and to address these issues, possibly through enhanced data processing techniques.

Finally, this is the first study which measures changes in genetic expression within cells using Raman spectroscopy. Genetic testing takes several days to reach a definitive diagnosis, whereas Raman spectroscopy can provide an immediate answer. Again, this offers a major benefit over the accepted testing method.

If each of these individual testing components is combined into a single model, Raman spectroscopy could provide an immediate, complete diagnosis of neuroblastoma, including an objective measure of tumor aggressiveness. If Raman spectroscopy is used in the operating room, physicians can begin development of a treatment plan before the surgery is complete. Increased accuracy in diagnosis may improve development of treatment plans, leading to better outcomes, just as shorter time to treatment may improve outcomes.

Improved diagnostic models may also allow for real-time scanning of tumor margins during tumor resection surgeries. Normally in tumor resection, the area surrounding the tumor (margin) is sent to the pathology laboratory while the surgery is in progress. An experienced pathologist examines the tissue for any remaining tumor cells. If cells are found near the excision border, more tissue is removed and again sent for pathologic testing. This process is expensive and time consuming. It may be possible, instead, to scan the tumor margins intra-operatively for remaining tumor cells. It could offer quicker and more accurate results than frozen section analysis.

Since this research was extremely successful in identifying neuroblastoma and its prognostic markers, another logical next step is to expand the research to other tumors. Raman spectroscopy has strong potential to dramatically impact the field of cancer diagnosis if other tumors can be identified as well as neuroblastoma.

CHAPTER 9 FUTURE WORK

While this work represents a great advance in clinical applications for Raman spectroscopy, specifically for advanced diagnosis of neuroblastoma, it naturally leads to many more questions and problems which must be addressed.

9.1 Data Processing to Account for Changing Hardware Components

Before Raman spectroscopy can be used clinically as a diagnostic tool, there must be a system developed which can account for changes in the Raman spectra due to switching out hardware components within the system. For example, Chapter 6 discusses the differences in the Raman spectra between two Leica-brand lenses and one Nikon-brand lens. Each lens had different underlying background signals, even when measured on the same tissue.

When Raman spectroscopy is used clinically, the system will have even more components which can impact the Raman spectra. Parts such as filters, grating, and even laser light sources vary slightly from piece to piece, and they each have a limited shelf life. This means system components may change throughout the lifespan of a product. As a specific component begins to fail, the Raman spectroscopy may exhibit subtle changes over time. Furthermore, an ideal Raman spectrometer would have interchangeable parts so it could be customized for specific applications.

These needs require a method for normalizing variations in Raman spectra due to changing equipment. Since software methods already exist for background subtraction, they may be the best avenue for addressing these needs in the future.

9.2 Clinical Testing for FDA Approval and Obtaining Reimbursement Codes

Before moving into the truly clinical realm, Raman spectroscopy must go through a series of validation steps, including FDA approval. This includes approval of the instrument to be used as well as the diagnostic algorithms and databases used. As a starting point, the FDA safety requirements and procedures must be examined. Once the process is understood, the application process can begin.

Simultaneously, investigation should begin towards establishing a standardized reimbursement code (CPT) for hospitals to use in procedural billing (Association, A. M.). The technology may fall under an existing code, or it may require development of a new code. If that is the case, a Category III (experimental) code can be obtained during FDA testing (Association, A. M.). Within five years, it can be changed to a Category I (procedural) code once requirements for a Category I code are met (Association, A. M.).

9.3 Study Expansion to Other Pathologies

Neuroblastoma represents just one of dozens of diseases which pose significant diagnostic problems. Since Raman spectroscopy displays great promise in diagnosing neuroblastoma from similar tumors and great promise in diagnosing specific parameters of neuroblastoma aggressiveness, it is logical that it be applied to other diseases and disease processes. It can also be used to track the effects of drug treatment, either through tissue testing, or ex-vivo testing on cells.

When higher incidence tumors are studied, there is also a possible business opportunity for developing commercial laboratory and surgical biopsy tools. A brief market analysis of high-incidence tumors is shown in Appendix E.

9.4 Biochemical Correlation to Raman Spectroscopic Peaks

The studies described in this dissertation go as far as to identify peaks which are diagnostically significant. However, there is not yet an attempt made to correlate these peaks to their biochemical correlates. Some of the Raman peaks which were diagnostically significant were actually valleys or slopes between peaks. An in-depth study is needed to determine why these Raman features were significant and to determine what they represent. Once the identity of the Raman features is established, they can be traced back to the underlying cancer biology, and conclusions can be drawn regarding underlying biological processes in the disease progression.

9.5 Development of a Cell-Line Database

Raman spectroscopy was highly sensitive and specific at detecting even the most subtle genetic changes in the MYCN-3 cell line. This suggests that Raman spectroscopy could easily detect less-subtle changes within cells, and it should easily be able to distinguish from cell line to cell line. Building a database of existing cell lines would provide a valuable tool to basic science researchers. Once a database is created, further subtleties can be cataloged, including changes in the Raman signature due to genetic alteration, drug treatment, etc.

An incidental finding in this work was that Raman spectroscopy could detect changes in the Raman signal of cells due to changes in their environment. Changes which appeared to be measurable using Raman include cell confluence, CO₂ levels in incubation, and quality of cell media being used. While monitoring these changes does not relate to cancer diagnostics, it opens up another avenue for Raman spectroscopic research.

9.6 In-Depth Measurement of MYCN Gene Amplification

The research performed measuring MYCN amplification was only a preliminary study. Further testing is necessary to confirm these results. A detailed follow-up study is outlined which measures MYCN amplification at several time points and compares it to untreated control samples at every time point. If there are measurable changes due to cell confluence, this experiment will also find those changes.

First, determine a growth curve for the cell line to determine the ideal plating densities. Grow cells to confluence in a T-75 flask. Trypsinize the flask and split the cells equally into 7 groups. Isolate 1/7 of the cells for immediate Raman testing. Replate the remaining six groups into six T-25 flasks. They should be plated at approximately 20% confluence. Treat three of the flasks with doxycycline to induce MYCN amplification. Harvest the cells and measure the Raman signatures from one control and one MYCN-amplified flask at the time points of 6 hours, 24 hours, and 48 hours. Figure 9.1 graphically depicts the experimental design.

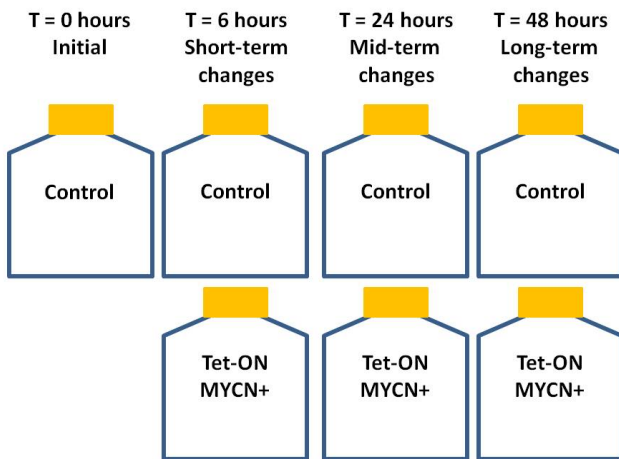


Figure 9.1: Experimental design. Control cells were tested at time = 0 hours. Control and MYCN-amplified cells were tested at time = 6 hours, 24 hours, and 48 hours.

APPENDIX A INTERNAL REVIEW BOARD DOCUMENTATION

1. COPY OF CURRENT PROTOCOL

Raman Spectroscopy for Diagnosis of Pediatric Neoplasms

Objectives:

This project seeks to evaluate the Raman spectroscopic signals associated with normal and malignant variations of different pediatric tissues. The specific objectives of this project are:

1. Use variations in spectra to differentiate between normal, benign, and malignant tissue.
2. Examine various tumor grades of the same tissue type in order to allow development of a new grading scale for tumor differentiation based on molecular composition.
3. Build a database of frozen tissues, which are more easily accessible. Frozen tissues can be correlated to similar fresh tissues.
4. Develop a Raman spectroscopy database of various tissue types.
5. Finally, our goal is to use the identified wavelengths for tissue diagnosis and condense the laser mechanism to incorporate laser emission and signal detection into a fiber optic probe. This will allow intra-operative use in tumor diagnosis and scanning tumor beds for residual malignant cells.*

Background Information:

Currently, gross and histopathologic diagnosis is routinely performed for resected tissue in cases of neoplastic growth. These diagnoses are often times delayed, inaccurate on frozen section and provide limited prognostic value. The state of genetic

testing and prognostication are not fully developed and are mainly utilized in academic investigation.

Various alterations occur during the degeneration of normal tissue to neoplastic tissue. As a result of this process, the cellular makeup of this tissue can be significantly different. For example, changes in protein to lipid ratios, protein and DNA modifications and or changes in DNA content have been reported to occur in association with neoplastic change. These tissue changes can be precisely detected by Raman spectroscopy.

The Raman Effect occurs when light incident on a sample is scattered at a new wavelength due to donation of energy to the sample's vibrational bonds. A photon of a new wavelength is emitted, and the change in wavelength is proportional to the change in vibrational energy in the sample. These changes in wavelength can be correlated with specific chemical constituents, yielding a "molecular fingerprint" that is unique to each sample.

In the past decade, Raman spectroscopy has been applied for identification of human normal and malignant tissues, including breast (Haka, A. S. et al., 2006b), skin (Nijssen, A. et al., 2007), colon (Chowdary, M. V. et al., 2007), esophagus (Shetty, G. et al., 2006b), neuroblastoma (Rabah, R. et al., 2008; Wills, H. et al., February 2008), and Wilms' Tumor (Wills, H. et al., (Submitted)) with high sensitivity and specificity. Specifically, our group has published reports on breast cancer (in mice) (Kast, R. E. et al., 2008; Thakur, J. S. et al., 2007), pancreatic ductal carcinoma (in mice) (Pandya, A. et al., 2008), neuroblastoma and related nerve tumors in children (Rabah, R. et al., 2008; Wills, H. et al., February 2008), and Wilms tumor in children (submitted) (Wills, H.

et al., (Submitted)). We have also examined smaller samples of many pediatric cancers, including brain, bone, lymph node, testicular and soft tissue cancers. To date, we believe we are the only group which focuses specifically on pediatric neoplasms.

Our long-term goal is to develop a fiber-optic probe which can be used to evaluate tissue disease status in near-real time. This will have applications from basic science to margin assessment in tumor resection.

Aims:

The aims of the study are to evaluate all tissue resections or biopsies obtained by various surgical specialists at Children's Hospital of Michigan, and Detroit Receiving Hospital. Such methods will reveal spectral correlates of normal and abnormal tissue in children compared to pathologic readings to determine validity of this new technique. This technique will be utilized on fresh tissue and archived tissue from pathology.

This data will be used in developing microprobes that will allow *in vivo* detection of tissue in a less invasive and more accurate manner. This will also serve as an important diagnostic tool in evaluating the tumor bed after resection.

Materials and Methods:

Patient Selection-Inclusion/Exclusion Criteria:

All patients at Children's Hospital of Michigan and Detroit Receiving Hospital that undergo resection or biopsy will be eligible for the study. The study will encompass all surgical fields and will attempt to evaluate all tissue regardless of site of origin. Only patients who do not have sufficient tissue to evaluate by both histopathology and by Raman spectroscopy will be excluded. Pathology will have the priority in evaluating tissue for diagnosis.

The study will involve a minimum of 600 subjects with the aim of developing a Raman database of various tissue types. Hepatoblastoma, neuroblastoma, Wilms tumor, Ewing sarcoma, lymphoma and intracranial neural tumors are some of the malignancies that will be evaluated, but we will also evaluate normal tissue from many organs. Subjects will be enrolled regardless of gender, race, or ethnicity. All patients identified as having tissue submitted for pathologic diagnosis will be enrolled. Normal control samples will be obtained from autopsy cases. A copy of the autopsy consent form is attached.

There will be no additional risk to the patients as a result of conducting this study. All samples will have undergone resection or biopsy as a matter of diagnostic and therapeutic intervention. This study will only utilize tissue samples already removed from the patient.

No consents will be obtained, but patient confidentiality will be maintained. The study coordinator (RK) will be responsible for maintaining all medical information. Any identifying patient information will be removed from records before being accessed by the rest of the group. Patients will be assigned a unique identifier which is not associated with a patient record number. The link to patient information will be stored on a computer in the department of surgery office.

Apparatus

A Raman spectroscopy unit consists of an Argon pumped Titanium: Sapphire laser, collection optics and spectrometer with a silicon based charge-coupled device (CCD). Selected wavelengths (514.5 nm & 785 nm) with detectable reflected intensities will be studied. These wavelengths were selected due to their use in previous studies

and existing knowledge of Raman effect on biologic tissue at varying wavelengths while limiting background fluorescence.

A Verax InPhotonics portable Raman spectrometer is also available with a 785 nm, 350 mW class III excitation laser. There is a short fiber optic coupling probe, and a long, skinny attachment. The probe will be used to interrogate pathology samples and will not be used for in-vivo testing.

Background spectra of samples will be obtained for the glass slide, cover slip, Acrytol mounting media, formalin and paraffin. This background spectral data is important in studying tissue because these chemical signatures may be included in the spectral findings. Once background information is collected, archived tissue slides of hepatoblastoma, neuroblastoma and Wilms tumor along with normal tissue from the same patients will be analyzed.

Raman Measurement

The Raman technician will cut the tissue into smaller specimens if necessary, and measure the Raman spectrum of the tissue using a Raman spectrometer. Raman spectroscopy is performed by mounting the tissue sample on a microscope stage (translational stage) with x, y and z coordinates. No sample pre-treatment of any kind will be performed on the tissue prior to spectroscopic examination. The laser light is focused on the tissue and the Raman spectra will be measured using a 10 second exposure time. Two exposures will be obtained to get an average reading for better signal-to-noise ratio. At least 12 spectra will be obtained from each tissue for each wavelength of light, unless quality spectra cannot be obtained from the sample. Spectra will be collected at random locations for each sample.

Following measurement, samples will be placed in a cryovial, labeled with a unique pathology code, and stored in a -80°C freezer. At a later date, tissues will be removed from the freezer, placed in saline, thawed for 20-60 minutes, and tested again according to the same procedure. Following testing, the samples will be replaced in the cryovial and put back in the freezer.

Periodically (depending on the rate of accrual), study pathologists (RR or JP) will again remove the frozen samples to cut a frozen H&E section; the remainder of the tissue will again be stored in the freezer. Frozen sections will be examined by light microscopy to determine the 'gold standard' diagnosis, which will be used to create a model of the tissues.

Tissues will be stored in the freezer for up to 10 years, in case there is question about the diagnosis of the sample. In the event of a disagreement between histology and Raman spectroscopy, a second frozen H&E section will be cut to re-examine the tissue with light microscopy. If a Raman spectrometer is obtained which uses a different excitation wavelength, tissues may be re-examined at the new excitation wavelength to help construct a database at the new wavelength.

COG Samples

Additional samples will be shipped frozen to Children's Hospital of Michigan from the Children's Oncology Group.

Data Management

The study coordinator will be in charge of the data management. She will be primarily responsible for arranging sample delivery from the operating room, arranging testing schedules for researchers, doing the data processing, and downloading the data

to a secure server. She will record diagnostic information provided by pathologists and store patient records in a locked drawer in the Harper Hospital surgery offices. Data will be stored on a secure online server. Parameters for each tissue, including the tissue code, date collected, and type of disease will be stored on a secure online SQL database, with links to the data files on the secure server. Only the study coordinator will have access to patient-identifying information.

Conflict of Interest and Funding

There are no conflicts of interest to report for any of the investigators. The study will be funded by Children's Hospital of Michigan.

Statistical Analysis:

10-20 spectra will be collected from each tissue sample. Each spectrum will be pre-processed by an algorithm to remove cosmic rays, noise and fluorescence background from the Raman spectra (Cao, A. et al., 2007). Spectra will be evaluated with all peaks, in order to get the full biochemical understanding of the sample, however, spectra will also be compressed using Principal Component Analysis to minimize file size for diagnostic testing. Variations in peak spectra for patient to patient variability as well as variability between archived and fresh tissue of similar tumors will be analyzed.

Box plots will be used to remove outliers from the data. Relevant peaks for biochemical analysis can be chosen using four approaches: (1) Subjective observation of the spectra by an experienced Raman investigator, (2) A Matlab program will be created which will extract the N highest peaks, (3) Relevant literature will be consulted which lists the Raman peaks for specific chemicals, (4) Principal component analysis

(PCA) will be used to reduce the data into a smaller number of variables. We will retain the first N principal components that account for >90% of the variance.

Discriminant Function Analysis and Neural Networks will be used to build diagnostic models of the tissues for classification. The 'gold-standard' diagnosis provided by the pathologists will serve as the training mechanism. Two approaches will be used for testing and training, as both have benefits and drawbacks: (1) data sets will be randomly split in half, with one half being used for 'training the model' and the other half being used for 'testing the model'. After classification, the groups will be reversed to get a classification picture of the whole dataset. (2) Leave-one-out analysis will create a model of the tissues based on all the spectra except one. The single spectrum will then be tested with the model. After testing, that spectrum will be replaced in the dataset and another spectrum will be removed. Again, a new model will be created, and the spectrum will be tested on that model. The process repeats until all the spectra have been tested in this manner.

When the data and histological diagnosis permits, we will breakdown the tumors according to the grade, treatment, or other parameters and repeat the procedure to determine the sensitivity and specificity for different grades of tumors. Analysis will also be done to examine the effects of freezing on Raman spectra. If frozen spectra

Significance:

This work has potential significance in tumor diagnostics. It can serve in a minimally invasive fashion and allow optical diagnosis of abnormal tissues. It may also lead to developing better prognostication data and serve to yield a molecular analysis of gross tissue. These molecular signals may allow for further classification of tumor

variants and allow for more precise grading. It also holds potential for tumor bed scanning and obtaining a molecular scan of surface tissue to detect abnormal areas.

Budget Justification:

The College of Engineering has been working on issues relating to the automotive industry and has started to become more interested in biomedical engineering. The School has acquired many expensive fabrications and measurement instruments over the years and will fully utilize them in this project.

The requested items under supplies are specific for this project due to the necessary adaptation to the equipment to perform these readings. An example is the translation stage and mounting posts kit required for measurements on slides or tissue cassettes. Other items such as sapphire substrates are consumable items utilized over the course of the project. The other major items are two notch filters required specifically for the wavelength utilized for biologic tissues. All of the major equipment is already on site and will not be paid for in any manner by this grant. No items are being requested for this study, as they are already available on-site.

2. 2009 PROGRESS REPORT SUBMITTED TO IRB

Our hypothesis is that an imaging technique called Raman spectroscopy can distinguish between normal and cancerous tissue. The goal of the study is to develop a Raman database of various tissue types. Building a database of 'normal' versus neoplastic tissues will aid in the development of a surgical tool for near real-time cancer detection.

We collect normal and tumor tissues from resections and biopsies obtained from the operating room. We also collect tissue samples from autopsies. Most tumors have some normal tissue at its surroundings. When possible, the pathologist takes two samples from the tissue: one tumor and one normal. We collect Raman signals from both samples. Then the samples are sent to histopathology, or frozen for future testing. The Raman signals are statistically analyzed to see if there are any differences between normal and cancerous tissue. We also see if we can predict what kind of sample it is from the Raman signal. This prediction is compared to the histopathological findings.

We recently began collaboration with the Children's Oncology group, where they sent us frozen samples of neuroblastoma (cancer of the adrenal gland or nerves) and similar tissues. This blinded study will support our hypothesis and aid us in collecting this rare type of tumor.

We have collected 350 tissues from 30 different tissue types. This year, two of our papers were published (submitted last year, titled: *Raman Spectroscopy Detects and Distinguishes Neuroblastoma and Related Tissues in Fresh and (Banked) Frozen Specimens*, and *Diagnosis of Wilms Tumor Using Raman Spectroscopy*), and we submitted a new paper to the journal of pediatric surgery titled "Differentiation of Small

Round Blue Cell Tumors Using Raman Spectroscopy". Instead of comparing normal vs. cancerous, this paper compared tumors which look the same using traditional pathology methods. Our findings showed that Raman spectroscopy can quickly and accurately distinguish these types of tumors which are otherwise hard to tell apart. We will also present this paper at the American Academy of Pediatrics National Conference and Exhibition October 17-20, 2009 in Washington DC.

3. 2009 IRB CONTINUATION APPROVAL

**WAYNE STATE
UNIVERSITY**

HUMAN INVESTIGATION COMMITTEE
101 East Alexandrine Building
Detroit, Michigan 48201
Phone: (313) 577-1628
FAX: (313) 993-7122
<http://hic.wayne.edu>



NOTICE OF EXPEDITED CONTINUATION APPROVAL

To: Michael Klein
Surgery/Pediatrics
Pediatric Surgery

From: James E. Puklin, M.D. *J. Puklin (Kain)*
Chairman, Human Investigation Committee

Date: September 15, 2009

RE: HIC #: 018201MP4E
Protocol Title: Raman Spectroscopy of Pediatric Neoplasms
Sponsor: * Pediatrics
Protocol #: 0506002366
Expiration Date: September 14, 2010
Risk Level / Category: 45 CFR 46.404 - Research not involving greater than minimal risk

Continuation for the above-referenced protocol and items listed below (if applicable) were APPROVED following Expedited Review by the Chairperson/designee of the Wayne State University Institutional Review Board (MP4) for the period of 09/15/2009 through 09/14/2010. This approval does not replace any departmental or other approvals that may be required.

- * Federal regulations require that all research be reviewed at least annually. You may receive a "Continuation Renewal Reminder" approximately two months prior to the expiration date; however, it is the Principal Investigator's responsibility to obtain review and continued approval before the expiration date. Data collected during a period of lapsed approval is unapproved research and can never be reported or published as research data.
- * All changes or amendments to the above-referenced protocol require review and approval by the HIC BEFORE implementation.
- * Adverse Reactions/Unexpected Events (AR/UE) must be submitted on the appropriate form within the timeframe specified in the HIC Policy (<http://www.hic.wayne.edu/hicpol.html>).

NOTE:

1. Upon notification of an impending regulatory site visit, hold notification, and/or external audit the HIC office must be contacted immediately.
2. Forms should be downloaded from the HIC website at each use.

*Based on the Expedited Review List, revised November 1998

4. 2009 IRB CONTINUATION FORM

Submission Instructions for HIC Continuation Form

Requests for continuation of a currently approved research protocol will be reviewed at a regularly convened meeting of the IRB committee that issued the original approval unless the criteria for expedited review are met.

1. Expedited Review for Continuation

Research that meets the following criteria may be reviewed by the HIC chair or his/ her designee:

- a) Where project was originally given an expedited approval;
- or
- b) Where:
 - (i) the research is permanently closed to enrollment of new subjects; and
 - (ii) all subjects have completed all research-related interventions; and/or
 - (iii) the research remains active only for long-term follow-up of subjects
- or
- c) Where no subjects have been enrolled and no additional risks have been identified (if the protocol has had a Full Board amendment approval within the last year that has increased the risks to the participants a Full Board Continuation must be submitted) ;
- or
- d) Where the remaining research activities are limited to data analysis

All required documents must be submitted six weeks prior to the expiration date.

- Submit one copy of the Continuation Form with original signatures
- Two clean* copies of the informed consent/assent/information sheet currently in use (if applicable)
- Two clean* copies of the advertisements/notices/flyers currently in use (if applicable).

2. Full Board Review for Continuation

All required documents must be submitted six weeks prior to the expiration date.

- Submit one copy of the Continuation Form with original signature
- Two clean* copies, single sided, of the informed consent/assent/information sheet currently in use (if applicable)
- Two clean* copies of the advertisements/notices/flyers currently in use (if applicable).

AND

Submit 19 collated packets each containing:

- One copy of the Continuation Form (one packet must contain original signatures)
- One clean* copy of the informed consent/assent/information sheet currently in use (if applicable)
- One clean* copy of the advertisements/notices/flyers currently in use (if applicable).

* Without IRB Approval Stamp


Human Investigation Committee

101 East Alexandrine (313) 993-7122 Fax
 Detroit, MI 48201 (313) 577-1628 Office
www.hic.wayne.edu

Continuation Form

ALL HIC SUBMISSION FORMS MUST BE THE CURRENT VERSION (SEE HIC WEBSITE) AND TYPEWRITTEN/COMPUTER GENERATED

Section A: Principal Investigator (PI)

1.	Name of PI	Michael Klein, MD	PI's Signature	
2.	Department	Pediatric Surgery	Fax	313-966-7696
3.	Address 3901 Beaubien Blvd, 3 rd Floor Carls Bldg Children's Hospital of Michigan If any of your contact information has changed since the last IRB submission please revise the information on WSU's pipeline, if you have WSU access.		Pager	313-328-5633
			E-Mail	mklein@dmc.org
			Telephone	313-745-5840
4.	Form Completed By	Rachel Kast	Date	9/4/09
	Telephone	248-877-1404	E-mail	aw7315@wayne.edu

Section B: Protocol Information

5.	Coeus Number	0506002366
6.	HIC Protocol Number	018201MP4E
7.	Project Title	Raman Spectroscopy of Pediatric Neoplasms
8.	Expiration Date	September 15, 2009
<p>Note: If your protocol does not receive approval prior to the expiration date, no new participants can be enrolled, no data can be collected or used for research if collected during the period of non-IRB approval (lapsed approval). Refer to HIC policy "Continuation/Renewal of Protocol" http://www.hic.wayne.edu/HRPP_Manual/4-7_Continuation-Renewal_of_a_Protocol.pdf</p>		
9.	Current Source of Funding	CHM
	a. Is this a change from the time of the last approval? NOTE: If there is a change, an amendment should have been submitted. If not done, an amendment form must be submitted.	<input type="checkbox"/> Yes <input checked="" type="checkbox"/> No
10.	Is WSU the Coordinating Center for this study? If yes, complete a Coordinating Center Form and submit with this continuation	<input type="checkbox"/> Yes <input checked="" type="checkbox"/> No
11.	If research personnel will be accessing in-patient and/or out-patient medical records from WSU or affiliated sites, or from databases created from in-patient and/or out-patient medical records, has appropriate HIPAA documentation been submitted (HIPAA Summary Form and HIPAA Authorization Form-if applicable)?	<input type="checkbox"/> Yes <input type="checkbox"/> No <input checked="" type="checkbox"/> N/A

12.	<p>This question applies to the Principal Investigator only: Has any potential and/or real financial conflict of interest arisen since the last IRB review that has not yet been reported to the Financial Conflict of Interest Committee (FCOIC)?</p> <p>If "yes," a "Financial Conflict of Interest Detailed Disclosure Form" must be submitted to the FCOIC annually or when a change(s) occurs. The form and more information are available at: www.research.wayne.edu/coi. For additional information, contact the Conflict of Interest Coordinator @ 313-577-9064</p>	<input type="checkbox"/> Yes <input checked="" type="checkbox"/> No
-----	--	--

Section C: Operational Status of Project

#	Question													
13.	Has this project accrued participants (consented) and/or collected data/specimens?	<input checked="" type="checkbox"/> Yes (go to question #14) <input type="checkbox"/> No (answer question #13a)												
	a. List reason(s) for not accruing participants/data/specimens?	<input type="checkbox"/> Insufficient staff <input type="checkbox"/> Insufficient funding <input type="checkbox"/> Lack of eligible participants <input type="checkbox"/> Other (explain):												
14.	Is this protocol closed to accrual/recruitment?	<input type="checkbox"/> Yes <input checked="" type="checkbox"/> No (go to question #15)												
	a. Have all the participants completed all research related interventions*? If yes, this submission qualifies for expedited review. *(Long term follow-up without intervention is not considered research-related intervention.)	<input type="checkbox"/> Yes <input type="checkbox"/> No												
	NOTE: It is not necessary to submit copies of the informed consent/assent if the protocol is closed to accrual unless the informed consent has been changed, re-consenting of participants continues, and/or re-consenting of participants may be needed in the future.													
15.	a. Indicate the initial number of participants/data/specimens approved for recruitment at WSU or its approved sites.	60												
	b. Indicate the current number of participants/data/specimens approved for recruitment at WSU or its approved sites. NOTE: If answer in a. and b. differ, an amendment should have been submitted. Date submitted: 9/7/2006 If not done, an amendment form must be submitted	600												
	c. Indicate the number of participants consented to date at WSU or approved sites.	0												
16.	This question applies to Veterans Administration Medical Center (VAMC) research only: Indicate the cumulative number of participants enrolled in each category. (State "0" if none enrolled.)	<input checked="" type="checkbox"/> NA												
	<table border="1" style="width: 100%; border-collapse: collapse;"> <thead> <tr> <th style="width: 40%;">Vulnerable Group</th> <th style="width: 10%;">#</th> <th style="width: 40%;">Vulnerable Group</th> <th style="width: 10%;">#</th> </tr> </thead> <tbody> <tr> <td>Children</td> <td></td> <td>Pregnant Women, Fetus, Neonate</td> <td></td> </tr> <tr> <td>Mental disabled/Cognitively Impaired</td> <td></td> <td>Prisoners</td> <td></td> </tr> </tbody> </table>	Vulnerable Group	#	Vulnerable Group	#	Children		Pregnant Women, Fetus, Neonate		Mental disabled/Cognitively Impaired		Prisoners		
Vulnerable Group	#	Vulnerable Group	#											
Children		Pregnant Women, Fetus, Neonate												
Mental disabled/Cognitively Impaired		Prisoners												

#	Question								
	Non-consenting participant			Terminally Ill					
	If participants enrolled in the study could be classified as belonging to a vulnerable group, IRB approval is required. If not previously approved by the IRB, submit an amendment to request the inclusion of the vulnerable group(s) into the study.								
17.	Complete the table below regarding the cumulative number of participants (consented)/documents/specimens accrued at WSU or its approved sites since the project was initiated.								
		American Indian or Alaskan Native	Asian	Black, not of Hispanic Origin	Hispanic	White, not of Hispanic Origin	Native Hawaiian or Pacific Islander	Other or Unknown	Total
	Female								
	Male								
	Unknown							400	400
	Total							400	400
18.	Is there an equitable distribution of ethnic groups?					<input type="checkbox"/> N/A (go to #19) <input checked="" type="checkbox"/> Ethnicity data not being collected (go to #19) <input type="checkbox"/> Yes (go to #19) <input type="checkbox"/> No (answer #18 a and b)			
	a. Provide justification for the inequity.					<input type="checkbox"/> Sample size too small to judge <input type="checkbox"/> Reflects site/clinic population <input type="checkbox"/> Research on specific ethnic group(s) <input type="checkbox"/> Other, explain below:			
	b. If the inequity cannot be justified, what actions will be taken during the next year to address this issue?					<input type="checkbox"/> N/A			
19.	Is there an equitable distribution of gender?					<input type="checkbox"/> N/A (go to #20) <input checked="" type="checkbox"/> Gender data not being collected (go to #20) <input type="checkbox"/> Yes (go to #20) <input type="checkbox"/> No (answer #19a and b)			
	a. Provide justification for the inequity					<input type="checkbox"/> Sample size too small to judge <input type="checkbox"/> Reflects site/clinic population <input type="checkbox"/> Research on specific gender <input type="checkbox"/> Other, explain below:			
	b. If the inequity cannot be justified, what actions will be taken during the next year to address this issue?					<input type="checkbox"/> N/A			
20.	How many participants withdrew their consent from the study at WSU and/or approved sites?							<input type="checkbox"/> N/A <input checked="" type="checkbox"/> None	
	a. Total since initial approval?								
	b. Total since last approval?								
	c. Summarize the reasons why participants withdrew their consent to participate in the study.								

#	Question	
21.	How many participants did the PI remove from the study at WSU and/or approved sites? Some examples may be screening failures, non-compliance or lost to follow-up.	<input type="checkbox"/> N/A <input checked="" type="checkbox"/> None
	a. Since initial approval?	
	b. Since last approval?	
	c. Summarize the reasons why PI removed participants from the study.	

Section D: Study Conduct

#	Question		
22.	Please indicate all of the following protocol amendment categories that received HIC approval(s) since the inception of this study. For each of these approved amendments, provide a concise narrative summary explaining the reasons for the amendment.	<input type="checkbox"/> N/A	
	Amendment Category	Date of Approval	
	Key Personnel Additions/Deletions	9/14/06 8/29/07 6/18/08 9/18/08 2/11/09 7/7/09	Addition of Gulay Serhatkulu, Rachel (Weber) Kast, Hale Wills, and Brian Sullivan as co-investigators. Deletion of Gulay Serhatkulu and Adrien Kant as co-investigators. Removal of Daad Haddad, William Lyman, Mustafa Kabeer, Christopher Young, Vaman Naik, and Houbei Dai; Addition of Cory Stewart, Umer Khalid, Luke Reisner, Brady King, Suneetha Devpura, and David Leslie as co-investigators
	Advertisement/Notice/Flyer		
	Protocol:		
	<i>Administrative changes</i>	9/18/08	Pathology reports will be stored at Harper Hospital surgery department instead of CHM surgery dept; data will be stored on a secure online website; study co-ordinator (RK) de-identify patient information and maintain key to pathology reports
	<i>Study design</i>	9/18/08	samples will be frozen and banked for follow-up testing; samples will also be tested with a Verax Raman spectrometer
	<i>Enrollment criteria</i>		autopsy specimens can be collected to build a database of normal tissue; tissues stored in the frozen tumor bank at CHM will be eligible for study inclusion
	<i>Change in treatment</i>		

#	Question		
	Data collection methods	9/30/04 1/3/05 10/21/05 9/14/06 8/29/07 6/18/08 9/18/08	All tissue resections and biopsies will be looked at instead of just suspected neoplasms; the addition of Harper Hospital, Karmanos Cancer Institute, & Detroit Receiving Hospital as study sites for tissue collection; sample size increased to 600; addition of Children's Oncology Group as a source of blinded samples of neuroblastoma-related tissues; Karmanos Cancer Institute and Harper Hospital removed as tissue collection site.
	Risks and/or benefits		
	Other	9/30/04	Raman spectroscopy will be performed in the Department of Pathology at CHM instead of WSU department of physics
	Consent/Assent/Info Sheets		
	HIPAA Summary/Authorization		
	Investigator's Brochure/Package Insert		
	Other (i.e., data safety monitoring minutes, study on hold notification, etc.)		
23.	Has the non-English short form consent been used for this study? *Please note non-English speaking participants must have the short form used plus the long form verbally translated into their language.		<input type="checkbox"/> Yes (if yes, answer #23a.) <input checked="" type="checkbox"/> No
	a. Language used:		Number of occurrences:
24.	For Investigator-initiated studies at WSU and/or approved sites involving: <ul style="list-style-type: none"> • an IND, or • an IDE, or • studies that have received IRB approval with provision that a literature search be performed on an annual or other basis, Provide the following: (1) the most recent date that a literature search or review of the literature was completed, and (2) define the strategy of the search and how the results of the search might impact the protocol approved by the IRB. Narrative:		<input checked="" type="checkbox"/> N/A
25.	List all reportable unexpected Adverse Reactions and/or Events (Serious Adverse Event-SAE) associated with this protocol (i.e., only those that met HIC reporting guidelines) in a concise narrative including the number of separate occurrences (attach separate page if necessary). These should match the specific SAE reports submitted on the Problem Report Form on file for this protocol. Follow-up reports are not counted as a separate SAE.		<input checked="" type="checkbox"/> None

#	Question		
	Site	Current Approval Period	Period Since Initial Approval
	WSU Sites and/or approved sites	(Example only: 3episodes of septic shock, 1 seizure, 5episodes of elevated liver enzymes)	
	Non-WSU Sites		
26.	Please provide a concise narrative description that explains the relevance of all reported SAE(s) to the study intervention(s); any effect(s) on study participants; and if a change in SAE frequency, severity, and/or specificity have occurred. Please indicate if any "possibly related" events have relevance on the study intervention(s).		<input checked="" type="checkbox"/> N/A
	Narrative:		
27.	Please indicate all of the following protocol event(s) that occurred since the initiation of this study. For each of these events, provide the date(s) of occurrence and a concise narrative summary explaining the reason(s) for the incidents. These events are reported/were reported to the HIC on an Unexpected Problem Form.		
	Event:	Date of Event(s)	Concise Narrative Summary
	Audits (Internal/External)		<input checked="" type="checkbox"/> None
	Breach of Confidentiality		<input checked="" type="checkbox"/> None
	Hold Notifications		<input checked="" type="checkbox"/> None
	Period of Non-IRB Approval		<input checked="" type="checkbox"/> None
	Participant Complaints		<input checked="" type="checkbox"/> None
	Suspensions (Institutional or Sponsor)		<input checked="" type="checkbox"/> None
	Change to protocol without IRB review and/or approval		<input checked="" type="checkbox"/> None
	Unanticipated adverse device effect		<input checked="" type="checkbox"/> None
	Incarceration of a participant in the study which was not approved for prisoners		<input checked="" type="checkbox"/> None
	Violations or Deviations		<input checked="" type="checkbox"/> None
	Other		<input checked="" type="checkbox"/> None
28.	What processes are in place to prevent any of these events from reoccurring?		<input checked="" type="checkbox"/> N/A
29.	Since last approval, indicate all of the following information obtained about the study. Provide a concise narrative summary explaining the significance to the protocol.		
	Information:	Concise Narrative	
	Data safety reports pertinent to the study?		<input checked="" type="checkbox"/> None
	Change in FDA labeling or withdrawal from marketing of drug, device or biologic used in the protocol?		<input checked="" type="checkbox"/> None

#	Question		
	Reports with relevant scientific interim findings?		<input checked="" type="checkbox"/> None
	Change in the risk/benefit ratio?		<input checked="" type="checkbox"/> None
30.	Provide justification as to why this protocol should receive approval for continuation.	Protocol has not reached accrual; we are still developing a diagnostic database of Raman spectra. The database will be used when we develop a portable probe for real-time identification	
31.	Since the last IRB approval, have any publications, abstracts, and/or presentations resulted from this research protocol? If yes, attach complete copies.		<input checked="" type="checkbox"/> Yes <input type="checkbox"/> No

Section E: Progress Report:

32.	<p>Attach a complete and concise updated progress report of the research project--in non-technical language (lay terms). Information provided is intended to give all members of the IRB (scientists and non-scientists) a clear understanding of the research study to-date. The narrative summary should contain the following information:</p> <ul style="list-style-type: none"> • The current goals/aims/hypothesis of the study • A brief description of methods/procedures of the study • A brief summary of progress of the study
-----	--

APPENDIX B RAMAN SPECTROSCOPY DATA PROCESSING

Preprocessing Data (may apply to cancer data only)

1. Put all the data files in the same folder.
2. Put a copy of adaptminmax#####.m, combinespectra#####.m, and meanspectraplot.m into the same folder
3. Open Matlab
4. Click [...] button next to the 'current directory' field and browse to select the folder your data is in
5. Type 'dir' into the command window to get a list of all the files in the folder
6. Highlight the filelist and press ctrl+c to copy the list (See Rachel for the secret trick if your filelist is longer than the command window in Matlab)
7. Open the notepad program and press ctrl+v to paste the list
8. Go through the list and delete any items which are not file names. If non-spectral files are included, you will get an error when you try to process the data
9. Save the file as 'filelist.txt'
10. In the Matlab command window, type 'adaptminmax#####' and press enter to run the preprocessing program
11. You will be asked if you want to see the graphs. Type '1' for yes and press enter
12. The processing program will begin preprocessing. For each file, a new graph will open which shows the original data and background subtraction on the top, and the processed spectrum on the top.
13. Relax for 10 minutes or so while the computer processes. The program is setup to pause after it processes 100 files. Sit back until you get to a pause.

14. One-by-one, look at each spectrum to see if it looks decent, and then close each window. Write down a list of all the files which look bad as you do this. Possible reasons for exclusion include: spectrum of glass or stainless steel, cosmic rays which were not removed, measurement which was stopped mid-way, etc
15. Save this list for later.
16. Once you've gone through all the files, you will be back at the Matlab command window. It will say 'Press any key to continue'.
17. Press any key to continue (pretty self explanatory, I know)
18. Repeat steps l-q until all your files are preprocessed
19. Once a file is preprocessed, the code 'amm-' is appended to the file. That is how you can identify processed data. You will also notice that map files which had many points are now separated into individual processed files.

Combine all the individual files into one mega-file

20. Open windows explorer and navigate to the folder where your data is stored
21. Copy all of your original data into a new subfolder (I suggest naming the folder 'Original' or 'Original Data' or something similar, for easy identification if you need it later). You won't need it anymore for data processing
22. Remember that list you made with all the bad files? It's time to get rid of them so they aren't included in the analysis. Go through and delete all of those bad boys. Make sure you're deleting the processed files (with 'amm-') and not the original files
23. Go back to Matlab and type 'dir' into the command window to get a list of all the files in the folder

24. Highlight the filelist and press ctrl+c to copy the list (See Rachel for the secret trick if your filelist is longer than the command window in Matlab)
25. Open the notepad program and press ctrl+v to paste the list
26. Go through the list and delete any items which are not file names. If non-spectral files are included, you will get an error when you try to combine the data into one file. Make sure that you are looking only at processed files. You don't want any original files included in the filelist.
27. Save the file as 'filelist.txt'
28. Go back to Matlab again (we're almost done in Matlab, I promise!) and type in 'combinespectra#####'
29. You will be asked if you want to create separate files or one big file. For now, we want to make one big file so we can import all the data into SPSS at once. Type 'b' and press enter.
30. The command window will say 'filelist.txt has ### files', then it will work for a couple minutes to create the file. It is done when you get a message which says 'allspectra.txt being created'.

Import Data Into SPSS and Setup your data

31. Open SPSS.
32. If the intro window pops up, press Cancel.
33. Select File/Read Text Data
34. In the browser that pops up, navigate to your data folder, and select 'allspectra.txt', then press 'open'
35. You will then go through a wizard system to help you import the data.

- a. In Step 1, select 'No', then press the Next button
- b. In step 2, select 'yes' for 'Are variable names included at the top of your file?'
- c. In step 3, press the Next button – the defaults are all ok here
- d. In step 4, un-select 'Space' as a delimiter and press Next
- e. In step 5, you will get an error that the file names are not an appropriate format. Press ok, then next
- f. In step 6, press finish to complete the import process

36. If you are trying to append new data to an existing SPSS file, there are many more steps. For now, see Rachel. Full notes will be written later

37. SPSS has 2 views you can look at. You switch between the views by choosing the 'Data View' tab or the 'Variable View' tab at the bottom. The data view tab is just like an Excel spreadsheet. Each row represents a single case, and each column represents a variable. The variable view tab is where you can add variables, change their format, etc. In this view, each row represents a variable, and the different columns represent different parameters for those variables. We need to add in more variables such as the filename, diagnosis, etc before we can classify data. Right now the only variables in SPSS are the peak intensities at each wavenumber.

38. To add variables, go to the variable view tab. Right click on row 1 and select "Insert Variable".

- a. Create a filename variable. Double click in the name column to change the variable name to 'filename'. Click on the 'Type' for the variable and a [...] button will appear. Click on that. In the 'Variable Type' window that pops up, select 'String'. In the 'Characters' tab, delete the 8 and put a more

reasonable number – think about how long your filenames would be – I recommend a nice large number like 100.

- b. Create a variable for tissue/cell/bacteria/etc type. Again, right click on row 1 and select “insert variable”. Double click in the name column to change the variable name to whatever is suitable for your data. This time, we will leave the variable type as ‘numeric’. Change the ‘decimals’ field for the variable to ‘0’. This just makes your data look prettier. Click on the field in the ‘values’ tab, then click the [...] button. This lets you make a key so that your numeric variable correlates to a text value. The text values will appear in the analysis output in your results. The value field will be a number (use consecutive numbers) and the label field will be the string value. For example,

1	neuroblastoma
2	ganglioneuroma
3	normal adrenal gland

- c. Create any other variables that are necessary for your analysis.

39. Now you have to enter in the information about each of your files!

40. Open notepad, and open the filelist.txt file. Use ctrl+a to select the whole filelist, then ctrl+c to copy it

41. Go to the data view tab in SPSS

42. Highlight the filelist column and press ctrl+v to paste the filelist. Now you don’t have to enter all the filenames manually!

43. Go through the rest of your columns/variables and fill in the information. (Hint: copy & paste speed this process up a lot)

Process Data

When you open SPSS, there are 2 windows. The first window is your data window (which has the data view tab and your variable view tab). The second window is the output tab. When you do analysis, the results will be shown in the output window.

For analysis in SPSS, there are approximately 1.3 gazillion ways you can analyze your data. I will explain how to do 2 essential methods: Principal Component Analysis (PCA) and Discriminant Function Analysis (DFA). PCA compresses the variability of your data set from many hundred variables to 5-20 really essential ones. It is up to you whether you want to perform PCA before doing DFA. If you want to look at the significance of your actual peaks, it's better to just run DFA. If you want to compress your data into a smaller set and then perform analysis, use PCA. DFA is the classification method. You have 3 methods for training: **(1)** do the classification based on all the data. This method has no validation and is not recommended. **(2)** Perform a leave-one-out analysis. In this method, a single spectrum is removed from the data set. DFA is performed on the remaining (n-1) files, and then the classification is applied to the single point. Then, another single spectrum is removed from the dataset and classification is performed again. This process repeats over and over until it has been performed for each point. If you have a reasonably sized data set, the changes to the PCA structure are so minimal that you do not need to do leave-one-out analysis on the PCA. **(3)** Test/Train grouping. In this method, you split your data in half into a testing group and a training group. You would create a placeholder variable (as described earlier) – for instance, '1' could represent training group, and '0' could represent the testing group. You would perform PCA (if desired) and DFA on the training group to

build your model, and then test it with the training group. You could then switch, and make the training group the test group and vice versa.

Selecting Cases for Analysis

Let's say that you have three groups in your data set, but only want to compare groups 2 & 3. In that case, we need to temporarily eliminate group 1 from the data set.

44. Select Data/Select Cases from the menu

45. In the Select area, choose "if condition is satisfied", then press the "if" button

46. In the pop up window, you will put in logic code to choose the cases you want to

KEEP. You can automatically move variable names from the left window, or you can manually type them in. The logic buttons are below. The & means 'and'. The | means 'or'. Make sure to use proper parenthesis if you are using complicated logic.

47. For example, if you wanted to select groups 2 & 3 as described above, you could type either of the following:

`(Group=2) | (Group = 3)`

`Group = (2 | 3)`

48. For a more complicated example, suppose you want to look at 2 groups, where group a is fresh, untreated tumors and group b is frozen, treated, normal tissues.

You might use the following code:

`((Treatment = 1) & (Temp = 1) & (Tumor = 1)) | ((Treatment = 0) & (Temp = 0) & (Tumor = 0))`

49. When you are satisfied with your selection press the 'continue' button, and then press the 'ok' button.

50. You should check your data before proceeding to make sure you selected the correct cases. All of the cases which are temporarily excluded will have a diagonal line through their case number on the left hand side of the data window.

Performing Principal Component Analysis

51. From the data window or the output window, select Analyze/Dimension Reduction/Factor

52. In the left hand column, select all of the Raman peak variables (you can hold down the shift key and use the mouse to quickly scroll through the list). Press the right-facing arrow button to move them to the variables column. These are the variables which will be used for analysis. If you don't want to use all the variables, only select the ones you want.

53. If you only want to do PCA on a specific group such as a training group, (it will be applied to everything else automatically) select the variable for the desired group, and use the bottom right-facing arrow to move it to the selection variable field. Click on the value button. In the pop-up box, enter the value you wish to use for the training group.

54. Press the extraction button. In the 'analyze' area, select 'covariance matrix' (instead of correlation matrix) then press continue.

55. Press the 'scores' button and select 'save as variables'. Then press continue.

56. Press 'ok' to run the analysis

Reviewing Principal Component Analysis Results

57. The results will show in the output window.

58. Principal components with an eigenvalue $> 1 \times$ the mean eigenvalue are saved.

59. The 'Total Variance Explained Table' shows you how many Principal components were saved. The 2 right hand columns are the important ones. They show how much variance is explained by each principal component individually and cumulatively.
60. The 'Component Matrix' table shows the weighting factors of each variable for each component. This would be important if you wanted to determine which chemicals are represented in each PC. For instance, you could do further testing to examine how diagnostic each PC is, then determine which chemicals are diagnostic. You're probably better off just doing this with DFA results though.

Discriminant Function Analysis

61. From the data window or the output window, select Analyze/Classify/Discriminant
62. In the left hand column, select the variable which you are classifying, and use the top blue arrow to move it to the 'grouping variable' field. Press the 'define range' button and enter the minimum and maximum values for your classification variable. If you have 2 groups, this might be 1, 2; three groups would be 1, 3, etc
63. In the left hand column, select all of the Raman peak variables (you can hold down the shift key and use the mouse to quickly scroll through the list). Press the middle arrow button to move them to the 'independents' column. These are the variables which will be used for analysis. If you don't want to use all the variables, only select the ones you want.
64. Press the 'Classify' button. In the 'display window, select the following
- 'casewise results': this will show you case-by-case results in a huge table. If you want to examine misclassified cases, you will need this table

- b. 'summary table': this will give you overall classification percentages. If you have 2 groups (cancer/normal), it is like sensitivity and specificity. If you do leave-one-out analysis or test/train analysis, the table will be twice as long, with original classification (no special training) on top, and the leave one out or test/train analysis on the bottom. *Make sure you are careful which half you look at when writing your results.*

65. If you think you might want to access your results later or make a pretty plot, press the save button and check the 'discriminant scores' box. Then press continue.

66. Setup the specific training parameters you wish to use

- a. If you don't want to do any special training, no extra steps are necessary.
- b. If you are doing **train/test analysis**, select the associated variable in the left hand column, and use the bottom blue area to move that variable to the 'Selection Variable' field.
- c. If you are doing **leave-one-out analysis**, press the 'classify' button. In the 'display' area, check 'leave one out classification' then press continue. Click on the value button. In the pop-up box, enter the value you wish to use for the training group.

67. Press 'ok' to run the analysis

Reviewing Discriminant Function Analysis Results

68. The results will show in the output window.

69. The number of discriminant functions/standardized canonical discriminant functions will be 1 less than the number of classification groups. (if you have normal/cancer

there will be $2-1=1$ group, if you have normal/benign/cancer, there will be $3-1=2$ groups).

70. The 'standardized canonical discriminant functions' and 'structure matrix' tables can show which Raman peaks are significant for each discriminant function. Use these if you want to determine which peaks have diagnostic capability.
71. The casewise statistics table shows you all of your misclassifications. Cases marked with * were misclassified. The actual group column shows how you entered the classification in SPSS (this would be the gold standard). The predicted group column shows the group that the data is placed into based on DFA (not the gold standard). If you look at the case number, you can go to that row in the data table to see which file is misclassified.
72. The classification results table shows how many cases were diagnosed to each group with actual number of cases classified and percentage classified. Special training methods (test/train or leave-one-out) are shown below the overall results (even if you don't want overall results, SPSS gives them to you anyway). *Make sure you are careful which half you look at when writing your results.*
73. Lots of other really cool statistics can be done with DFA, but we'll leave it at that for now. If you want to learn more, take PSY8150.
74. To create a plot of the DFA results, select Graphs/Legacy Dialogues/Scatter/Dot. Select the simple scatter or the 3-D scatter option. Scroll down to the bottom of your left hand list until you see the saved discriminant function scores (I hope you remembered to save them when you ran the analysis). Choose the variables you want, and move them to the x, y, and z (if applicable) –axis fields. At the top of the

left hand field list, select the classification variable, and move it to the 'Set markers by' field. This will make it so each case is labeled by its 'gold standard' diagnosis and you can easily see how well your classification separated the data. You can also do this with PCA values. I'll let you try to figure this out if you want.

- a. Note – remember the number of discriminant functions created is 1 less than the number of classification groups. Therefore, if you only have 2 classification groups, you'll only have 1 discriminant function. Therefore, you can only make a 1-D scatter plot.

Excluding/changing data points

75. Once misclassified cases are identified, go back to the raw data to look for reasons why. Review the raw data text file to see if there is anything unusual. If it seems ok, go back to your original sample (if possible). Review the slide or other available information to look for explanations for the misclassification.
76. If you find that you have to delete a case or change its diagnosis, you must update the SPSS data table, then re-do your analysis, starting with PCA if applicable.

Creating mean spectra figure files (In Matlab)

77. If you didn't already do step 1, make sure all the data files are in the same folder, with a copy of MeanSpectraPlot.m.
78. Open Matlab
79. Click [...] button next to the 'current directory' field and browse to select the folder your data is in
80. Open SPSS or excel to get a list of your files and their classifications.

81. Copy the list of filenames for the group whose mean spectrum you would like to calculate
82. Paste the list into WordPad or similar program and save the file as graphfilelist.txt
83. In the Matlab command window, type meanspectraplot then press the enter key to run the program.
84. At the prompt, type 2 (All the files) and press enter
85. The program will work for awhile and you'll be prompted to select the type of plot you want to see. To see the mean spectrum plot, select 5.
86. Repeat the same steps (75-80) for each group you'd like to calculate a mean spectrum plot for.
87. To edit a plot, click on the arrow button of the toolbar icon menu in the plot window. Then, if you double click on plot characteristics, a pop-up edit window will appear, or you can edit the text as well. If you don't like this way, you can programmatically change plot options as well, but we won't get into that here.
88. This program, as you can see, has lots of other options that you can utilize. If you want to calculate a difference spectrum (between 2 groups only) or plot multiple mean spectra on the same plot (no limit on how many groups allowed), your text file must also include group assignments. To make the group assignments, you need to copy 2 columns into the graphfilelist.txt file. The left column should be the filename and the right column should be the group number. It's easier to arrange your columns this way in Excel or SPSS, then copy to WordPad.

APPENDIX C CELL CULTURING SOP

Materials

- Trypsin (see specific cell line notes for exact type)
- Medium (see specific cell line notes for exact type)
- Dulbecco's Phosphate Buffered Saline (PBS)
- Flasks
- Pipetter and pipettes (1cc, 2cc, 5cc, 10cc, 25cc)
- Alcohol and kimwipes/clean room paper
- Bleach in a beaker
- Centrifuge tubes (when splitting adherent cells or testing cells with Raman)
- UV-quartz slide (when testing with Raman)

General Cell Culture Notes

- Media is added to flask containing trypsin because the media neutralizes the trypsin
- Generally cells are split every other day
 - Fast growers are generally split → 1:3 (1 initial flask + 2 new flask)
 - Slow growers are generally split → 1:2 (1 initial flask + 1 new flask)
 - It's important to passage to prevent overgrowth, nutrient depletion, & contamination.
- *Generally with trypsin one wants to use as little as possible & allow to sit on cells for as little time as possible.* The time varies by cell line. See cell line specific notes for more information.
- Avoid touching the neck of the flask and the back (cell side) of the flask with the pipetter. This will avoid contamination and prevent you from damaging the cells

- When pipetting, pay close attention to both the flask and the pipetter. Make sure not to suck liquids to the level of the cotton in the flask. This keeps the pipetter from being contaminated.
- Media and trypsin can become bad if they are old or are over-heated/heated too long in the incubator
- Once a pipette has been in the flask or other contaminated either, it should not go in the sterile fluid containers (media, PBS, trypsin, etc)
- Wear gloves, and avoid touching any exposed skin while wearing gloves
- Wash hands after working with cells
- Complete medium should not be left in the fridge >3 weeks.

Mixing Cell Media

Start with a 500 mL bottle of cell medium. Then add:

- 50 mL fetal bovine/calf serum
- 5 mL L glutamine
- 5 mL antibiotic (we used a mix of 2 antibiotics and 1 antifungal)

Place the lid back on the medium and shake by hand to mix. Label the container with initials, date, and what you added. With the above additions to the media the media is referred to as complete media.

Defrosting Cells

1. Move cells from the -150C freezer to the -80 freezer (all our cells are currently in the -80C freezer)
2. Prep the hood area by spraying with 75% alcohol

3. Start with a new flask (spray flask or flask bag with alcohol before bringing under hood)
4. Label the flask with your initials, the date, the cell line, and any other pertinent information
5. Add 11 mL of complete medium to the flask
6. Prepare the area for transferring the cells.
 - a. Leave the flask lid loose
 - b. Place a 2mL pipette on the pipetter (leave the paper wrapping on)
7. Move the cells from the -80 freezer to the 37 bath.
8. Wait about 90 seconds or until there is a small, pea-sized ice still remaining. For most cell lines, you want to spin the flask between your fingers while defrosting, without letting the neck of the flask touch the water. See specific cell-line notes for more instructions.
9. Spray the cell vial and your hands with 75% alcohol and wipe down with a Kimwipe/clean room paper.
10. Open the cell cryovial (place the lid face-up in the hood if necessary)
11. Use the 1cc pipette to suck out the cells from the flask
12. Empty the pipette into the flask (put the pipette tip all the way into the medium fluid and then empty)
13. Mix a couple of times to rinse out the pipette
14. Suck out about 0.5 mL of the cell/medium mixture
15. Use this to rinse out the cryovial a couple of times
16. Suck the 0.5 mL out of the vial and replace it in the flask.

17. Mix a couple more times.
18. Replace the lid on the flask (tightly)
19. Discard the pipette
20. Place the flask under the microscope and double-check your cells
21. Place the flask in the 37C incubator
22. Put some bleach in the vial to kill the cells (since we are working with human cells).
 Allow the bleach mixture to sit for at least 5 minutes, then you can pour the bleach mixture down the drain (dilute with running water)
23. Clean the working area by spraying with 75% alcohol

Cell Passage (Splitting): Adherent Cells

1. Remove complete media and trypsin from refrigerator & warm (RT – 37 °C, takes 20 – 30 minutes)
While complete media & trypsin are warming, steps 2-5 may be performed
2. Prep the hood area by spraying with 75% alcohol and wiping down. Put the other necessary supplies under the hood too (pipetter, pipettes, PBS, bleach, etc) and put the biohazard bag close to your work area
3. Start with a new flask (spray flask or flask bag with alcohol before bringing under hood)
4. Label T-75 flask w/cell line (i.e. 2774), date, initials, and split ratio (i.e. 1:3). Label both the front and the bottom of the flask.
5. While media warming, check cell growth under the microscope to determine its confluence.
 - a. Generally, cells should be split ~ 70% confluence.

b. If media is not ready, place cells back into the incubator

When complete media & trypsin are warmed, continue below

6. Use a 10 cc pipette to suck out the media, and discard in the bleach container
7. Add 5 – 8 ml Dulbecco's PBS to flask. (*Add to front wall, side of flask w/o attached cells.*)
8. Re-cap & then rock/roll flask side-to-side w/fluid touching attached cells. (*Don't let fluid enter cap.*)
9. Remove PBS and discard in bleach container
10. Some cell lines need to be rinsed with PBS 2-3 times (generally cancer cells). See cell-line specific notes.
11. Add ~3 ml trypsin to the attached cells and then rock side-to-side. Generally, cancer cells need to be placed in the 37C incubator for ~5min for the trypsin to act, whereas normal cells can sit under the hood 2-3 min. See cell-line specific notes.
12. You can look at the back wall of the flask or look under the microscope to verify that the cells are detaching.
13. Add 7 ml of media to back wall of flask to deactivate the trypsin & continue to wash back of wall (power wash) until cells come off.
14. Break up cell clumps. You can suck up all the media into the pipette, place it against the bottom of flask and push out the cells, or you can release the cells against the corner of the flask to break clumps. Check with microscope if desired.
15. When splitting cells in the T-75 flask, 12 ml of fluid need to be in each flask. There should be 10cc of liquid in the flask currently (3 trypsin, 7 media). Determine the

amount of fluid you need to add to get to the right concentration (add 14 cc media to make 2 flasks/24 cc, 26 cc media to make 3 flasks/36 cc, etc).

16. Add the proper amount of media you just figured out and mix. (Go up and down with the pipette several times)
17. Place 12 ccs of media/cells in each flask and cap your flasks. Check with microscope if desired.
18. Place flasks in incubator
19. Clean hood and everything left in hood with the 75% alcohol. After cells have been in bleach for at least 5 min, they can be poured down the sink (dilute with running water)

Freezing Cells

Cells Should be split ~1 day prior to freezing. They should be at approximately 80-90% confluence when splitting.

1. Warm up media and trypsin
2. Sterilize hood with 70% EtOH
3. Prepare all necessary materials, wipe everything with 70% ethanol
4. Check cells for confluence & contamination
5. Remove media from flask
6. Rinse with 5-7 cc PBS (add to front wall)
7. Remove PBS
8. Add 3 mL trypsin (see cell notes for which type) to back wall, cover bottom, incubate as described in cell-specific notes

9. Add 7cc fresh media to resuspend. Power wash back wall to detach all cells, break up any clumps
10. Put media/trypsin/cell into centrifuge tube and spin at 700 RPM for 5 min
11. Bleach flask while waiting
12. Warm up freezing media and prepare cryovials with labels
13. Use 1mL or 2mL pipette to remove media from centrifuge tube. Near the bottom, tilt the tube to remove fluid rather than putting the pipette near the cell pellet.
14. Resuspend in PBS to wash away any remaining medium. Break up any clumps.
15. Centrifuge at 1200 RPM for 5 min
16. Remove PBS from centrifuge tube (remember to tilt the tube)
17. Add 1 mL of freezing media for each flask you wish to make.
18. Put 1 mL of media in each cryovial. Do not put bubbles in. It is ok to have slightly less than 1 mL.
19. Place in Mr. Frosty in -80.
20. Remove from Mr. Frosty the next day and place in -150 freezer if available

Testing Cells with Raman Spectroscopy

In the clean room:

1. Remove cells from flask (trypsinize if necessary) and place in centrifuge tube
2. Spin down at 700 RPM for 5 min
3. Remove media with 1mL or 2mL pipette and discard in bleach container. Tilt tube when you get to the bottom rather than putting pipette near the cell pellet.
4. Resuspend cells in PBS and re-spin at 700 RPM for 5 min (this will make sure the cells are thoroughly rinsed)

5. Remove media with 1mL or 2mL pipette and discard in bleach container. Tilt tube when you get to the bottom rather than putting pipette near the cell pellet.
6. Resuspend in 1-2 mL of PBS and place cells in a cryovial

In 3322:

1. Turn on the live-cell chamber and place the cryovial in the chamber so it stays warm.
2. Turn on and calibrate the Raman if it isn't already ready
3. Put the Nikon 60x dipping objective on the microscope
4. When the Raman is ready, move the cells under the hood, and place 150 uL on the end of a clean UV-quartz slide.
5. Carefully bring the slide over to the Raman. Put the remaining cells back in the live cell chamber.
6. Place the slide on the stage, with the cell end hanging over the edge.
7. Raise the stage until the objective contacts the liquid
8. Adjust the stage to focus on a cell
9. *Carefully close the door to the Raman and switch the laser on.
10. Ensure the laser is properly focused and begin the measurement
11. The parameters we use are:
 - a. 10 accumulations
 - b. 10 seconds each
 - c. 50% power
 - d. Check cosmic ray removal
 - e. Check 'close shutter after measurement'

f. 600-1800 cm⁻¹

The filename should include this information, as well as the cell type (note if suspended in PBS), the date, and which measurements came from each cell (A1, A2, B1, B2, etc)

APPENDIX D PCR PROCEDURES AND RESULTS

RNA Isolation

Total RNA was isolated using the RNeasy Protect Mini Kit (Qiagen), adding the optional step to perform DNase I digestion. Briefly, cells were stored at 4°C in PBS until RNA isolation. Cells were lysed using Buffer RLT, then homogenized using a QIAshredder spin column. The RNA was bound to the RNA column, treated with DNaseI to remove genomic DNA, washed, eluted with RNAase-free water, and stored at -80°C.

cDNA Generation

Prior to cDNA generation, the concentration of total RNA in each sample was measured using the NanoDrop spectrometer (Thermo Fisher Scientific, Wilmington, DE). 1 µL of sample was pipetted onto the measurement surface, and the arm was closed, creating a bubble between the arm and measurement surface. The height of the bubble was automatically adjusted for the wavelength of light, and the quantity of RNA in the sample was determined. The NanoDrop was cleaned with lens paper between each sample measurement.

NanoDrop also provided information about the quality of RNA, and whether it had protein contamination. Protein is generally more absorbent at 280 nm whereas nucleic acids have higher absorbance at 260 nm. In general, a 260/280 absorbance ratio of 2.0 represents a pure RNA sample. Lower values mean the sample may be contaminated by protein or other chemicals ("NanoDrop Technical Support Bulletin T009," 2007). Table D.1 shows the RNA concentrations and 260/280 ratio for each sample.

Sample Number	RNA concentration (ng/uL)	260/280 ratio
MYCN3-B-120809	236.28	2.13
MYCN3-L-120909	585.29	2.12
MYCN3-K-120909	297.78	2.07
MCYN3-M-121009	34.40	2.6
MYCN3-Q-121109	1641.42	2.08
MYCN3-P-121109	1388.21	2.11

Table D.1: Relative concentration of RNA and 260/280 ratio for each sample.

As Table D.1 shows, sample M had an exceptionally low concentration of RNA. It was removed from the study.

cDNA was created following RNA quantification. Ready-To-Go You-Prime First-Strand Beads (GE Healthcare) with random hexamers (Integrated DNA Technologies, Coralville, IA) were used to create the cDNA. RNA was added to the You-Prime First-Strand Bead tubes at a concentration of 2 µg/ 30 µL. The initial concentration of RNA detected using the NanoDrop was converted to µg/µL, and then entered into the formula

$$\text{volume sample RNA} = (2 \mu\text{g} * 1 \mu\text{L}) / \text{concentration}$$

to determine the volume of sample necessary to reach 2 µg. Then, the volume of water necessary to reach the 30 µL volume was calculated using the formula

$$\text{volume water} = 30 \mu\text{L} - \text{volume sample RNA.}$$

Table D.2 shows the volumes of sample RNA and water used for each sample.

Sample ID	Initial RNA (ng/µL) Concentration	Convert to µg/µL	µL RNA to get 2 µg RNA	µL water to reach 30 µL
MYCN3-B-120809	236.28	0.2363	8.4638	21.5362
MYCN3-L-120909	213.43	0.5853	3.4171	26.5829
MYCN3-K-120909	297.78	0.2978	6.7159	23.2841
MCYN3-M-121009	34.40	Excluded	Excluded	Excluded
MYCN3-Q-121109	1641.42	1.6414	1.2185	28.7815
MYCN3-P-121109	1388.21	1.3882	1.4407	28.5593

Table D.2: Calculations for each sample to determine the concentration of RNA and water needed to initiate cDNA generation

Next, 2 µg of random hexamer diluted in 3 µL RNA-free water was added to each tube. We started with 10 nm (nanomoles) of dry random hexamer at a molar concentration of 5581.3 pm (picomoles) / 10 µg and calculated that our total weight of hexamer of 18.18 µg. We diluted the dry random hexamer in 90.9 µL of RNA-free water to get a final concentration of 0.2 µg/ µL water ((18.18 µg*1 µL)/0.2 µg). Using this dilution, we can be sure that each 1 µL of water contains exactly 0.2 µg of random hexamers. A large quantity of random hexamer equal to the volume necessary for 13 samples was mixed using 13 µL of random hexamer and 26 µL of RNA-free water. Then, 3 µL volumes were pipetted from this mixture to each sample tube. One extra sample was made in case of pipette errors.

Once the sample tubes were all prepared, they were gently vortexed and briefly centrifuged to mix the sample and move it to the bottom of the tube. Tubes were incubated at 37°C for 60 minutes while the cDNA reaction occurred. After the reaction, cDNA samples were stored at -20C until PCR measurement.

PCR

PCR was performed using a MYCN TaqMan gene expression assay with a FAM marker (Applied Biosystems) to quantitate the level of MYCN in our cells. We also used a probe to measure the GAPDH housekeeping gene marked with a JOE tag as a control (Applied Biosystems). Housekeeping genes are found at the same expression level in all cells; therefore, they should provide a constant expression value in all samples.

The MYCN probe was supplied at an 18µM concentration for primers and 5µM concentration for the probes, totaling a 20X concentration. The GAPDH probe was

supplied with a 10 μ M forward primer, a 10 μ M reverse primer, and a 5 μ M probe. TaqMan $\text{\textcircled{R}}$ Universal PCR Master Mix at a 2x concentration (Invitrogen) was used for the reaction.

The MYCN gene expression assay was specially designed to simplify the PCR chemistry. Each 20 μ L reaction was composed of 10 μ L of master mix, 1 μ L of primer (at 20x concentration), and 9 μ L of water containing the cDNA.

The GAPDH gene expression assay was designed such that each 20 μ L reaction was composed of 10 μ L of master mix, 2 μ L of forward primer, 2 μ L of reverse primer, 2 μ L of the probe, and 4 μ L of water containing the cDNA.

Each sample was tested in duplicate for each gene (MYCN and GAPDH) at two different concentrations (100 ng/reaction and 10 ng/reaction). A negative control (NTC) containing no DNA was also tested for each gene of interest in duplicate. Tests were performed in duplicate to ensure there was no sample contamination. Singleplex PCR was used because it requires less setup and calibration than multiplex PCR.

In order to minimize the number of pipetting steps, the following procedure was followed:

- Determine the number of reactions necessary (5 samples * 2 genes * 2 replications * 2 concentrations) + (1 NTC * 2 genes * 2 replications) = 44 reactions; for each gene, this are 22 reactions.
- Allow for a 10% pipette error, and adjust the number of reactions mixed accordingly. For each gene, allow for 22 reactions + 2 pipette error reactions = 24 total reactions.
- Determine which combination of reaction components for each gene can be combined to pipette in one step

- All ingredients are the same for each gene tested except the cDNA plus water ingredients – the cDNA material must be pipette individually for each sample
- The smallest amount of water needed in a reaction is 4 μL using the GAPDH probe.
 - The GAPDH reaction mix should contain 10 μL of master mix, 2 μL of forward primer, 2 μL of reverse primer, and 2 μL of probe for each reaction
 - The MYCN reaction mix should contain 10 μL of master mix, 1 μL of primer, and (9 μL – 4 μL) 5 μL of water for each reaction
- Combine the ingredients determined in the previous step, making enough material for all reactions for each gene
 - For GAPDH, combine in a single tube
 - 10 μL * 24 reactions = 240 μL of master mix
 - 2 μL * 24 reactions = 48 μL of forward primer
 - 2 μL * 24 reactions = 48 μL of reverse primer
 - 2 μL * 24 reactions = 48 μL of GAPDH probe
 - For MYCN, combine in a single tube
 - 10 μL * 24 reactions = 240 μL of master mix
 - 1 μL * 24 reactions = 24 μL of primer
 - 5 μL * 24 reactions = 120 μL of water
- Pipette 16 μL of the GAPDH mixture into each well designated for GAPDH testing. The same pipette tip can be used for the entire process, as long as it does not get contaminated.

- Pipette 16 μL of the MYCN mixture into each well designated for MYCN testing. The same pipette tip can be used for the entire process, as long as it does not get contaminated.
- Determine the volume of water and cDNA necessary to reach concentrations of 100ng cDNA / 4 μL water.
 - cDNA was created at a concentration of 2 μg / 33 μL . This is equivalent to 60.6 ng / μL .
 - Prepare enough material to have 1 extra reaction. Therefore, there should be at least 5 reactions made for each sample (2 reactions for MYCN, 2 reactions for GAPDH, and 1 extra for each sample)
 - The volume of cDNA necessary for 500 ng is $500 \text{ ng} / (60.6 \text{ ng} / \mu\text{L}) = 8.25 \mu\text{L}$
 - The volume of water required to reach the final volume of 20 μL is $20 \mu\text{L} - 8.25 \mu\text{L} = 11.75 \mu\text{L}$.
- Determine the volume of water and cDNA necessary to reach concentrations of 10ng cDNA / 4 μL water.
 - The smallest reliable pipette volume is 1 μL , or 60.6 ng. Therefore, make enough material for 6 reactions. ($60 \text{ ng} / 6 \text{ reactions} = 10 \text{ ng} / \text{reaction}$)
 - The remaining volume of water necessary to reach the volume of 24 μL (6 reactions * 4 μL) is $24 \mu\text{L} - 1 \mu\text{L} = 23 \mu\text{L}$.
- Create a 100 ng / reaction mixture and a 10 ng / reaction mixture for every sample using the volumes listed above.
- For each sample, pipette 4 μL of the appropriate mix into the appropriate well. To avoid contamination, use a new pipette tip for each well.

- Add 4 μL of water to the NTC wells of the plate. Since these are control wells, there should be no genetic material in the well.

The end result is a well plate where every test well is filled to the same volume of 20 μL . The layout of the 96-well plate is shown below in Figure D.1.

		MYCN 100ng	MYCN 100ng	MYCN 10ng	MYCN 10ng	GAPDH 100ng	GAPDH 100ng	GAPDH 10ng	GAPDH 10ng				
		1	2	3	4	5	6	7	8	9	10	11	12
Sample B	A												
Sample L	B												
Sample K	C												
Sample P	D												
Sample Q	E												
	F	NTC	NTC		NTC	NTC							
	G												
	H												

Figure D.1: Layout of 96-well plate for PCR

Once the well plate was set up, it was sealed with parafilm, making sure each well was individually sealed. The tray was vortexed to ensure there were no air bubbles, and to ensure that the whole sample volume was at the bottom of the well plate. Next, the plate was centrifuged for 2 minutes at 400 rpm.

Real-time PCR was performed using a 7900HT Real-Time PCR system (Applied Biosystems). The well plate was placed in the robot, and the software was setup to identify the detector (gene target: MYCN or GAPDH) and reporter (dye: JOE or FAM) in each well plate. Wells with no sample included were also identified. Finally, the standard thermal cycle protocol was selected and PCR was initiated.

PCR Results

Figure D.2 shows the amplification curves for samples B, K, and L at 100 ng cDNA concentration. Note that within each sample, the lines run very close to each other and in parallel. This signals consistent results within each sample.

Table D.3 shows the output quantitative PCR results for the experiment. The MYCN Ct value of each sample was correlated to the GAPDH Ct value of the same sample. This ensured that even if the concentration of sample within the well is off, the data analysis results will still be conclusive. In the table below, results are shown relative to the PCR concentration of 100ng of sample K.

#	Sample	Avg Ct	Avg Δ Ct	Δ Ct SE	Delta Delta Ct SD	RQ	RQ Min	RQ Max
1	100ng B	22.522	5.141	0.236	-1.554	2.937	0.579	14.901
2	100ng K	22.836	6.695	0.185	0	1	0.281	3.562
3	100ng L	20.891	3.126	0.167	-3.569	11.868	3.773	37.333
4	100ng P	23.891	5.214	0.937	-1.481	2.791	0.004	1757.162
5	100ng Q	25.396	5.868		-0.827	1.774		
6	10ng B	25.692	2.905	1.446	-3.79	13.828	0.001	288934.5
7	10ng K	27.376	6.168	3.693	-0.527	1.441	0	1.55E+11
8	10ng L	24.087	-0.909	2.781	-7.604	194.524	0	3.96E+10
9	10ng P	24.774	-0.472	1.62	-7.167	143.667	0.002	9922547
10	10ng Q	29.264	5.019	3.659	-1.676	3.196	0	2.73E+11
11	NTC MYCN							

Table D.3: Relative quantification PCR results, calibrated to 100ng sample K and the GAPDH housekeeping gene.

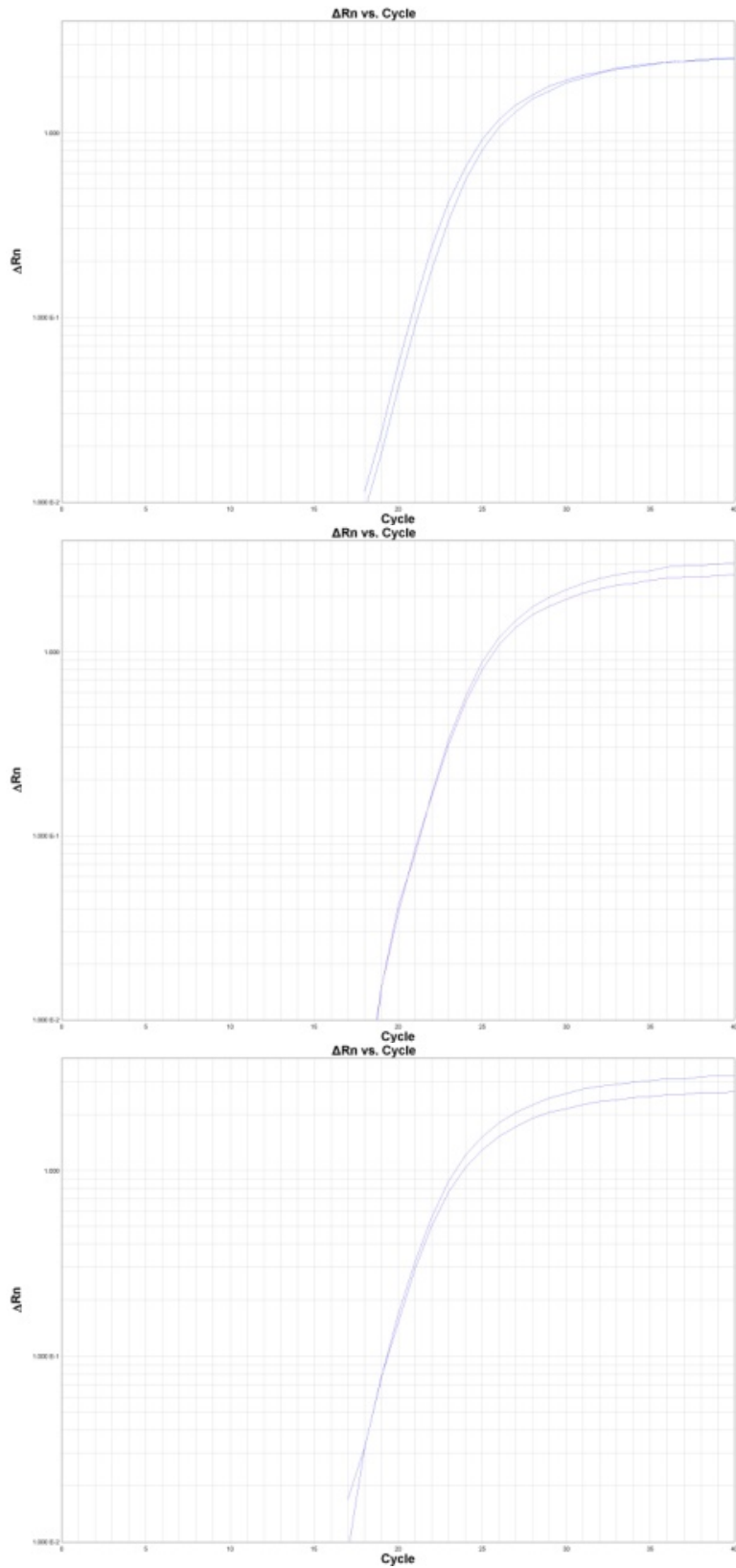


Figure D.2: PCR amplification curves for sample B (top), K (middle), and L (bottom).

The RQ min and RQ max columns show the top and bottom values of the expected error bars for each sample. Note that the error bars for the 10ng sample range from 0 to ~270 billion times amplification. These results were excluded from the remainder of the experiment. The 100 ng concentration P and Q samples of trial number 2 were also excluded for similar reasons. This is not totally unexpected. Since the ideal concentrations of cDNA for running PCR were unknown, multiple concentrations were tested.

Also, note that the NTC row of Table X contains no data. This is expected, since that sample was used purely as a control, with no cDNA placed in the well. If that row had data, it would signal a flaw in the experimental setup.

Finally, examine the 100 ng B, K, and L rows of Table D.3, which are highlighted in blue. The Ct value is the number of times the material was doubled before it reached a threshold value. Therefore each increase in Ct represents a doubling. The delta delta Ct value represents the difference in cycles to get to the threshold when normalized to the GAPDH control and the 100ng K MYCN sample. The RQ value is $2^{(\text{delta delta Ct})}$ and it represents how much more MYCN cDNA was in samples B and L. RQ min and RQ max represent the error bars for the RQ calculation. Figure D.3 graphically depicts the RQ values.

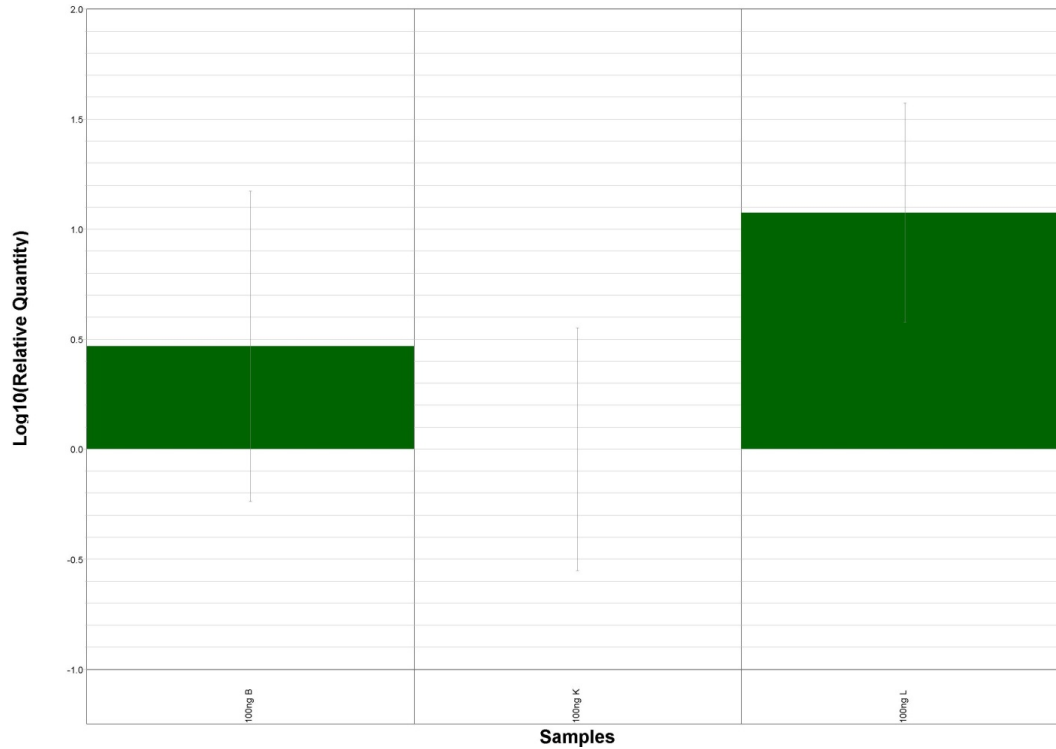


Figure D.3: Relative quantitative PCR results with sample K as the control

As shown, sample L, which was treated with tetracycline has 11.9 times more MYCN cDNA than the control sample K counterpart. This is a significant change because the error bars do not overlap. Sample B had approximately 2.9 times more MYCN cDNA than sample K; however, this difference was not significant, as exhibited by the overlapping error bars. These results suggest that treatment by tetracycline did increase the level of MYCN cDNA within the experimental cells.

APPENDIX E MARKET ANALYSIS FOR RAMAN BIOPSY TOOL

U.S. Cancer Incidence

It was estimated that there would be 1,399,790 new cases of cancer diagnosed in 2006 in the United States, including the following high-incidence cancers ("Cancer Facts & Figures 2006," 2006):

- Prostate Cancer (234,460)
- Breast Cancer (214,640)
- Lung Cancer (174,470)
- Colon Cancer (106,680)
- Melanoma (62,190)
- Bladder Cancer (61,420)

These numbers exclude new cases of basal and squamous cell carcinomas, as well as in situ carcinomas. Within Michigan, it was predicted there would be 48,250 new cancer cases diagnosed in 2006. As the average age of the American population continues to rise, it is expected that cancer incidence will rise accordingly. The incidence of invasive cancer developing at any site between birth and 39 years of age is 1 in 70 for men and 1 in 50 for women. By age 69, the odds of developing cancer increase to 1 in 6 for men and 1 in 9 for women ("Cancer Facts & Figures 2006," 2006).

Market Plan: Surgical Instrument

Preliminary data suggests a surgical spectrometer could be priced as low as \$10,000; however, the market may support a price much higher than this if the device is truly useful to the surgical user. For example, the newest daVinci robot sells for approximately \$1.5 million.

We propose selling our equipment for a fixed price, and then charging a per-use diagnostic fee for each biopsy performed. Initially, we will focus on the three highest-

incidence cancers in the United States (prostate, breast, and colon cancer), which account for over one third of total U.S. cancer cases annually, as shown in Table E.1. Lung cancer was excluded from preliminary marketing because it may require slightly different instrumentation (i.e. Raman measurement through and endoscope instead of through a probe).

	Annual US incidence	Annual MI incidence
Prostate Cancer	234,460	7,370
Breast Cancer	214,640	7,070
Colon Cancer	106,680	4,930*
TOTAL	555,780	19,370

*includes colon and rectal cancer

Table E.1: Annual incidence of the most common types of cancer

In the first year, we expect to sell 5 units to our collaborating hospitals. One hospital, Karmanos Cancer Institute sees 6,000 new patients per year. We assume that each of the other hospitals will see approximately the same amount of patients annually. Since prostate, breast, and colon cancer make up approximately 1/3 of cancer cases, we can assume approximately one third of cancer patients at each hospital will be seen with these conditions. Of the 2,000 patients per hospital, we will assume that one third undergo surgery using our diagnostic Raman probe for margin mapping. This allows for some patients who do not receive surgery, and it also accounts for surgical time of the instrument. With (52 weeks * 4 working days) 208 working days annually for elective surgeries, 667 cases per hospital equates to approximately three uses per day. This is in agreement with the average scheduling time necessary for a tumor resection surgery. 6000 cases * (1/3 of cases are prostate/breast/colon) * (1/3 of those cases) * 5 hospitals = 3,333 uses (See Table E.2)

Item	Cost	Number	Revenue
Laboratory systems	\$10,000	5	\$50,000
General biopsy diagnosis	\$10	3335	\$33,350
Total			\$83,350

Table E.2: Projected Year 1 revenue

Since no technology currently exists like this product, it is impossible to predict the product life cycle, or how quickly other users will adopt our technology. The following model is based on our best guess.

Following the first year, we expect our collaborating hospitals to adopt more systems in order to fully address their case load. We expect both surgeon and patient word of mouth in addition to our marketing to increase interest among outside institutions. In 2005, there were 4,936 community hospitals, including 2,927 urban hospitals and 2,009 rural hospitals (Association, B. C. a. B. S., 2008), however, we expect that the early adopters of the Raman probe technology will be the same users who are early adopters of similar high tech devices, such as the daVinci robot. Of the daVinci systems, 358 systems are placed in 290 Tier 1 hospitals (>325 beds), and 64 are located in Tier 2 hospitals (200-325 beds) ("U.S. Image Guided and Robot Assisted Surgery Markets N14C-54," 2008). Sixty one hospitals have two or more daVinci systems.

In year two, we predict that two thirds of the sixty one hospitals using multiple daVinci systems would be early adopters of our technology. We also predict that four of our original collaborating hospitals will invest in a second device, in order to increase the case load of Raman-diagnosed tumor resection surgeries. We predict that each

device will be used in approximately 667 cases annually, or about 3 cases per working day.

In year three, we predict selling 50 units, and we predict selling 75 units annually in years four and 5. By year 5, we expect to be involved in approximately 166,000 cases of breast, colon, and prostate cancer annually (Table E.3), or about 30% of cases. This still allows room for future growth. Expansion into other types of cancer or diagnosis of other diseases allows for further growth.

	Year 1	Year 2	Year 3	Year 4	Year 5
Units Sold	5	45	50	75	75
Total Units in the Market	5	50	100	175	250
Procedures Performed 667 cases / unit / year	3,335	33,350	66,700	116,725	166,750
Unit Revenue	\$50,000	\$440,000	\$500,000	\$750,000	\$750,000
Diagnostic Revenue	\$33,350	\$333,500	\$667,000	\$1,167,250	\$1,667,500
Total Annual Revenue	\$83,350	\$773,500	\$1,167,000	\$1,917,250	\$2,417,500
Cumulative Revenue	\$83,350	\$856,850	\$2,023,850	\$3,941,100	\$6,358,600

Table E.3: Predicted five year revenue of surgical instrument

9.6.1 *Surgical Biopsies*

Non-cancer diagnosis must also be included in market analysis. While most breast biopsies are performed through a needle, sometimes an open surgery is required to access the tissue in question. 1.6 million breast biopsies are performed annually in the U.S. Of those, approximately 5% (80,000) require an open biopsy (Shockney, L., 2009).

We do not anticipate selling any new devices for this market. Current customers would use their existing surgical systems to perform surgical biopsies. One local collaborator, Henry Ford Hospital, performs 48,000 breast procedures annually ("Breast

Cancer," 2010). Assuming each of our collaborators performs approximately the same amount of procedures, and 3% of those are surgical biopsies, we predict (48,000 procedures * 5 systems * .03 of cases) 7,200 biopsies performed in year one at \$10 diagnostic fee per case, for an additional revenue of **\$120,000** in breast biopsy cases alone. As long as a breast biopsy database exists, there would be minimal overhead cost in this market, as users would be paying for database lookup only.

9.6.2 Laboratory-Based In-Vitro Diagnostics

The global in-vitro market is expected to grow to \$8 billion annually in 2012, with 11% annual growth ("Global cancer diagnostics market to reach \$8B by 2012 ", 2008). The market increase is partially due to increased emphasis on cancer screening and early detection, as well as improved treatment methodologies, allowing cancer to be treated more like a chronic disease.

Design of a laboratory-use Raman spectrometer is actually much simpler than design of a handheld surgical system. Theoretically, the current probe design could be adapted for laboratory use, and sold at the same price of \$10,000. We would sell per-use diagnostic software, with a detailed diagnosis including tumor aggressiveness (etc) for an additional \$10.

If only breast biopsy samples are included in the analysis, there are 1.6 million annual cases. Assuming only growth with known collaborators in the first year (DMC/Karmanos, Henry Ford, U of M, U of Chicago, etc) in the first year, we can expect to sell 5 systems in year one, with growth growing exponentially after that. One local collaborator, Henry Ford Hospital, performs 48,000 breast procedures annually ("Breast Cancer," 2010). Assuming each of our collaborators performs approximately the same

amount of procedures, and assuming 10% of biopsy samples are tested with Raman spectroscopy, this equates to $(48,000 \cdot 10 \cdot 5) = 24,000$ biopsies in year one. We assume that 30% (7200) of those samples would be positive for breast cancer and would require in depth Raman diagnosis. The total revenue, then, in the first year would be

Item	Cost	Number	Revenue
Laboratory systems	\$10,000	5	\$50,000
General biopsy diagnosis	\$10	24,000	\$240,000
In-depth Raman Diagnosis	\$10	7,200	\$72,000
Total			\$362,000

Table E.4: Potential first-year revenue from pathology laboratory-based systems for breast cancer

This model poses minimal overhead costs. Development of laboratory systems should be simpler and quicker than development of portable systems. Conversely, a portable surgical system could be sold with a stationary mounting system and used as-is. The only other cost involved would be development and maintenance of diagnostic database systems. Furthermore, this laboratory system could easily be expanded to other types of cancer simply through sample testing and database development.

This model assumes about 4,800 biopsies per year per institution, which may be a slight over-estimation for what a normal hospital would see. Assuming (50 weeks * 5 working days) 250 working days per year for biopsies (overnight hospitalization is not normally required, so procedures are more commonly performed on Fridays), this equates to 19 biopsies per day.

Our 5 year model will assume a more reasonable 5 biopsies per day per institution, or 1,250 cases annually per institution. Since the biopsy market is actually

larger than the tumor resection market, we can estimate that the same number of units or more will be adopted for lab use as for surgical use.

	Year 1	Year 2	Year 3	Year 4	Year 5
Units Sold	5	45	50	75	75
Total Units in the Market	5	50	100	175	250
Procedures Performed 1250 cases / unit / year	6,250	62,500	125,000	218,750	312,500
Unit Revenue	\$50,000	\$440,000	\$500,000	\$750,000	\$750,000
Diagnostic Revenue	\$62,500	\$625,000	\$1,250,000	\$2,187,500	\$3,125,000
Total Annual Revenue	\$112,500	\$1,065,000	\$1,750,000	\$2,937,500	\$3,875,000
Cumulative Revenue	\$112,500	\$1,177,500	\$2,927,500	\$5,865,000	\$9,740,000
Annual Surgical Revenue*	\$83,350	\$773,500	\$1,167,000	\$1,917,250	\$2,417,500
Cumulative Surgical Revenue*	\$83,350	\$856,850	\$2,023,850	\$3,941,100	\$6,358,600
Total Annual Revenue	\$195,850	\$1,838,500	\$2,917,000	\$4,854,750	\$6,292,500
Total Cumulative Revenue	\$195,850	\$2,034,350	\$4,951,350	\$9,806,100	\$16,098,600

* Taken from Table E.3

Table E.5: Five-year revenues for laboratory-based diagnostics and surgical diagnostics

REFERENCES

- Althea Technologies Announces the Development of a Diagnostic Capable of Differentiating Multiple Forms of Childhood Cancer. 2007. Genetic Engineering & Biotechnology News, pp. Press Release.
- Association, A. M., About CPT®. Chicago, IL.
- Association, A. M., Applying for CPT® Codes. Chicago, IL.
- Association, A. M., CPT® Process - How a Code Becomes a Code. Chicago, IL.
- Association, B. C. a. B. S., 2008. Medical Cost Reference Guide. BlueCross BlueShield Association, Chicago, IL, pp.
- Baron, U., Freundlieb, S., et al., 1995. Co-regulation of two gene activities by tetracycline via a bidirectional promoter. Nucl. Acids Res. 23(17), 3605-3606.
- Breast Cancer. 2010. Henry Ford Health System.
- Brodeur, G., Pritchard, J., et al., 1993. Revisions of the international criteria for neuroblastoma diagnosis, staging, and response to treatment. J Clin Oncol 11(8), 1466-1477.
- Brodeur, G., Seeger, R., et al., 1988. International criteria for diagnosis, staging, and response to treatment in patients with neuroblastoma. J Clin Oncol 6(12), 1874-1881.
- Brown, K. L., Palyvoda, O. Y., et al., Raman spectroscopic differentiation of activated versus non-activated T lymphocytes: An in vitro study of an acute allograft rejection model. Journal of Immunological Methods In Press, Corrected Proof.
- Brown, K. L., Palyvoda, O. Y., et al., 2009a. Differentiation of alloreactive versus CD3/CD28 stimulated T-lymphocytes using Raman spectroscopy: A greater

specificity for noninvasive acute renal allograft rejection detection. *Cytometry Part A* 75A(11), 917-923.

Brown, K. L., Palyvoda, O. Y., et al., 2009b. Raman spectroscopic differentiation of activated versus non-activated T lymphocytes: An in vitro study of an acute allograft rejection model. *Journal of Immunological Methods* 340(1), 48-54.

Can Neuroblastoma be Found Early? , 2009. Cancer Reference Information, American Cancer Society.

Cancer Facts & Figures 2006. 2006. American Cancer Society, American Cancer Society, Atlanta, pp. 1-56.

Cao, A., Pandya, A. K., et al., 2007. A robust method for automated background subtraction of tissue fluorescence. *Journal of Raman Spectroscopy* 38(9), 1199-1205.

Caspers, P. J., Lucassen, G. W., et al., 2003. Combined In Vivo Confocal Raman Spectroscopy and Confocal Microscopy of Human Skin. *Biophysical Journal* 85(1), 572-580.

Chan, J. W., Taylor, D. S., et al., 2008. Nondestructive Identification of Individual Leukemia Cells by Laser Trapping Raman Spectroscopy. *Anal. Chem* 80(6), 2180-2187.

Chan, J. W., Taylor, D. S., et al., 2006. Micro-Raman Spectroscopy Detects Individual Neoplastic and Normal Hematopoietic Cells. *Biophysical Journal* 90(2), 648-656.

Chen, Q.-R., Vansant, G., et al., 2007. Diagnosis of the Small Round Blue Cell Tumors Using Multiplex Polymerase Chain Reaction. *J Mol Diagn* 9(1), 80-88.

Childhood Cancer Panel. 2008. Althea Dx.

- Chowdary, M. V., Kumar, K. K., et al., 2007. Discrimination of normal and malignant mucosal tissues of the colon by Raman spectroscopy. *Photomed Laser Surg* 25(4), 269-274.
- Clare, S. E., Neubauer, H., et al., 2006. Raman spectroscopy to distinguish progression stages in breast cancer. *J Clin Oncol (Meeting Abstracts)* 24(18_suppl), 10619-.
- Cohn, S. L., Pearson, A. D. J., et al., 2009. The International Neuroblastoma Risk Group (INRG) Classification System: An INRG Task Force Report. *J Clin Oncol* 27(2), 289-297.
- Colthup, N. B., Daly, L. H., et al., 1990. *Introduction to Infrared and Raman Spectroscopy*. Academic Press, A Division of Harcourt Brace & Company, San Diego, CA, pp. 1-73.
- Cotran, R. S., Kumar, V., et al. (eds.): 1994, *Robbins Pathologic Basis of Disease*, W.B. Saunders Company, Philadelphia, 1994.
- Crow, P., Barrass, B., et al., 2005a. The Use of Raman Spectroscopy to Differentiate Between Different Prostatic Adenocarcinoma Cell Lines. *Br J Cancer* 92(12), 69-82.
- Crow, P., Molckovsky, A., et al., 2005b. Assessment of fiberoptic near-infrared raman spectroscopy for diagnosis of bladder and prostate cancer. *Urology* 65(6), 1126-1130.
- Crow, P., Stone, N., et al., 2003a. The use of Raman spectroscopy to identify and grade prostatic adenocarcinoma in vitro. *British Journal of Cancer* 89, 106-108.
- Crow, P., Stone, N., et al., 2003b. The use of Raman spectroscopy to identify and grade prostatic adenocarcinoma in vitro. *Br J Cancer* 89(1), 106-108.

- Crow, P., Uff, J., et al., 2004. The use of Raman spectroscopy to identify and characterize transitional cell carcinoma in vitro. *BJU Int* 93(9), 1232-1236.
- Dai, H., 2005. Statistical Analysis of Raman Spectral Data For Cancer Detection. Department of Physics and Astronomy, Wayne State University, Detroit, pp. 67.
- de Paula, A., Sathaiah, S., 2005. Raman spectroscopy for diagnosis of atherosclerosis: a rapid analysis using neural networks. *Med Eng Phys* 27(3), 237-244.
- Do We Know What Causes Neuroblastoma? , 2009. Cancer Reference Information, American Cancer Society.
- Draux, F., Jeannesson, P., et al., 2008. Probing single live lung cancer cells using micro-raman spectroscopy. *AACR Meeting Abstracts 2008(1_Annual_Meeting)*, 5135-.
- Edsall, J. T., 1936. Raman Spectra of Amino Acids and Related Compounds I. The Ionization of the Carboxyl Group. *The Journal of Chemical Physics* 4(1), 1-8.
- Eilers, M., Eisenman, R. N., 2008. Myc's broad reach. *Genes & Development* 22(20), 2755-2766.
- Fendel, S., Schrader, B., 1998. Investigation of skin and skin lesions by NIR-FT-Raman spectroscopy. *Fresenius' Journal of Analytical Chemistry* 360(5), 609-613.
- Finegold, M. J., Triche, T. J., et al., 1983. Neuroblastoma and the differential diagnosis of small-, round-, blue-cell tumors. *Human Pathology* 14(7), 569-595.
- Frank, C. J., 1994. Applications of near-infrared raman spectroscopy to the study of human tissue specimens (breast cancer). pp. 187 pp.

- Frausto-Reyes, C., Medina-Gutierrez, C., et al., 2005. Qualitative study of ethanol content in tequilas by Raman spectroscopy and principal component analysis. *Spectrochim Acta A Mol Biomol Spectrosc* 61(11-12), 2657-2662.
- Geladi, P., Kowalski, B. R., 1986. Partial Least Square Regression: a tutorial. *Anal. Chem. Acta* 185, 1-7.
- Global cancer diagnostics market to reach \$8B by 2012 2008. HealthImaging.com.
- Gniadecka, M., Philipsen Peter, A., et al., 2004. Melanoma diagnosis by Raman spectroscopy and neural networks: structure alterations in proteins and lipids in intact cancer tissue. *Journal of investigative dermatology* 122(2), 443-449.
- Gniadecka, M., Wulf, H. C., et al., 1997. Distinctive molecular abnormalities in benign and malignant skin lesions: studies by Raman spectroscopy. *Photochem Photobiol* 66(4), 418-423.
- Gossen, M., Bujard, H., 1992. Tight control of gene expression in mammalian cells by tetracycline-responsive promoters. *Proceedings of the National Academy of Sciences of the United States of America* 89(12), 5547-5551.
- Gossen, M., Freundlieb, S., et al., 1995. Transcriptional activation by tetracyclines in mammalian cells. *Science* 268(5218), 1766-1769.
- Gregorio, A., Corrias, M. V., et al., 2008. Small round blue cell tumours: diagnostic and prognostic usefulness of the expression of B7-H3 surface molecule. *Histopathology* 53(1), 73-80.
- Gremlich, H.-U., Yan, B., 2001. *Infrared and raman spectroscopy of biological materials*. Marcel Dekker, New York, NY, pp. 581.

- Guicheteau, J., Argue, L., et al., 2008. Bacillus spore classification via surface-enhanced Raman spectroscopy and principal component analysis. *Appl Spectrosc* 62(3), 267-272.
- Haka, A. S., Shafer-Peltier, K. E., et al., 2002. Identifying Microcalcifications in Benign and Malignant Breast Lesions by Probing Differences in their Chemical Composition using Raman Spectroscopy. *Cancer Research* 62, 5375-5380.
- Haka, A. S., Shafer-Peltier, K. E., et al., 2005. Diagnosing breast cancer by using Raman spectroscopy. *Proceedings of the National Academy of Sciences of the United States of America* 102(35), 12371-12376.
- Haka AS, V., Gardecki, Nazemi, Lyons, Hicks, Fitzmaurice, Dasari, Crowe, Feld, 2006. In vivo Margin Assessment during Partial Mastectomy Breast Surgery Using Raman Spectroscopy. *Cancer Research* 66(6), 3317-3322.
- Haka, A. S., Volynskaya, Z., et al., 2006a. In vivo Margin Assessment during Partial Mastectomy Breast Surgery Using Raman Spectroscopy. *Cancer Research* 66(6), 3317-3322.
- Haka, A. S., Volynskaya, Z., et al., 2006b. In vivo Margin Assessment during Partial Mastectomy Breast Surgery Using Raman Spectroscopy. *Cancer Res* 66(6), 3317-3322.
- Haka, S.-P., Fitzmaurice, Crowe, Dasari, Feld, 2005. Diagnosing breast cancer by using Raman spectroscopy. *Proc Natl Acad Sci USA* 102(35), 12371-12376.
- Harvey, T. J., Faria, E. C., et al., 2008. Spectral discrimination of live prostate and bladder cancer cell lines using Raman optical tweezers. *Journal of Biomedical Optics* 13(6), 064004-064012.

- Hata, T. R., Scholz, T. A., et al., 2000. Non-invasive raman spectroscopic detection of carotenoids in human skin. *J Invest Dermatol* 115(3), 441-448.
- Hawi, S., Campbell, W., et al., 1996. Characterization of normal and malignant human hepatocytes by Raman microspectroscopy. *Cancer Lett* 110(1-2), 35-40.
- Hellerer, T., AxÃng, C., et al., 2007. Monitoring of lipid storage in *Caenorhabditis elegans* using coherent anti-Stokes Raman scattering (CARS) microscopy. *Proceedings of the National Academy of Sciences* 104(37), 14658-14663.
- Houssami, N., Irwig, L., et al., 2003. Sydney Breast Imaging Accuracy Study: Comparative sensitivity and specificity of mammography and sonography in young women with symptoms. *AJR Am J Roentgenol* 180(4), 935 - 940.
- How is Neuroblastoma Staged? , 2009. Cancer Reference Information, American Cancer Society.
- Howman-Giles, R., Shaw, P. J., et al., 2007. Neuroblastoma and Other Neuroendocrine Tumors. *Seminars in Nuclear Medicine* 37(4), 286-302.
- Huang, Y., Karashima, T., et al., 2005. Molecular-level investigation of the structure, transformation, and bioactivity of single living fission yeast cells by time- and space-resolved Raman spectroscopy. *Biochemistry* 44(30), 10009-10019.
- Huang, Z., McWilliams, A., et al., 2003a. Effect of formalin fixation on the near-infrared Raman spectroscopy of normal and cancerous human bronchial tissues. *INTERNATIONAL JOURNAL OF ONCOLOGY* 23, 649-655.
- Huang, Z., McWilliams, A., et al., 2003b. Near-infrared Raman spectroscopy for optical diagnosis of lung cancer. *Int J Cancer* 107(6), 1047-1052.

- Jarvis, R., Goodacre, R., 2004. Discrimination of bacteria using surface-enhanced Raman spectroscopy. *Analytical Chemistry* 76(1), 40-47.
- Jemal, A., Siegel, R., et al., 2008. Cancer Statistics, 2008. *CA Cancer J Clin* 58(2), 71-96.
- Jess, P., Mazilu, M., et al., 2009. Optical detection and grading of lung neoplasia by Raman microspectroscopy. *Int J Cancer* 124(2), 376-380.
- Jessen, K. R., Mirsky, R., 2005. The origin and development of glial cells in peripheral nerves. *Nat Rev Neurosci* 6(9), 671-682.
- Johansson, C. K., Christensen, D. H., et al., 1999. Near-infrared Fourier transform Raman spectral studies of human skin. *Dansk Kemi* 80(8), 12-13.
- Jolliffe, I. T., 1986. *Principle Component Analysis*
- Kaminaka, S., Yamazaki, H., et al., 2001. Near-infrared Raman spectroscopy of human lung tissues: possibility of molecular-level cancer diagnosis. *Journal of Raman Spectroscopy* 32(2), 139-141.
- Kast, R., Rabah, R., et al., Accepted for June 2010. Differentiation of Small Round Blue Cell Tumors Using Raman Spectroscopy. *Journal of Pediatric Surgery*.
- Kast, R. E., Serhatkulu, G. K., et al., 2008. Raman spectroscopy can differentiate malignant tumors from normal breast tissue and detect early neoplastic changes in a mouse model. *Biopolymers* 89(3), 235-241.
- Kawabata, T., Mizuno, T., et al., 2008. Optical diagnosis of gastric cancer using near-infrared multichannel Raman spectroscopy with a 1064-nm excitation wavelength. *J Gastroenterol* 43(4), 283-290.

- Kendall, C., Stone, N., et al., 2003. Raman spectroscopy, a potential tool for the objective identification and classification of neoplasia in Barrett's oesophagus. *J Pathol* 200(5), 602-609.
- Khan, J., Wei, J., et al., 2001. Development of a molecular taxonomy of small blue round-cell tumors using cDNA microarrays. *Nat Genet*.
- Klecka, W. R., 1980. *Discriminant Analysis*. Sage Publications, Inc., Newbury Park, CA, pp.
- Koljenovic, S., Choo-Smith, L., et al., 2002. Discriminating vital tumor from necrotic tissue in human glioblastoma tissue samples by Raman spectroscopy. *Lab Invest* 82(10), 1265-1277.
- Krafft, C., Miljanic, S., et al., 2003. Near-infrared Raman spectroscopy to study the composition of human brain tissue and tumors. *Proceedings of SPIE-The International Society for Optical Engineering 5141(Diagnostic Optical Spectroscopy in Biomedicine II)*, 230-236.
- Krafft, C., Steiner, G., et al., 2009. Disease recognition by infrared and Raman spectroscopy. *J Biophotonics* 2(1-2), 13-28.
- Li, X., Lin, J., et al., 2004. Spectral analysis for diagnosis of esophagus dysplasia using fluorescence Raman spectroscopy. *Conf Proc IEEE Eng Med Biol Soc* 1, 141-144.
- Lieber, C., Kabeer, M., Characterization of pediatric Wilms' tumor using Raman and fluorescence spectroscopies. *J Pediatr Surg* 45(3), 549-554.
- Lutz, W., Stohr, M., et al., 1996. Conditional expression of N-myc in human neuroblastoma cells increases expression of alpha-prothymosin and ornithine

- decarboxylase and accelerates progression into S-phase early after mitogenic stimulation of quiescent cells. *Oncogene* 13(4), 803-812.
- Mahadevan-Jansen, A., Follen Mitchell, M., et al., 1998a. Near-infrared Raman spectroscopy for in vitro detection of cervical precancers. *Photochem Photobiol* 68(1), 123-132.
- Mahadevan-Jansen, A., Mitchell, M. F., et al., 1998b. Development of a fiber optic probe to measure NIR Raman spectra of cervical tissue in vivo. *Photochem Photobiol* 68(3), 427-431.
- Malini, R., Venkatakrishna, K., et al., 2006. Discrimination of Normal, Inflammatory, Premalignant, and Malignant Oral Tissue: A Raman Spectroscopy Study. *Biopolymers* 81, 179-193.
- Mandel, J. S., Bond, J. H., et al., 1993. Reducing Mortality from Colorectal Cancer by Screening for Fecal Occult Blood. *N Engl J Med* 328(19), 1365-1371.
- Mannie, M. D., McConnell, T. J., et al., 2005. Activation-dependent phases of T cells distinguished by use of optical tweezers and near infrared Raman spectroscopy. *Journal of Immunological Methods* 297(1-2), 53-60.
- Manoharan, R., Shafer, K., et al., 1998. Raman spectroscopy and fluorescence photon migration for breast cancer diagnosis and imaging. *Photochem Photobiol* 67(1), 15-22.
- Mariani, M. M., Lampen, P., et al., 2009. Impact of fixation on in vitro cell culture lines monitored with Raman spectroscopy. *The Analyst* 134(6), 1154-1161.
- Maris, J. M., Matthay, K. K., 1999. Molecular Biology of Neuroblastoma. *J Clin Oncol* 17(7), 2264-.

- Matthaus, C., Chernenko, T., et al., 2007. Label-Free Detection of Mitochondrial Distribution in Cells by Nonresonant Raman Microspectroscopy. *Biophysical Journal* 93(2), 668-673.
- Meltzer, P. S., 2007. Is Ewing's Sarcoma a Stem Cell Tumor? *Cell Stem Cell* 1(1), 13-15.
- Motz, J. T., Gandhi, S. J., et al., 2005. Real-time Raman system for in vivo disease diagnosis. *J Biomed Opt* 10(3), 031113.
- Motz, J. T., Hunter, M., et al., 2004. Optical fiber probe for biomedical Raman spectroscopy. *Appl Opt* 43(3), 542-554.
- Mourant, J., Gibson, R., et al., 2003. Methods for measuring the infrared spectra of biological cells. *Phys Med Biol* 48(2), 243-257.
- Nakama, H., Kamijo, N., et al., 1997. Clinical diagnostic accuracy of faecal occult blood test for anal diseases. *Int J Qual Health Care* 9(2), 139 - 141.
- Nanda, K., McCrory, D., et al., 2000. Accuracy of the Papanicolaou test in screening for and follow-up of cervical cytologic abnormalities: a systematic review. *Ann Intern Med* 132(10), 810 - 819.
- NanoDrop Technical Support Bulletin T009. 2007. NanoDrop Technologies.
- Nijssen, A., Maquelin, K., et al., 2007. Discriminating basal cell carcinoma from perilesional skin using high wave-number Raman spectroscopy. *Journal of Biomedical Optics* 12(3), 034004.
- Notingher, I., Verrier, S., et al., 2002. In situ characterisation of living cells by Raman spectroscopy. *Spectroscopy* 16(2), 43-51.

- Olsen, O., Gøtzsche, P. C., 2001. Cochrane review on screening for breast cancer with mammography. *The Lancet* 358(9290), 1340-1342.
- Orkin, S. H., Fisher, D. E., et al., 2009. *Oncology of Infancy and Childhood*. Saunders, Maryland Heights, MO, pp.
- Pandya, A., Serhatkulu, G., et al., 2008. Evaluation of Pancreatic Cancer with Raman spectroscopy in a Mouse Model. *Pancreas* 36(2), e1-e8.
- Pandya, A. K., Serhatkulu, G. K., et al., 2008. Evaluation of Pancreatic Cancer With Raman Spectroscopy in a Mouse Model. *Pancreas* 36(2), e1-e8
- Rabah, R., Weber, R., et al., 2008. Diagnosis of neuroblastoma and ganglioneuroma using Raman spectroscopy. *Journal of Pediatric Surgery* 43(1), 171-176.
- Redd, D. C. B., Feng, Z. C., et al., 1993. Raman spectroscopic characterization of human breast tissues: implications for breast cancer diagnosis. *Applied Spectroscopy* 47(6), 787-791.
- Reisner, L. A., King, B. W., et al., 2007. A prototype biosensor-integrated image-guided surgery system. *The International Journal of Medical Robotics and Computer Assisted Surgery* 3(1), 82-88.
- Robichaux-Viehoever, A., Kanter, E., et al., 2007. Characterization of Raman spectra measured in vivo for the detection of cervical dysplasia. *Appl Spectrosc* 61(9), 986-993.
- Sato-Berru, R., Mejia-Uriarte, E., et al., 2007. Application of principal component analysis and Raman spectroscopy in the analysis of polycrystalline BaTiO₃ at high pressure. *Spectrochim Acta A Mol Biomol Spectrosc* 66(3), 557-560.

- Sawada, T., Matsumura, T., et al., 1991. Long-term effects of mass screening for neuroblastoma in infancy. *Am J Pediatr Hematol Oncol* 13(1), 3-7.
- Schäfer, A. T., Kaufmann, J. D., 1999. What happens in freezing bodies?: Experimental study of histological tissue change caused by freezing injuries. *Forensic Science International* 102(2-3), 149-158.
- Schulz, H., Baranska, M., et al., 2005. Potential of NIR-FT-Raman spectroscopy in natural carotenoid analysis. *Biopolymers* 77(4), 212-221.
- Schuster, K., Urlaub, E., et al., 2000. Single-cell analysis of bacteria by Raman microscopy: spectral information on the chemical composition of cells and on the heterogeneity in a culture. *J Microbiol Methods* 42(1), 29-38.
- Shetty, G., Kendall, C., et al., 2006a. Raman Spectroscopy: Elucidation of Biochemical Changes in Carcinogenesis of Oesophagus. *Br J Cancer* 94(10), 1460-1464.
- Shetty, G., Kendall, C., et al., 2006b. Raman spectroscopy: elucidation of biochemical changes in carcinogenesis of oesophagus. *Br J Cancer* 94(10), 1460-1464.
- Shim, M. G., Wilson, B. C., 1996. The Effects of ex vivo Handling Procedures on the Near-Infrared Raman Spectra of Normal Mammalian Tissues. *Photochemistry and Photobiology* 63(5), 662-671.
- Shim, M. G., Wilson, B. C., 1997. Development of an in vivo Raman spectroscopic system for diagnostic applications. *J. Raman Spectrosc* 28, 131-142.
- Shim, M. G., Wilson, B. C., et al., 1999. Study of Fiber-Optic Probes for In Vivo Medical Raman Spectroscopy. *Applied Spectroscopy* 53, 619-627.
- Shimada, H., Ambros, I., et al., 1999a. The International Neuroblastoma Pathology Classification (the Shimada system). *Cancer* 86(2), 364-372.

- Shimada, H., Ambros, I. M., et al., 1999b. Terminology and morphologic criteria of neuroblastic tumors. *Cancer* 86(2), 349-363.
- Shockney, L., 2009. Before You Get a Biopsy, Read This. Yahoo! Health.
- Short, K. W., Carpenter, S., et al., 2005. Raman Spectroscopy Detects Biochemical Changes Due to Proliferation in Mammalian Cell Cultures. *Biophysical Journal* 88(6), 4274-4288.
- Slack, A., Chen, Z., et al., 2005. The p53 regulatory gene MDM2 is a direct transcriptional target of MYCN in neuroblastoma. *Proceedings of the National Academy of Sciences of the United States of America* 102(3), 731-736.
- Smith, E., Dent, G., 2005. *Modern Raman Spectroscopy: A Practical Approach*. Wiley, West Sussex, England, pp. 1-222.
- Socrates, G., 2001. *Infrared and Raman Characteristic Group Frequencies*. John Wiley & Sons Ltd, West Sussex, England, pp. 1-347.
- Stevens, J. P., 2002. *Applied Multivariate Statistics for the Social Sciences*. Lawrence Erlbaum Associates, Publishers, Mahwah, NJ, pp.
- Stone, N., Kendall, C., et al., 2002. Near-infrared Raman spectroscopy for the classification of epithelial pre-cancers and cancers. *Journal of Raman Spectroscopy* 33(7), 564-573.
- Stone, N., Stavroulaki, P., et al., 2000. Raman spectroscopy for early detection of laryngeal malignancy: preliminary results. *Laryngoscope* 110(10 Pt 1), 1756-1763.
- Tabachnick, B. G., Fidell, L. S., 2007. *Using Multivariate Statistics*. Pearson, Boston, pp.

- Taleb, A., Diamond, J., et al., 2006. Raman microscopy for the chemometric analysis of tumor cells. *J Phys Chem B* 110(39), 19625-19631.
- Taylor, C., Patel, K., et al., 1993. Diagnosis of Ewing's sarcoma and peripheral neuroectodermal tumour based on the detection of t(11;22) using fluorescence in situ hybridisation. *British Journal of Cancer* 67(1), 128-133.
- Teixeira, C., Bitar, R., et al., 2009. Thyroid tissue analysis through Raman spectroscopy. *Analyst* 134(11), 2361-2370.
- Thakur, J. S., Dai, H., et al., 2007. Raman spectral signatures of mouse mammary tissue and associated lymph nodes: normal, tumor and mastitis. *Journal of Raman Spectroscopy* 38(2), 127-134.
- Thiele, C. J., 1998. Neuroblastoma. In Masters, J. (Ed.), *Human Cell Culture*. Klumwer Academic Publishers, Lacaster, UK, pp. 21-53.
- Thiele, C. J., Reynolds, C. P., et al., 1985. Decreased expression of N-myc precedes retinoic acid-induced morphological differentiation of human neuroblastoma. *Nature* 313(6001), 404-406.
- Treuner, J., Schilling, F. H., 1995. Neuroblastoma mass screening: The arguments for and against. *European Journal of Cancer* 31(4), 565-568.
- U.S. Image Guided and Robot Assisted Surgery Markets N14C-54. 2008. Frost & Sullivan.
- Utzinger, U., Heintzelman, D. L., et al., 2001. Near-infrared Raman spectroscopy for in vivo detection of cervical precancers. *Applied Spectroscopy* 55(8), 955-959.
- Utzinger, U., Richards-Kortum, R., 2003. Fiber optic probes for biomedical optical spectroscopy. *J Biomed Opt* 8(1), 121-147.

- van Noesel, M., Hahlen, K., et al., 1997. Neuroblastoma 4S: a heterogeneous disease with variable risk factors and treatment strategies. *Cancer* 80(5), 834-843.
- Verma, S. P., Schmidt-Ullrich, R., et al., 1977. Differences between the Structural Dynamics of Plasma Membranes of Normal Hamster Lymphocytes and Lymphoid Cells Neoplastically Transformed by Simian Virus 40 as Revealed by Laser Raman Spectroscopy. *Cancer Res* 37(10), 3490-3493.
- Verrier, S., Notingher, I., et al., 2004. In situ monitoring of cell death using Raman microspectroscopy. *Biopolymers* 74(1-2), 157-162.
- Vuguin, P. M., 2009. Pheochromocytoma. in Windle, M. L., Bergstrom, S. K., et al. (eds.), *emedicine from WebMD*.
- Weber, R. E., 2007. Comparison of discriminant function analysis and neural networks for tissue identification using Raman spectroscopy. Department of Physics and Astronomy, Wayne State University, Detroit, MI.
- What Are the Key Statistics About Neuroblastoma? , 2009. Cancer Reference Information, American Cancer Society.
- What are the Risk Factors for Neuroblastoma? , 2009. Cancer Reference Information, American Cancer Society.
- What is Neuroblastoma. 2009. Cancer Reference Information, American Cancer Society.
- Wills, H., Kast, R., et al., 2009a. Raman spectroscopy detects and distinguishes neuroblastoma and related tissues in fresh and (banked) frozen specimens. *Journal of Pediatric Surgery* 44(2), 386-391.

- Wills, H., Kast, R., et al., February 2008. Raman Spectroscopy Detects and Distinguishes Neuroblastoma and Related Tissues in Fresh and (Banked) Frozen Specimens. *Journal of Pediatric Surgery*.
- Wills, H., Kast, R., et al., (Submitted). Diagnosis of Wilms Tumor Using Raman Spectroscopy. *Journal of Pediatric Surgery*.
- Wills, H., Kast, R., et al., 2009b. Diagnosis of Wilms' tumor using near-infrared Raman spectroscopy. *Journal of Pediatric Surgery* 44(6), 1152-1158.
- Winawer, S. J., 2007. Colorectal cancer screening. *Best Practice & Research Clinical Gastroenterology* 21(6), 1031-1048.
- Wolthuis, R., van Aken, M., et al., 2001. Determination of water concentration in brain tissue by Raman spectroscopy. *Analytical Chemistry* 73(16), 3915-3920.
- Yazdi, Y., Ramanujam, N., et al., 1999. Resonance Raman Spectroscopy at 257nm Excitation of Normal and Malignant Cultured Breast and Cervical Cells. *Applied Spectroscopy* 53, 82-85.
- Ye, Z., Auner, G., 2003. Linear filtering and nonlinear fuzzy logic filtering for sample identification with Raman spectroscopy. *Systems, Man and Cybernetics*, 2003. IEEE International Conference on, pp. 4619-4624 vol.4615.
- Ye, Z., Auner, G., 2004a. Principal component analysis approach for biomedical sample identification. *Systems, Man and Cybernetics*, 2004 IEEE International Conference on, pp. 1348-1353 vol.1342.
- Ye, Z., Auner, G., 2004b. Raman spectrum baseline identification and its optimization using genetic algorithm. *Intelligent Control*, 2004. Proceedings of the 2004 IEEE International Symposium on, pp. 489-494.

Young Jr, J. L., Ries, L. G., et al., 1986. Cancer incidence, survival, and mortality for children younger than age 15 years. *Cancer* 58(S2), 598-602.

ABSTRACT**IDENTIFICATION OF NEUROBLASTOMA AND ITS PROGNOSTIC MARKERS
USING RAMAN SPECTROSCOPY**

by

RACHEL KAST**May 2010****Advisors:** Dr. Gregory Auner and Dr. Abhilash Pandya**Major:** Biomedical Engineering**Degree:** Doctor of Philosophy

Introduction: Neuroblastoma is the most common cancer of infancy. It is one of several peripheral nervous system tumors, including ganglioneuroma, peripheral nerve sheath tumor, and pheochromocytoma. It is commonly situated on the adrenal gland. It displays similar histology to other small round blue cell tumors, including non-Hodgkin lymphoma, rhabdomyosarcoma, and Ewing sarcoma. One method of judging neuroblastoma aggressiveness uses tumor histology factors, including mitosis-karyorrhexis index, Schwannian stromal development, degree of differentiation, and patient age. Tumor aggressiveness can also be judged based on the amplification of certain genes, including MYCN. Raman spectroscopy is a physics-based method which identifies the biochemical fingerprint of a sample. It has recently been applied to disease classification, specifically in adult cancers.

Methods: To identify neuroblastoma from adrenal gland, peripheral nervous system tumors, and small round blue cell tumors, and to identify tumor histology, fresh and frozen samples were collected from the operating room and tested with Raman spectroscopy. Tissues were assigned a 'gold standard' diagnosis by experienced

pediatric pathologists. Tumor histology was further evaluated with blinded tissues provided by the Children's Oncology Group. To test identification of gene amplification, the tet-on MYCN-3 cell line was cultured in the presence and absence of tetracycline to induce or repress MYCN gene expression. Cells were harvested and tested with Raman spectroscopy and polymerase chain reaction. All Raman spectra were preprocessed and classified with discriminant function analysis.

Results: Raman spectroscopy identified neuroblastoma from healthy adrenal gland, peripheral nervous system tumors, and small round blue cell tumors with 100% sensitivity and specificity. It identified favorable, unfavorable, and treated neuroblastoma with high accuracy. Neuroblastoma cells with and without MYCN amplification were identified with 100% sensitivity and specificity.

Conclusions: This is the first study applying Raman spectroscopy to identify pediatric tumors, and the first blinded Raman spectroscopy study performed in collaboration with the Children's Oncology Group, a national tumor bank. It provides the first in-depth examination of specific markers of aggressiveness, including tumor favorability and MYCN gene amplification. Raman spectroscopy has the potential to revolutionize the field of cancer diagnostics. It can provide a detailed, accurate diagnosis in minutes instead of days.

AUTOBIOGRAPHICAL STATEMENT

RACHEL KAST

Education

Wayne State University Detroit, MI	2010	Ph.D.	Biomedical Engineering
Wayne State University Detroit, MI	2007	M.S.	Physics
Kettering University Flint, MI	2005	B.S.	Applied Physics

Work Experience

Wayne State University

Smart Sensors and Integrated Microsystems

Graduate Research Assistant

June 2007 - present

Department of Physics

Graduate Teaching/Research Assistant

September 2005 - May 2007

Undergraduate Research Assistant

June 2005 - August 2005

Lear Corporation

Sound Quality Co-op

January 2004 – March 2005

Stephen Computer Services, Inc.

Software Quality Co-op

May 2001 – December 2003

Publications

- Leslie, D., Kast, R., et al., (in preparation). Identification of Pediatric Brain Neoplasms Using Raman Spectroscopy. *Cancer Research*.
- Kast, R., Rabah, R., et al., (Accepted for 2010). Differentiation of Small Round Blue Cell Tumors Using Raman Spectroscopy. *Journal of Pediatric Surgery*.
- Wills, H., Kast, R., et al., 2009. Diagnosis of Wilms' tumor using near-infrared Raman spectroscopy. *J Pediatr Surg* 44(6), 1152-1158; discussion 1158.
- Wills, H., Kast, R., et al., 2009. Raman spectroscopy detects and distinguishes neuroblastoma and related tissues in fresh and (banked) frozen specimens. *Journal of Pediatric Surgery* 44(2), 386-391.
- Kast, R. E., Serhatkulu, G. K., et al., 2008. Raman spectroscopy can differentiate malignant tumors from normal breast tissue and detect early neoplastic changes in a mouse model. *Biopolymers* 89(3), 235-241.
- Rabah, R., Weber, R., et al., 2007. Diagnosis of Neuroblastoma and Ganglioneuroma Using Raman Spectroscopy. *American Pediatric Surgical Association 38th Annual Meeting, Orlando, FL*.
- Pandya, A., Serhatkulu, G., et al., 2008. Evaluation of Pancreatic Cancer with Raman spectroscopy in a Mouse Model. *Pancreas* 36(2), e1-e8.
- Cao, A., Pandya, A. K., et al., 2007. A robust method for automated background subtraction of tissue fluorescence. *Journal of Raman Spectroscopy* 38(9), 1199-1205.
- Weber, R. E., 2007. Comparison of discriminant function analysis and neural networks for tissue identification using Raman spectroscopy. *Department of Physics and Astronomy, Wayne State University, Detroit, MI*.
- Weber, R. E., 2005. Automation of Sound Intensity Scanning Process. *Department of Physics, Kettering University, Flint, MI*.